

Rational Design of Mesoporous Adsorbents for the Removal of Organic Pollutants from Water

Doctoral Dissertation of:
Wannes Libbrecht

Promotors:
Prof. Pascal Van Der Voort
Prof. Jeriffa De Clercq
Prof. Joris W. Thybaut



Dissertation submitted in fulfillment of the requirements for the degree of
Doctor of Science: Chemistry

Department of Inorganic and Physical Chemistry
Faculty of Sciences
Ghent University
2016-2017

Contents

List of Figures	vi
List of Tables	xii
List of Abbreviations	xv
1 Introduction	1
1.1 Preface	1
1.2 Outline	3
1.3 Mesoporous carbons	4
1.3.1 Precursor types	5
1.3.2 Surfactant types	9
1.3.3 Precursor to surfactant ratios	15
1.3.4 Acid or base catalysts	17
1.3.5 Synthesis pathways	21
1.3.6 Carbonization temperature	22
1.3.7 Surface modification	23
1.4 Adsorption of organic pollutants	25
1.5 Conclusions	32
2 Characterization of Porous materials	35
2.1 Nitrogen sorption	35
2.2 Powder X-ray diffraction	40
2.3 Elemental analysis	40
2.4 DRIFTS	41
2.5 Raman spectroscopy	42
2.6 Thermogravimetric analysis	42
2.7 UV-Vis spectroscopy	42
2.8 LC-OCD	43
2.9 Zeta potential measurements	44
2.10 TEM and SEM	44
3 Optimization of Mesoporous Carbon Synthesis via Definitive Screening Design	47

3.1	Introduction	47
3.2	Experimental	49
3.2.1	Mesoporous carbon synthesis	49
3.2.2	DSD and data analysis	50
3.2.3	Characterization	50
3.2.4	Adsorption tests	51
3.3	Results and Discussion	51
3.4	Characterization of the mesoporous carbons	54
3.4.1	Definitive Screening Design Model evaluation	57
3.5	Optimization	63
3.6	Adsorption experiments	64
3.7	Conclusions	67
4	Tuning the Pore Geometry of Ordered Mesoporous Carbons for Enhanced Adsorption of Bisphenol-A	69
4.1	Introduction	69
4.2	Experimental Section	71
4.2.1	Synthesis of Ordered Mesoporous Carbons	71
4.2.2	Adsorption Tests	72
4.3	Results and Discussion	74
4.3.1	Characterization of the Adsorbents	74
4.3.2	Adsorption Isotherms	77
4.3.3	Adsorption Kinetics	78
4.4	Conclusions	82
5	Tunable Large Pore Mesoporous Carbons for the Enhanced Adsorption of Humic Acid	83
5.1	Introduction	83
5.2	Materials and methods	84
5.2.1	Adsorption Tests	85
5.3	Results and Discussion	87
5.3.1	Effect of p/s ratio on material characteristics	87
5.3.2	Effect of carbonization temperature on material characteristics	91
5.3.3	Humic acid adsorption	94
5.3.4	Adsorption kinetics of SMC-800-0.25 and AC	95
5.3.5	Adsorption isotherms of SMC-800-y and AC	96
5.3.6	Influence of the pH	98
5.3.7	Molecular weight distribution of HA	99
5.4	Conclusions	100
6	Porous Boron Nitride as New Adsorbent Material	103
6.1	Introduction	103
6.2	Experimental	105

6.2.1	Hard template porous BN synthesis	105
6.2.2	Template-free porous boron nitride synthesis	106
6.2.3	Characterization	106
6.2.4	Adsorption tests	107
6.3	Results and Discussion	108
6.3.1	Hard templated h-BN	108
6.3.2	Template-free h-BN	113
6.3.3	Adsorption experiments	120
6.3.4	BN stability	121
6.4	Conclusions	124
7	Conclusions	125
8	English and Dutch summary	129
8.1	English summary	129
8.1.1	Optimization of mesoporous carbon synthesis via DSD	130
8.1.2	Influence of pore geometry on the adsorption of bisphenol A	131
8.1.3	Tuning the pore size for enhanced adsorption of humic acid	132
8.1.4	Porous boron nitride as new adsorbent	133
8.1.5	Conclusions and outlook	135
8.2	Nederlandstalige samenvatting	136
8.2.1	Optimalisatie van de mesoporeuze koolstofsynthese	136
8.2.2	Invloed van de poriestructuur op de adsorptie van BPA	138
8.2.3	Afstemmen van de poriegrootte van mesoporeuze koolstoffen voor humuszuuradsorptie	140
8.2.4	Poreus boornitride als nieuw adsorbens	141
8.2.5	Conclusies en toekomstperspectieven	142
	Bibliography	145

List of Figures

1.1	Carbon precursors: phenol, resorcinol (benzene-1,3-diol) and phloroglucinol (benzene-1,3,5-triol).	5
1.2	Self-assembly of phloroglucinol with PEO segments via H-bonding for better ordering of the mesostructure [26].	6
1.3	Biosourced precursors: tannin, a main component of larch sawdust: hexahydroxydiphenic acid and an example of a possible lignin structure.	8
1.4	Different surfactant structures used for soft template mesoporous carbon synthesis.	13
1.5	Nitrogen sorption isotherms (A) and pore size distribution (B) of (a) C-FDU- 18-1, (b) C-FDU-18-2, and (c) C-FDU-18-3. The N ₂ sorption isotherms of (a) C-FDU-18-1 are offset vertically by -100 cm ³ /g [41].	14
1.6	Influence of surfactant type and p/s ratio on ordering of the mesoporous carbon [7].	16
1.7	Schematic representation of mesoporous polymer and carbon synthesis with different morphologies depending on the p/s ratio or type of surfactant used [7].	17
1.8	acid catalyzed reaction mechanism.	18
1.9	base catalyzed reaction mechanism.	19
1.10	Novolac structure (left) and resol structure (right) before curing into 3D interconnected polymer.	19
1.11	A possible mechanism of ultra-large pores creation in mesoporous carbons by varying acid concentration [46].	20
1.12	Effect of carbonization temperature on the pore size of FDU-16 (circles) and FDU-15 (triangles) (left) [7] and the PSD of mesoporous carbons synthesized with R/f/glutamic acid (right) [59].	22
1.13	TEM images (a-d) and HRTEM images (e, f) of mesoporous materials FDU-15 prepared by using F127 as a template via the EISA method after calcination at 350 °C (FDU-15-350; a, b) and at 1200 °C (FDU-15-1200; c-f) under an Ar atmosphere, viewed from the [110] (a, c, e) and [001] (b, d, f) directions [7].	24
1.14	pH-effect on functionalities of carbon adsorbents in aqueous solutions [87].	25

1.15	Properties of organic adsorbates with different MW and size or RH = hydrodynamic radius.	27
1.16	Adsorption kinetics of 10 mg of CMK-3 (■) and PAC (▲) in 100 mL of 25 mg/L BPA-solution [100].	28
2.1	Different types of N ₂ sorption isotherms identified by IUPAC [114].	36
2.2	Different hysteresis types identified by IUPAC [114].	37
2.3	Different stages of a nitrogen sorption isotherm of a soft templated mesoporous carbon.	39
2.4	Schematic representation of Bragg's law.	41
2.5	Schematic representation of LC-OCD setup [115].	43
2.6	TEM images of ordered mesoporous carbons viewed along the [110] (a, c and e) and [001] (b, d and f) directions [77].	46
3.1	Nitrogen sorption isotherms with precursor/surfactant ratio 0.5 (triangles) and 2.0 (circles).	52
3.2	Nitrogen sorption isotherms (left) with an increasing shift of 150 cm ³ STP/g for each isotherm and pore size distributions (right) with a shift of 0.1 cm ³ /g.nm for each curve of the 11 DSD materials.	55
3.3	XRD patterns of ordered 2D hexagonal mesoporous carbons (left) and less ordered carbons (right).	58
3.4	Predicted versus experimental microporous surface area (left) and microporous volume (right).	61
3.5	Predicted versus experimental mesoporous surface area (left) and mesoporous volume (right).	62
3.6	Predicted versus experimental carbon content.	62
3.7	Optimal values for the significant parameters influencing the mesoporous surface area, and the predicted value (red) together with the lower and upper limits (blue).	63
3.8	Nitrogen sorption isotherms and pore size distribution (inset) for the mesoporous carbon with optimized S _{meso}	64
3.9	Predicted versus experimental adsorption capacity with S _{meso} and wt% C as significant factors with DSD1, 8, 9 (left) following Equation 3.8 and without DSD1, 8, 9 (right) following Equation 3.9.	66
4.1	N ₂ sorption isotherms (left) and their corresponding pore size distributions obtained by density functional theory (DFT) method (right) of CMK-3 (■), AC (●) and SMC (▲).	75
4.2	Powder X-ray diffraction patterns of CMK-3 (a) and SMC (b).	75
4.3	Transmission electron microscope (TEM) images of CMK-3 (left) and SMC (right).	76

4.4	Adsorption isotherms of 10 mg of CMK-3 (■), AC (●) and SMC (▲) in 100 mL of BPA-solution, experimental data were fitted with the Langmuir and Freundlich model, the error bars represent the standard deviation of the triplicate measurements.	78
4.5	Adsorption kinetics of 100 mg of CMk-3 (■), AC (●) and SMC (▲) in 1 L of 60 mg/L BPA-solution, particle size is between 62 and 88 μm , the error bars represent the standard deviation of the triplicate measurements, the dashed lines represent the pseudo-second-order kinetic model descriptions.	79
4.6	Schematic representation of 2D hexagonal mesoporous structure of SMC (left) and the interconnected nanorod structure of CMK-3 (right).	80
4.7	Effect of particle size 62–88 μm (▲), 177–250 μm (●) and 510–700 μm (■), on the adsorption kinetics of 100 mg of AC (left) or SMC in 1 L of 60 mg/L BPA-solution (right).	81
5.1	Nitrogen sorption isotherms (left) and PSD (right) of AC and SMC-800-y materials.	88
5.2	SEM pictures (left) and TEM pictures (right) of SMC-800-0.83 (top) -0.50 (centre) -0.25 (bottom).	90
5.3	Powder X-ray diffraction patterns for AC and SMC-1200-y materials.	91
5.4	Nitrogen sorption isotherms for all SMC-x-y materials (left) and PSD (right).	93
5.5	Adsorption kinetics of 50 mg SMC-800-025 and AC in 500 mL 40 mg/L HA-solution at RT, 700 rpm and pH of 7. The pseudo-second order model (left) and the Weber-Morris model (right) were fitted to the data.	96
5.6	Adsorption isotherms of SMC-800-0.25, SMC-800-0.5 and AC with Langmuir fit, 10 mg of adsorbent was added to 50 mL HA-solution of various concentrations at 25 °C, 200 rpm for 7 days.	97
5.7	Zeta potential measurements at varying pH of AC, SMC-800-0.50 and SMC-800-0.25.	98
5.8	Influence of initial pH on the adsorption capacity of 10 mg SMC-800-0.25 in 50 mL HA-solution (40 mg/L) for 7 days at 25 °C and 200 rpm.	99
5.9	LC-OCD chromatograms of 50 mL HA-solution (80 mg/L) before (HA, blue line) and after adsorption for 7 days at 25 °C at 200 rpm, with 50 mg adsorbent (AC, short dash and SMC-800-0.25, long dash).	100
6.1	Raman spectra of synthesized (top) and pure NH_3BH_3 (bottom).	108
6.2	TGA curve of NH_3BH_3 at 10 °C/min in nitrogen atmosphere.	109

6.3	Reaction mechanism of h-BN from ammonia borane [7*]. Hydrogen abstraction by the evolution of molecular hydrogen at high temperature is assumed. **Reversibility between molecular aminoborane and PAB [178].	110
6.4	Powder X-ray diffraction patterns of commercial h-BN and BN from ceramization of pure NH_3BH_3 at 1400 °C, * = sample holder peaks.	110
6.5	Nitrogen sorption isotherms of CMK-3, CMK-3/BN and hard template BN-500 °C-air (left) with PSD (right).	111
6.6	TGA curves of CMK-3 and CMK-3/BN material at 10 °C/min in air.	112
6.7	Supramolecular structure of melamine diborate precursor.	114
6.8	Nitrogen sorption isotherms of the template-free BN-x materials.	116
6.9	Powder X-ray diffraction patterns of commercial h-BN and template-free BN-x, * = peaks from sample holder.	117
6.10	IR spectra of template-free BN-1700 and commercial h-BN.	117
6.11	SEM pictures of template-free BN-1700 with a clear lamellar structure of the slit shaped pores at 25k magnification (left) and 100k magnification (right).	118
6.12	Schematic representation of turbostratic and hexagonal BN.	118
6.13	TEM picture of template-free BN-1700 comprised of disordered h-BN sheets with an interplanar distance of 0.34 nm.	119
6.14	BPA adsorption capacities of BN-x after 1h, 4h and 24h adsorption time. 10mg of BN material was added to 100 mL of 60 mg/L BPA-solution, stirred at 200 rpm at 25 °C.	120
6.15	TPD curves of toluene from AC (black) and BN-1700 (red) heated at 30 °C/min to 400 °C.	121
6.16	TGA curve of BN-1700 heated at 10 °C/min in air.	122
6.17	Nitrogen sorption measurements of template-free BN-1700 after stability tests in air at 500 °C and in water.	123
8.1	Nitrogen sorption isotherm and pore size distribution (inset) for the mesoporous carbon with optimized S_{meso}	130
8.2	Schematic representation of microporous AC (left), 2D hexagonal mesoporous structure of SMC (middle) and the interconnected nanorod structure of CMK-3 (right).	131
8.3	Adsorption kinetics of 100 mg of CMK-3 (■), AC (●) and SMC (▲) in 1 L of 60 mg/L BPA-solution, particle size is between 62 and 88 μm , the error bars represent the standard deviation of the triplicate measurements, the dashed lines represent the pseudo-second-order kinetic model descriptions.	132
8.4	Nitrogen sorption isotherms (left) and pore size distribution (right) of AC and SMC carbonized at 800 °C with a p/s ratio of 0.83, 0.50 and 0.25.	133

8.5	Nitrogen sorption isotherms (left) of the template-free BN materials ceramized at 1400, 1600 and 1700 °C and PSD (right).	135
8.6	Stikstofsorptie isotherm en poriegroottedistributie voor mesoporeuze koolstof met geoptimaliseerd S_{meso}	137
8.7	Schematische voorstelling van microporeus AC, 2D hexagonal mesoporeuze structuur van SMC en de intergeconnecteerde nano-staaf structuur van CMK-3.	138
8.8	Adsorptiekinetiek van 100 mg van CMK-3 (■), AC (●) en SMC (▲) in 1 L van 60 mg/L BPA-oplossing, partikelgrootte tussen 62 en 88 μm , de foutenbalken zijn de standaardafwijkingen van de meting in drievoud opgemeten, de stippellijn stelt de pseudo-tweede-orde kinetiek fit voor.	139
8.9	Stikstofsorptie isothermen (links) en poriegroottedistributies (rechts) van AC en SMC gecarboniseerd bij 800 °C met een p/s verhouding van 0.83, 0.50 en 0.25	140
8.10	Stikstofsorptie isothermen (links) en poriegroottedistributies (rechts) van templaatsvrije BN materialen gesynthetiseerd bij 1400, 1600 en 1700 °C.	142

List of Tables

1.1	Overview of material characteristics of reported mesoporous carbons synthesized under different conditions or with different surfactants, p = phenol, f = formaldehyde, phlor = phloroglucinol, mel = melamine, Tan = tannin, fur = furfural, HMT = hexamethylenetetramine, DCD = dicyanodiamide, HT = hydrothermal, PS = phase separation, EISA = evaporation induced self-assemble, 2D hexagonal (p6mm), 3D cubic (Ia3d), 3D bicontinuous cubic (Im3m).	10
1.2	Material characteristics of various carbon adsorbents and their adsorption capacity for BPA. * All adsorption experiments were performed at pH 7.	28
1.3	Material characteristics of various carbon adsorbents and their adsorption capacity (q_{max}) for organic dyes (MO = methyl orange, RhB = rhodamine B). * All adsorption experiments were performed at pH 7.	29
1.4	Material characteristics of various carbon adsorbents and their adsorption capacity for Lysozyme. * All adsorption experiments were performed at pH 11.	31
1.5	Material characteristics of various carbon adsorbents and their adsorption capacity for humic acid. * All adsorption experiments were performed at pH 11.	31
3.1	Definitive screening design of 5 factors, with center values marked in bold.	53
3.2	Material properties of the mesoporous carbons of the DSD experiments.	56
3.3	Material properties of the reproduced syntheses of DSD9 and DSD11.	57
3.4	Model coefficients of the significant main, interaction and quadratic effects for the models S_{micro} , V_{micro} , S_{meso} , V_{meso} and wt% C, with their respective p-values.	59
3.5	Material properties of the mesoporous carbon and predicted values with optimized S_{meso}	64
3.6	Experimental adsorption capacities ($q_{e,exp}$) for the DSD materials and the optimal material and the predicted adsorption capacities $q_{e,pred}$ for the model with and without DSD 1, 8, 9.	65

4.1	Structural properties of the carbon adsorbents.	74
4.2	Elemental composition of the three carbon adsorbents.	76
4.3	The observed maximum adsorption capacity in mg/g and converted to molecules per nm ² , parameters describing the adsorption isotherms of BPA on AC, CMK-3 and SMC modeled by Langmuir and Freundlich.	77
4.4	Parameters of the pseudo-first-order, pseudo-second-order and Weber-Morris kinetic models for adsorption of BPA on AC, CMK-3 and SMC.	79
4.5	Parameters of the Weber-Morris kinetic model for adsorption of BPA on AC and SMC with different particle sizes.	81
5.1	Material characteristics of AC and SMC-x-y materials.	89
5.2	Experimental and predicted (Equation 5.2) adsorption capacities (10 mg adsorbent in 50 mL of 500 mg/L HA-solution, RT, 200 rpm, pH = 7), together with the significant material characteristics pore size D_p and wt% C.	94
5.3	Kinetic parameters for pseudo-second order and Weber-Morris model for SMC-800-0.25 and AC.	95
5.4	Langmuir and Freundlich parameters for SMC-800-0.25, SMC-800-0.5 and AC.	97
6.1	Material characteristics of CMK-3, CMK-3/BN and BN.	112
6.2	Properties of hard template BN after carbon removal at different temperatures in air.	113
6.3	CHNS analysis for the melamine diborate complex synthesized with melamine to boric acid.	115
6.4	Material characteristics of the template-free BN-x with ceramization at different temperatures.	115
6.5	Material characteristics of BN-1700 after stability tests.	123
8.1	Material properties of the mesoporous carbon and predicted values with optimized S_{meso}	131
8.2	Experimental and predicted adsorption capacities (10 mg adsorbent in 50 mL of 500 mg/L HA-solution, RT, 200 rpm, pH = 7), together with the significant material characteristics pore size D_p and wt% C.	134
8.3	Materiaaleigenschappen van de mesoporeuze koolstof en de voorspelde waarden voor een geoptimaliseerd S_{meso}	138
8.4	Experimentele ($q_{e,exp}$) en voorspelde ($q_{e,pred}$) adsorptiecapaciteiten (10 mg adsorbens in 50 mL of 500 mg/L HA-oplossing, RT, 200rpm, pH = 7), samen met de significante materiaaleigenschappen: poriegrootte D_p en wt% C.	141

List of Abbreviations

AC	Activated carbon
APS	Ammonium persulfate
BET	Brunauer Emmett Teller
BJH	Barret Joyner Halenda
BN	Boron nitride
BPA	Bisphenol A
CMK-3	Carbon Material of Korea
CTF	Covalent triazine framework
CT	Chestnut tannin
CTAB	Cetyl trimethylammonium bromide
DCBP	4,4-Biphenyldicarbonitrile
DCD	Dicyanodiamide
DoE	Design of Experiments
DSD	Definitive Screening Design
DRIFT	Diffuse Reflectance Infrared Fourier Transform
EISA	Evaporation induced self-assembly
FDU	Fudan University
HA	Humic acid
HMT	Hexamethylenetetramine
HT	Hydrothermal
h-BN	Hexagonal boron nitride
IUPAC	International union of pure and applied chemistry
IR	Infrared Spectroscopy
KIT-5	Korean Institute for Technology
LC-OCD	Liquid chromatography organic carbon detection

Lz	Lysozyme
MCM	Mobil catalytic material
MO	Methyl orange
MW	Molecular weight
P4VP	Poly-4-vinylpyridine
PCL	Polycaprolacton
PEG	Polyethylene glycol
PET	Polyethylene terephthalate
PEO	Polyethylene oxide
PMMA	Polymethylmethacrylate
PPO	Polypropylene oxide
P/S	precursor to surfactant ratio
PS	Polystyrene
PSD	Pore size distribution
PZC	Point of zero charge
RT	Room temperature
RH	Hydrodynamic radius
RhB	Rhodamine B
SBA	Santa Barbara University
SEM	Scanning electron microscopy
SMC	Soft templated mesoporous carbon
t-BN	Turbostratic boron nitride
TEM	Transmission electron microscopy
TEOS	Tetraethylorthosilicate
THF	Tetrahydrofuran
TMAB	Trimethylaminoborazine
TMB	1,3,5-Trimethylbenzene
UV	Ultra violet
VOC	Volatile organic compound
XRD	X-ray diffraction spectroscopy
XRF	X-ray fluorescence spectroscopy

1.1 Preface

Environmental pollution from various sources has become an increasing problem over the last several decades. One of the major global issues is the pollution of water. Water is a vital resource for all known forms of life and a necessity for the sustainability of earth's ecosystems. Water availability is affected by pollution caused by intensive agriculture, industrial production, mining and untreated urban runoff and wastewater. This pollution creates environmental and health risks [1]. The availability and access to pure water as a natural resource are therefore crucial for human health, agriculture, industry and natural ecosystems [2].

Organic pollutants are an important group of hazardous compounds contaminating water [3]. Efficient techniques for the removal of organic compounds from water have drawn significant interest. A number of methods such as adsorption, coagulation, filtration with coagulation, precipitation, ozonation, reverse osmosis and advanced oxidation processes have been used for the removal of organic pollutants from polluted water and wastewater. Most of these methods have been found to be limited, since they often involve high capital and operational costs. Among the possible techniques for water treatments, adsorption shows potential as one of the most efficient methods because of its simple design and low initial cost. [4].

Activated carbon (AC) is the most widely used commercial adsorbent to remove organic pollutants from wastewater due to its porous structure and high specific surface area [5]. However, AC is less suitable for the adsorption of pollutants with larger molecular size (e.g. bulky molecules or macromolecules). The inherent micropores (< 2 nm) are less accessible or even unable to host these large molecules leading to lower adsorption capacities.

Mesoporous adsorbents on the other hand are materials with a pore size between 2 and 50 nm. These larger pore sizes will be advantageous in the adsorption of larger molecules. Interesting materials are mesoporous carbons, originally synthesized via a hard template route, in which a mesoporous silica is used as a template. This template was filled with carbon precursor which is polymerized in the pores. After template removal, porosity is created [6]. A more recently developed soft template method uses the interaction of carbon precursors with a micelle-forming surfactant to synthesize mesoporous carbons. A treatment at high temperatures in an inert atmosphere removes the surfactant, creating porosity in the mesoporous carbon [7]. This method involves less synthesis steps and does not require a hard template, which needs to be removed with dangerous HF. The versatility in reaction conditions of soft templated mesoporous carbons can lead to a broad range of carbons in which the material properties can be tailored to specific needs.

Another novel mesoporous material gaining interest as adsorbent is hexagonal boron nitride which is known for its chemical and thermal stability. It has a similar chemical structure to graphite which allows the successful adsorption of organic pollutants. With the introduction of porosity into this material, a chemical and thermal stable efficient adsorbent could be obtained.

In summary, the need for a cleaner environment and efficient ways to remove pollutants from water requires the development of better adsorbents. In order to address new challenges, tailor-made adsorbents need to be developed to meet specific requirements. A fundamental understanding in the design of new mesoporous materials with control over material properties, e.g. specific surface area, pore volume, pore size or surface chemistry is crucial to efficiently remove organic pollutants from water.

1.2 Outline

In **Chapter 1**, an extensive review and introduction on the synthesis of soft templated mesoporous carbons is discussed. The different synthesis steps and components and their effect on material characteristics are addressed. The use of soft templated mesoporous carbons as adsorbents for a variety of pollutants is evaluated.

In **Chapter 2**, the main analysis techniques to characterize the mesoporous materials are described.

Chapter 3 reports on a structural approach to identify the effect of different synthesis parameters on the material properties of soft templated mesoporous carbons. Therefore, a new type of design of experiments was employed: a definitive screening design (DSD). This design was used to obtain the models that predict the effect of significant synthesis parameters on the material properties. Optimal conditions to maximize the mesoporous surface area were derived from the model and were tested and validated. All the mesoporous carbons were tested for the adsorption of bisphenol A (BPA). In this way the significant effects of material properties on the BPA adsorption were detected.

Chapter 4 elaborates on the adsorption of BPA. In this chapter, three porous carbons with varying material characteristics were tested for BPA adsorption. Both equilibrium as well as kinetic studies of BPA adsorption were performed for a soft templated mesoporous carbon, a hard templated mesoporous carbon and a commercial activated carbon.

Chapter 5 introduces a new way to synthesize large pore mesoporous carbon via the acid catalyzed EISA synthesis. These large pores opened up new possible adsorbate types to be removed from water. The ability of soft templated mesoporous carbons to remove humic acid (HA) was investigated. Both equilibrium as well as kinetic studies were performed with soft templated mesoporous and activated carbon.

Chapter 6 provides some insights into the synthesis of porous boron nitride (BN). BN has recently shown to be a promising new adsorbent type. A hard template BN synthesis method, in which ammonia borane is impregnated into CMK-3 and a template-free BN synthesis in which melamine diborate is transformed into porous BN are investigated. Their material characteristics were evaluated and some preliminary adsorption experiments for BPA were performed.

Chapter 7 summarizes the most important conclusions from this work and provides some perspectives for further research and developments.

1.3 Mesoporous carbons

The discovery and development of mesoporous carbons provided a new material with attractive properties, including high specific surface area and large pore volume, tunable pore sizes and geometries in combination with a good chemical and mechanical stability. These unique properties introduce an abundance of application possibilities in the field of catalysis, electrochemistry, separation and adsorption [8–14]. Mesoporous carbon indicates a pore size between 2 and 50 nm, this is in contrast with conventional porous carbons, such as activated carbon, which are often limited to micropores ($< 2\text{nm}$). Most mesoporous carbons have a combination of micro- and mesoporosity, and in rare cases the pore size can be enlarged to macropores ($> 50\text{nm}$). Mesoporous carbons were first developed via an indirect synthesis or hard template route by Ryoo et al. [6, 14] with mesoporous silica as template. With an already large existing family of porous silica and emerging variety of mesoporous oxides available to use as template, the resulting negative replica of mesoporous carbons is evenly extensive [12, 15, 16]. To overcome some negative aspects of this synthesis, such as multiple synthesis steps, the morphology being limited to the used template and the use of hazardous HF or NaOH, the direct synthesis or the soft template route was investigated.

The soft template route is based on micelle templating in which the structure-directing polymer provides the driving force for micelle formation. The carbon precursor, mostly phenol or resorcinol in combination with formaldehyde, must have a strong interaction with one of the blocks of the block copolymer acting as micelle forming surfactant. This interaction can be a hydrogen bonding or electrostatic interaction ($I^+X^-S^+$) between the precursor and the surfactant under very acidic conditions [17, 18]. In a next step, the carbon precursor must be able to polymerize and cross-link around the micelles to create the framework. Finally, the cross-linked polymer is transformed into a mesoporous polymer or resin at temperatures below $600\text{ }^\circ\text{C}$. Further heating to temperatures of $600\text{ }^\circ\text{C}$ and higher, under inert atmosphere, will result in a mesoporous carbon. The micelle-forming surfactant is decomposed at these temperatures and removed creating the desired mesoporosity.

The flexibility of the soft template synthesis has resulted in the search for novel precursors, surfactants, and reaction conditions. The selection of both precursor and surfactant, their ratio, acid or base catalyzed synthesis, synthesis route (EISA, phase separation or hydrothermal) and carbonization temperatures are variables which greatly influence the material characteristics of the mesoporous carbon. New types of, or enhanced, mesoporous carbons further strengthen their potential use in various applications. The unique physical and chemical properties of mesoporous carbons such as large specific surface area, large pore volume, pore size control and tuning of the hydropho-

bicity are especially advantageous in adsorption applications. Introducing mesopores (2-50 nm) was crucial in the adsorption process of various larger organic molecules [19–22], obtaining a rigorous control of the pore size enabled the adsorption of even the largest pollutants e.g. enzymes, humic acids, etc. [23–25].

The focus of this introduction is on the recent developments in soft template synthesis of mesoporous carbons and specifically the ability to fine-tune the pore size and pore size distributions. The variation in synthesis methods is addressed systematically by the following sequence: a) precursors, b) surfactants, c) precursor surfactant ratio, c) acid or base catalyst, d) synthesis route, e) carbonization temperature and f) surface modification. From the various applications of mesoporous carbons, an overview of the use as an adsorbent is presented. The versatility of mesoporous carbon characteristics, e.g. pore size, symmetry and surface modifications, are summarized and their effect on the adsorption performance of different pollutants evaluated.

1.3.1 Precursor types

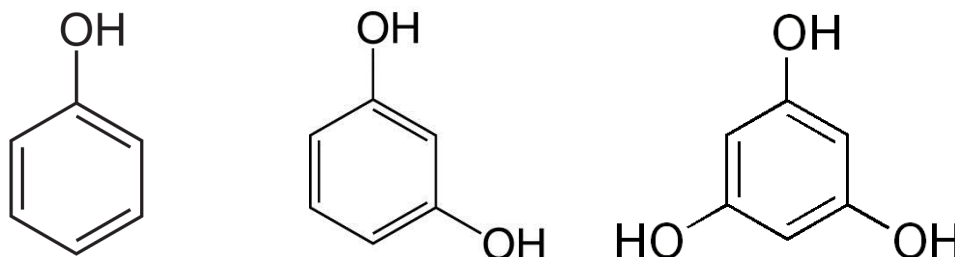


FIGURE 1.1: Carbon precursors: phenol, resorcinol (benzene-1,3-diol) and phloroglucinol (benzene-1,3,5-triol).

Phenol, resorcinol and phloroglucinol are frequently used phenolic resin monomers for the synthesis of mesoporous carbons. These aromatic compounds (Figure 1.1) with respectively one, two and three hydroxyl groups can form hydrogen bonds with the polyethyleneoxide (PEO) chains of the surfactants. These interactions enable the organic-organic self-assembly. Phenol is most often chosen as starting reagent due to its low cost price and the easy control over the polymerization rate. The reactivity of these monomers increases with the number of hydroxyl groups: phloroglucinol > resorcinol > phenol. Liang et al. discovered that the polymerization of phenol was very

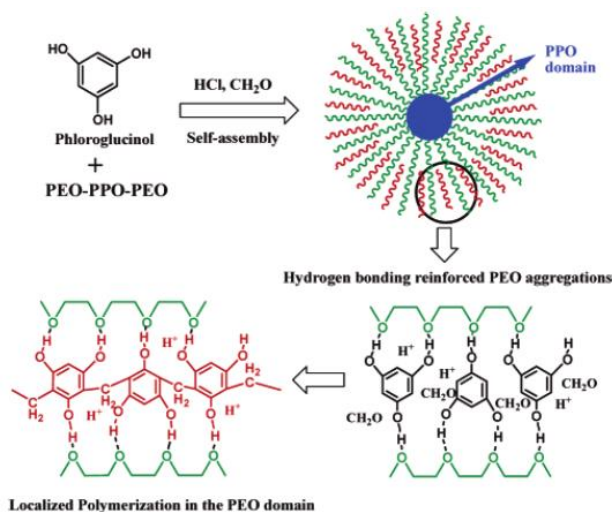


FIGURE 1.2: Self-assembly of phloroglucinol with PEO segments via H-bonding for better ordering of the mesostructure [26].

slow in the presence of the PEO-PPO-PEO surfactant F127 with HCl concentrations below 10^{-2} M: it took about two to three weeks to precipitate the phenol/formaldehyde polymer at room temperature [26]. The resulting polymer yielded porous carbons with very low surface areas (< 5 m²/g). Resorcinol polymerized slightly faster than phenol. The polymerization time of resorcinol at room temperature was about one week. Phloroglucinol, however, polymerized much faster than either resorcinol or phenol. It took only about 40 min to a few hours to polymerize phloroglucinol. This implies that the high hydroxyl density in the oligomers formed from phloroglucinol provides a greater driving force for the self-assembly interaction with the PEO blocks (Figure 1.2), as compared with those provided by the oligomers from phenol and resorcinol [26]. Interestingly, the phloroglucinol carbon was processed in three different ways to form monolith, fiber and film morphologies. These resulted in specific surface areas of 378, 593, and 569 m²/g and corresponding average pore sizes of 9.5, 6.1, and 5.4 nm, respectively. The monolith formation was performed by curing the polymer as synthesized, while applying shear stress for the fiber and film extrusion resulted in more ordering and a smaller pore size.

The use of green chemicals or valorization of waste materials for mesoporous carbon synthesis is growing. This can reduce the material cost or make it more environmentally friendly by replacing toxic precursors phenol

and resorcinol. These plant-based precursors are composed out of a phenolic-type structure, but are often much larger or contain extra functional groups as seen in Figure 1.3. Larch was used to synthesize a carbon foam with bimodal micro/mesopores by Liu et al. by liquefaction, resinification, foaming and carbonization at different temperatures [27]. An extra activation step with KOH was performed to create a 3D network and a ligament/pore structure was developed. The pores were 2.1 and 3.9 nm in diameter with surface areas from 554 m²/g up to 1918 m²/g [27]. Another naturally occurring precursor that has been explored is tannin. Due to the high amount of hydroxyl groups of their flavonoid subunits, these cheap and non-toxic biopolymers enhance hydrogen bonding with the hydrophilic corona of the triblock copolymers PEO-PPO-PEO which resulted in an ordered 2D hexagonal mesoporous carbon with a pore size of around 8 nm [28]. Further advances were made with chestnut tannin (CT). By varying different synthesis parameters e.g. the ratio CT to F127, pH or reaction time a variety of mesoporous carbons were synthesized. The surface areas ranged from 242 m²/g to 420 m²/g. Varying the ratio CT to F127 from 1 to 2.38 changed the morphology from lamellar to 2D hexagonal with corresponding pore sizes of 17 nm and 7.5 nm [29].

A larger precursor that has been used is lignin (Figure 1.3), it is a well-known biopolymer and obtained as a co-product from pulping industries and biorefineries. Saha et al. recently used it successfully as carbon precursor in combination with the F127 surfactant. They compared it with a typical phenol-based mesoporous carbon synthesis. The mesoporous carbon with phenol precursor showed narrow pore size of typical 4 to 6 nm, whereas the pore size of lignin based mesoporous carbons showed a much wider pore size distribution of 3 to 10 nm. The BET specific surface areas were respectively 400 m²/g and 205 m²/g. The lower porosity for the lignin based carbon can be attributed to the heterogeneous molecular architecture and highly branched structure of lignin, which causes imperfect self-assembly of surfactant micelles in the randomly cross-linked matrix and results in poor material characteristics [30].

Furfural, often used as a carbon precursor in hard template synthesis, was also successfully used in a soft template route. It was used in combination with resorcinol and hexamethylenetetramine (HMT), a known replacement for formaldehyde, to synthesize mesoporous carbons with pore sizes around 3.5 nm [31].

Different possible alternatives for the toxic formaldehyde have been studied as well. The combination of phloroglucinol with the slower reacting glyoxal precursor in presence of F127 led to ordered carbons with a pore size of 7.5 nm. The use of hexamethylenetetramine (HMT) has the ability to produce formaldehyde and ammonia upon hydrolysis. Ammonia could catalyze

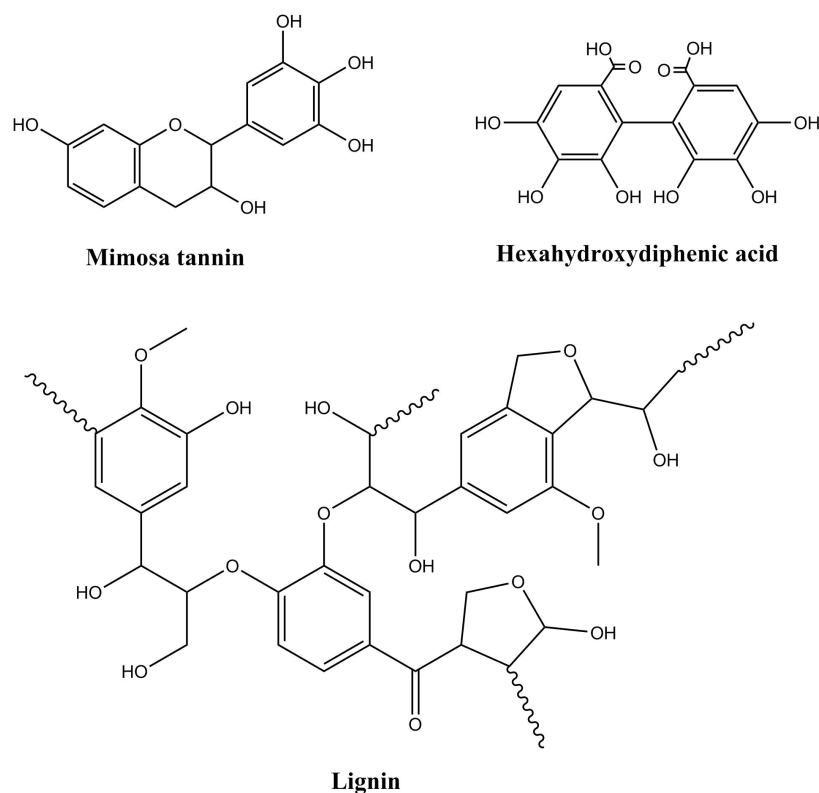


FIGURE 1.3: Biosourced precursors: tannin, a main component of larch sawdust; hexahydroxydiphenic acid and an example of a possible lignin structure.

the polymerization reaction of resorcinol and formaldehyde and initiate their condensation process [32]. Together with a range of PEO-PCL surfactants where the polycaprolactone (PCL) chain was increased in size, carbons with pore sizes from 6.8 to 15.6 nm were synthesized. Huang et al. also used HMT to replace formaldehyde [33]. They synthesized a 2D hexagonal and 3D cubic carbon by changing the precursor to surfactant (p/s) ratio from 1.2 to 2.4, which resulted in mesoporous carbons with a pore size of 3 to 4 nm.

In the search for nitrogen doped mesoporous carbons, nitrogen rich precursors e.g. melamine, dicyandiamide or urea are used instead of, or together with the traditional phenol or resorcinol precursors. These nitrogen doped mesoporous carbons can be used as catalysts, supercapacitors or adsorbents for CO₂ or acid gasses [34–37]. By mixing melamine with phenol and F127, N-doped mesoporous carbons were synthesized. A pore size of 6 nm was obtained. By increasing the amount of melamine in comparison to phenol the pore size shifted to 8 nm as seen in Table 1.1. More nitrogen was introduced by increasing the melamine amount. Elemental mapping showed a good dis-

persity of the N-functionalities which could serve as supercapacitors [35]. The combination with resorcinol was also investigated by Yu et al. which resulted in a cubic Im3m mesoporous carbon with uniform pore size of 3 nm and almost 3 wt% of N [37]. A melamine formaldehyde carbon was synthesized with CaCl_2 as pore creating template by Huang et al., this resulted in pores of 4, 9 and also 30 nm. High specific surface areas and pore volumes of $1290 \text{ m}^2/\text{g}$ and $2.33 \text{ cm}^3/\text{g}$ respectively, were observed [38]. A second N-precursor is dicyandiamide (DCD). DCD is able to interact with resorcinol and formaldehyde and is incorporated in the 2D hexagonal mesoporous carbon structure. Increasing the amount of DCD introduced more nitrogen in the structure up to 2.3 wt%. The pore size was around 8.5 nm for materials carbonized at 350°C and 6.1 nm when the temperature was 800°C [39]. A third N-precursor is urea, which was added to a phenol, formaldehyde and F127 system by Chen et al.. The hydrothermal synthesis resulted in 1.3 wt% N carbon nanospheres of 230 nm, which showed a cubic pore network with uniform small pores of 2.8 nm. Formaldehyde could also be replaced by HMT to obtain a N-doped mesoporous carbon. Resorcinol, HMT, ammonia, ureum and F127 resulted in an ordered cubic structure with pore size of 3 nm [37].

1.3.2 Surfactant types

An ideal template surfactant should have a strong interaction with both precursors and can be easily removed. The first surfactants used were cationic quaternary ammonium compounds (e.g. CTAB or hexadecyl trimethyl ammonium bromide). The use of these surfactants in combination with phenol or resorcinol-formaldehyde precursors led to disordered mesostructures with a wide pore size distribution or collapse of the mesostructure. This instability was attributed to the uncontrollable polymerization of organic precursors, difficulties of removing the micelles formed by the cationic template without damaging the pore structure and the weak interaction between the quaternary ammonium and the organic polymer precursors.

Table 1.1: Overview of material characteristics of reported mesoporous carbons synthesized under different conditions or with different surfactants, p = phenol, f = formaldehyde, phlor = phloroglucinol, mel = melamine, Tan = tannin, fur = furfural, HMT = hexamethylenetetramine, DCD = dicyanodiamide, HT = hydrothermal, PS = phase separation, EISA = evaporation induced self-assembly, 2D hexagonal (p6mm), 3D cubic (Ia3d), 3D bicontinuous cubic (Im3m).

Material	Precursor type	Surfactant type	P/S ratio	Synthesis pathway	Carb. Temp. (°C)	Ordering	S_{BET} (m^2/g)	V_{tot} (cm^3/g)	D_p (nm)	Ref.
FDU-14-800°C	p/f	P123	0.92	HT	800	3D (Ia3d)	690	0.34	2.0	[7]
FDU-15-800°C	p/f	F127	0.61	HT	800	2D (P6mm)	720	0.40	3.1	[7]
FDU-16-800°C	p/f	F127	1.22	HT	800	3D (Im3m)	820	0.47	3.8	[7]
CS-6-700	Larch/p/f	F127	1/0.06	HT	700	/	410	0.291	2.84	[27]
0.8A80F50	Tan/f	F127		EISA	800	2D (P6mm)	315	0.29	16.3	[29]
F127/RF-0.5	R/fur	F127	2	EISA	900	3D (Im3m)	785	0.49	3.6	[31]
F127/RF-1.36	R/fur	F127	0.74	EISA	900	2D (worm)	657	0.91	7.4	[31]
NC	Mel,p/f	F127	1.46	HT	600	/	962	0.84	6.9	[35]
NC-H	Mel,p/f	F127	1.25	HT	600	/	850	0.81	8.6	[35]
NOMC-800	Mel/R/HMT/NH3	F127	0.616	PS	800	3D (Im3m)	631	0.326	2.71	[37]
NMC-1-1073	Mel/f	CaCl ₂	1.0	/	800	disordered	865	1.19	9	[38]
NMC-2-1073	Mel/f	CaCl ₂	0.5	/	800	disordered	1290	2.33	4,9,27	[38]
1.0DCD-RF-800	DCD,R/f	F127	0.714	PS	800	2D (P6mm)	556	0.47	6.0	[39]
N-OMCs-0.15	Ureum/P/f	F127	0.685	HT	600	3D (Im3m)	446	0.24	3.0	[34]

Material	Precursor type	Surfactant type	P/S ratio	Synthesis pathway	Carb. Temp.(°C)	Ordering	S_{BET} (m ² /g)	V_{tot} (cm ³ /g)	D_p (nm)	Ref.
FDU-18-800°C	p/f	PEO ₁₂₅ -PMMA ₁₄₄	0.416	EISA	800	3D (Fm3m)	1050	0.57	10.5	[40]
C-FDU-18-1	p/f	PEO ₁₂₅ -b-PS ₁₂₀	2.5	EISA	800	3D (Fm3m)	684	0.47	11.9	[41]
C-FDU-18-2	p/f	PEO ₁₂₅ -b-PS ₂₃₀	2.5	EISA	800	3D (Fm3m)	795	0.72	22.7	[41]
C-FDU-18-3	p/f	PEO ₁₂₅ -b-PS ₃₀₅	2.5	EISA	800	3D (Fm3m)	922	0.87	33.3	[41]
RFR-carbon	R/f	PS-P4VP	0.512	PS	800	2D (P6mm)	/	/	33.7	[42]
C-V-50-600	R/f	PEO-PBO-PEO	1.0	EISA	600	disordered	760	1.3	20	[25]
C-V-50-T-50-600	R/f	PEO-PBO-PEO+TMB	1.0	EISA	600	disordered	810	1.7	27	[25]
15C-1:1		F127	1	EISA	850	2D (channel)	455	0.78	10.2	[43]
15C-3:1		F127	0.33	EISA	850	2D (channel)	476	0.74	16.1	[43]
40C-1:1		F127	1	EISA	850	2D (channel)	466	0.71	9.6	[43]
40C-4:1		F127	0.25	EISA	850	3D (cage-like)	423	0.30	6.2	[43]
RF-F127(3)	R/f	F127	0.73	EISA	800	aggregated	563	1.3	56	[44]
RF-F127(9)	R/f	F127	1.1	EISA	800	3D connected	643	0.56	6.8	[44]
ST-citric acid	R/f	F127	0.66	PS	600	2D (P6mm)	741	0.59	6.12	[45]
ST-HCl	R/f	F127	0.66	PS	600	2D (P6mm)	694	0.68	7.92	[45]
PC-600	Phloro/f	F127 low acid	1.0	EISA	600	2D (P6mm)	420	0.82	8.6	[46]

To increase the interaction strength between precursors and surfactant, hydrogen bonding interactions were investigated. The commercially inexpensive triblock copolymers pluronics, P123, F127 or F108, consist of polyethylene oxide (PEO) ends and a polypropylene oxide (PPO) center which can have varying lengths as seen in Figure 1.4. They were first applied successfully for the synthesis of mesoporous silicas and subsequent research showed their potential for the synthesis of mesoporous carbons. Tanaka et al. reported ordered channel structured mesoporous carbons (COU-1) via the combination of the resorcinol/formaldehyde precursors with the F127 (EO₁₀₅PO₇₀EO₁₀₅) surfactant [47]. The addition of triethyl orthoacetate was needed to enhance the ordered structure. Following this success, the use of PEO-PPO-PEO type surfactants or pluronics was elaborately studied. Meng et al. investigated the effect of the different types (P123, F127 and F108) as well as the p/s ratio [7]. The low-molecular weight resol-precursor was first synthesized via the basic route, then mixed with the surfactant e.g. F127 in ethanol solvent, followed by an EISA procedure. The high amount of hydroxyl groups enabled a good interaction with the surfactant via hydrogen bonding. By changing the surfactant type and the p/s ratio, the lamellar, 2D hexagonal as well as 3D cubic structures were obtained. The pore sizes of 2D hexagonal FDU-15 and 3D cubic FDU-16 carbonized at 800 °C were respectively 3.1 and 3.8 nm [7].

By replacing the PPO segment with polybutylene oxide (PBO), a larger surfactant became commercially available, the triblock copolymer PEO-PBO-PEO or Vorasurf 504 as seen in Figure 1.4, which consists of (EO)₃₈-(BO)₄₆-(EO)₃₈. This led to the synthesis of mesoporous carbons with pore sizes around 20 nm. With addition of trimethylbenzene (TMB) the pore size increased to 27 nm. These large pores could facilitate the transport of large biomolecules, such as lysozyme, and the mesoporous carbons were tested as adsorbent for the latter [25].

Other than the typical PEO-PPO triblock copolymers, a diblock copolymer of PEO and polystyrene (PS) was successfully used to synthesize ordered ultra-large pore carbons. Deng et al. synthesized C-FDU-18 with PEO-b-PS as a surfactant resulting in a cubic structure and a pore size of 23 nm. A high surface area of 1510 m²/g and a large pore volume of about 0.7 cm³/g were obtained of which the majority was microporous [48]. By using PEO-b-PS amphiphilic diblock copolymers with various PS chain lengths as templates, carbons with tunable pore size between 12–33 nm were discovered. The molecular weights of the different PEO-b-PS surfactants were varied from 17900, 29700, and 37200 g/mol, corresponding to approximate molecular compositions of PEO₁₂₅-b-PS₁₂₀, PEO₁₂₅-b-PS₂₃₀ and PEO₁₂₅-b-PS₃₀₅. The obtained C-FDU-18-1, C-FDU-18-2 and C-FDU-18-3 carbons possess highly ordered fcc mesostructures with Fm3m symmetry and large pore sizes of respectively 11.9, 22.7 and 33.3 nm as seen in Figure 1.5 [41].

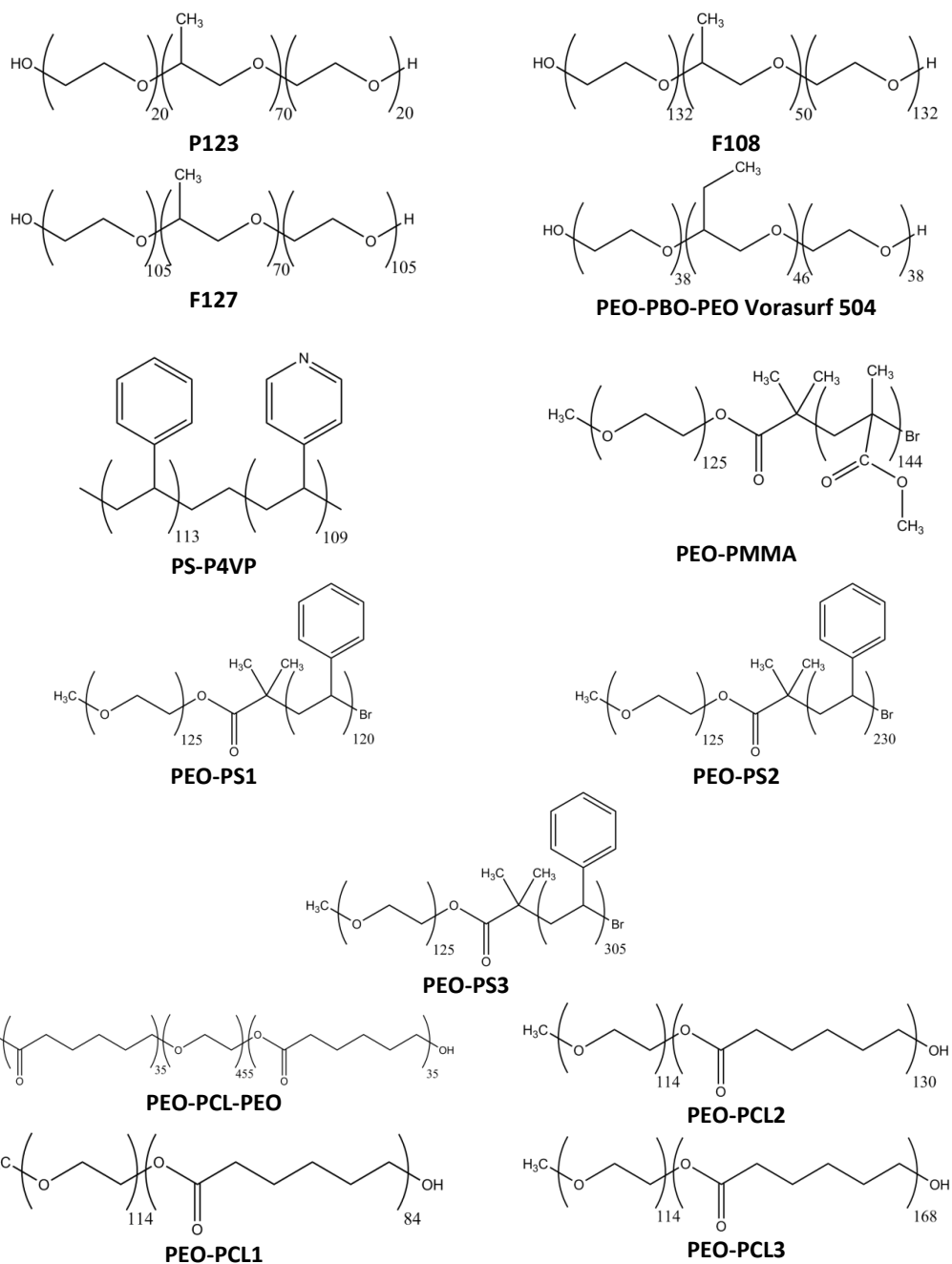


FIGURE 1.4: Different surfactant structures used for soft template mesoporous carbon synthesis.

A different surfactant, polyethyleneoxide-b-polycaprolacton (PEO-PCL) was used by Li et al. who synthesized different mesoporous resins with pore sizes of around 7, 9 and 11 nm by changing the amount of CL segments [32]. The use of larger diblock copolymer surfactants for highly ordered nanoporous carbon films was performed by Liang et al. [42]. First, the resorcinol monomers preorganized into a well-ordered nanostructured film with the assistance of polystyrene-block-poly(4-vinylpyridine) (PS-P4VP) self-assembly followed by the in situ polymerization of the resorcinol monomers with formaldehyde vapor to form ordered nanostructured films. The polystyrene-block-poly(4-vinylpyridine) was able to create ordered large mesopores of around 34 nm [42].

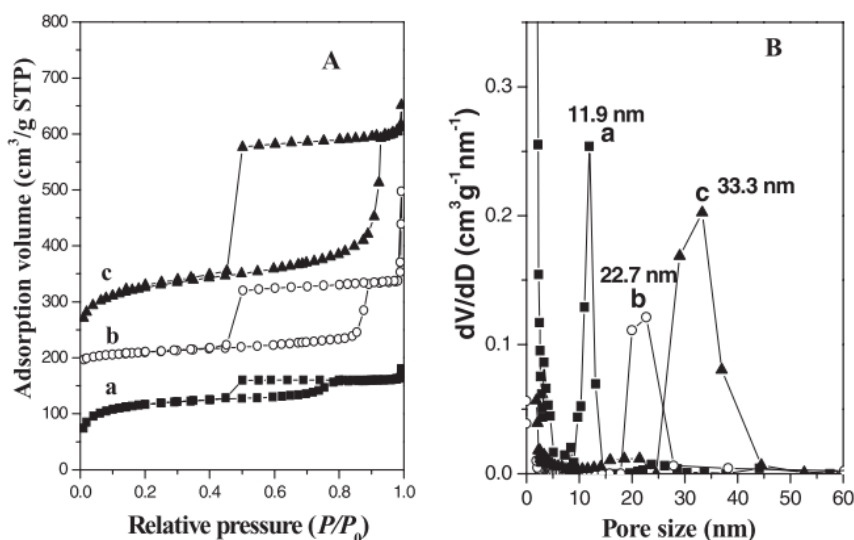


FIGURE 1.5: Nitrogen sorption isotherms (A) and pore size distribution (B) of (a) C-FDU-18-1, (b) C-FDU-18-2, and (c) C-FDU-18-3. The N_2 sorption isotherms of (a) C-FDU-18-1 are offset vertically by $-100 \text{ cm}^3/\text{g}$ [41].

Zhao et al. continued the investigation of different surfactant types and found a copolymer of polyethyleneoxide and polymethylmethacrylate ($\text{PEO}_{125}\text{-PMMA}_{144}$) [40]. This weakly hydrophobic surfactant resulted in mesoporous carbons with a pore size of about 10 nm. Interestingly due to the weak hydrophobicity of PMMA, the hydrophilic resol precursor was able to interact more than usual with the hydrophobic core of the surfactant. This resulted in thick wall mesoporous carbons and slightly disordered mesostructure. This weak hydrophobic templating process allows to tune the wall thickness, but could increase mechanical/chemical stability as well.

With every micelle-forming surfactant there is a possibility to increase the size of the hydrophobic core. The interfacial curvature will be changed by addition of hydrocarbon molecules, e.g. hexadecane or trimethylbenzene (TMB). These swelling agents will migrate to the hydrophobic core and cause swelling, which can cause pore size alterations or even phase changes. Zhang et al. reported a phase change from the highly ordered mesoporous carbons with body-centered cubic Im3m structure (FDU-16) with a pore size of 3.2 nm to mesoporous carbons with highly ordered 2D hexagonal p6m structure (FDU-15) in the aqueous synthesis process by addition of a short-chain hydrocarbon such as decane. The latter may have a strong interaction with the PPO segment of amphiphilic triblock copolymers and yield a larger pore size of 6.8 nm [49]. For PEO-PBO-PEO, the addition of TMB increased the pore size from 20 nm to 27 nm as seen in Table 1.1 [25]. The most direct way to influence the pore size of soft templated mesoporous carbons is changing the type of surfactant. The traditional block copolymers P123, F127 or F108 mostly result in carbons with pore size between 3 and 10 nm. The discovery of new types of surfactant, see Figure 1.4, allows for an increase in hydrophobic core size formed during the micelle formation and will result in larger pore sizes from 10 nm up to 30 nm. The ability to fine-tune the surfactant will result in a good regulation of the pore size. The use of hydrophobic bulky molecules known as swelling agents can often further enlarge the pore size with a few nm.

1.3.3 Precursor to surfactant ratios

In an intensive study by Meng et al., three different surfactants were tested (F127, P123 and F108) at varying precursor to surfactant ratios [7]. Changing the ratio between 0.5 and 2.5 resulted in lamellar, 2D-hexagonal, 3D bicontinuous (Ia3d), body centered cubic (Im3m) symmetries as seen in Figure 1.6. The change in phenol to template ratio or the higher amount of PEO segments in the surfactant causes a change in the hydrophilic/hydrophobic ratio of the resol-surfactant mesophase and therefore change of the interfacial curvature [50, 51]. This change forces the mesophase into another symmetry as seen in Figure 1.6. For F108 only the Im3m symmetry was observed. P123 and F127 can form Im3m, p6m, Ia3d and even lamellar symmetry depending on the p/s ratio as shown in Figure 1.6. Low p/s ratios for F127 resulted in a more 2D hexagonal (p6m) structure, higher ratio changed the symmetry to cubic (Im3m). For the FDU-type materials, all pore sizes were between 2 and 7.4 nm, however no clear correlation between pore size and p/s ratio (phenol to template) was observed.

The phloroglucinol formaldehyde F127 system was evaluated by Gorka et al. [43]. They varied the p/s ratio from 1 to 0.25 at different synthesis temperatures of 15 °C to 40 °C as seen in Table 1.1. At low reaction temperatures of

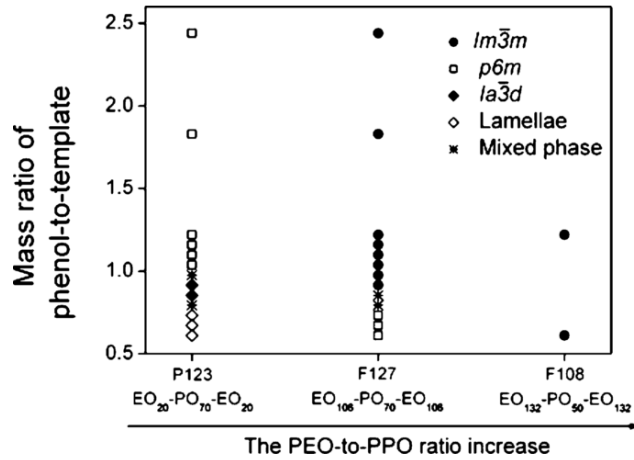


FIGURE 1.6: Influence of surfactant type and p/s ratio on ordering of the mesoporous carbon [7].

15 °C the shift from p/s ratio 1 to 0.33 increased the pore size from 10 nm to 16 nm, together with broadening the PSD. At reaction temperatures of 40 °C, the same ratio change varied the pore size from 9.6 nm to 7.8 nm, with a morphology change from worm-like to a cage-like structure [43].

Long et al. investigated the effect of resorcinol-furfural to F127 ratios, they reported the same effect of changing p/s ratio on the interfacial curvature. The resorcinol-furfural oligomers rather mix with the more hydrophilic PEO blocks than with the hydrophobic PPO ones. This causes a swelling of the hydrophilic volume and forces the hydrophilic/hydrophobic interface towards a low interfacial curvature. The quantity of oligomers is a dominant parameter which controls the swelling of the PEO blocks and thus the successful self-assembly of the mesophase. To obtain a well-defined symmetry the reaction time should be short enough to limit the polymerization degree of the oligomers or the hydrophilic properties should be improved [31]. The lower precursor to surfactant ratio together with a high amount of furfural to resorcinol ratio led to an increase in pore size from 3 nm to 7 nm. The symmetry of the mesopores shifted from a 3D cubic to a worm-like 2D hexagonal structure.

It seems that p/s ratio does not only effect the symmetry of the material, it can also affect the resulting pore size. In the resorcinol formaldehyde and F127 system, a typical 7 nm pore size was increased up to 12.5 nm by chang-

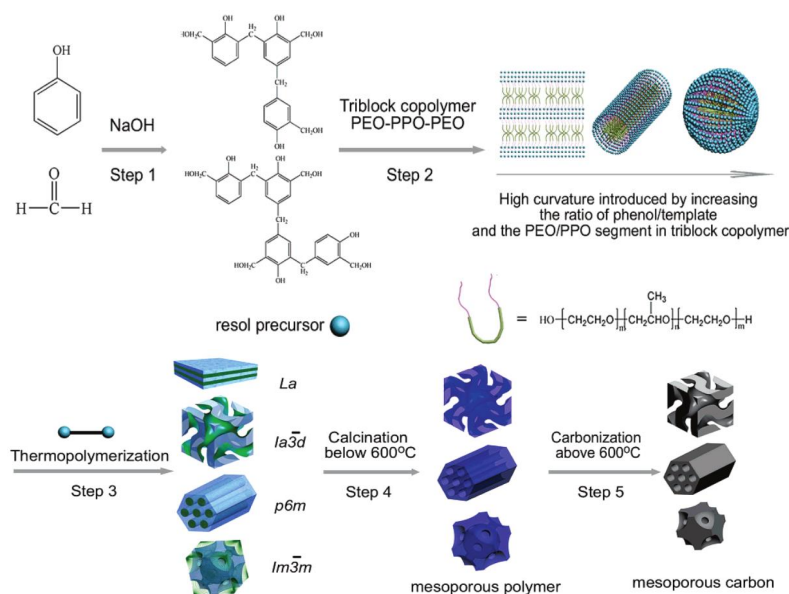


FIGURE 1.7: Schematic representation of mesoporous polymer and carbon synthesis with different morphologies depending on the p/s ratio or type of surfactant used [7].

ing the p/s ratio and polymerization time [52]. A recent study indicated that the change of p/s ratio together with the water/ethanol ratio increased the pore size from 7 nm up to 56 nm. Mitome et al. observed that, when low p/s ratios are used together with a low water/ethanol ratio, a very high interfacial curvature was obtained, resulting in an inversion of the micelles [44]. This shifts the symmetry from a small pore 3D connected framework to a large pore aggregated particle structure. With high water/ethanol ratios, the structure returned to the standard 7 nm 3D connected framework [44]. The interfacial curvature was paramount in the control over symmetry of the mesophase. For F127 lower p/s ratio led to a shift from 3D cubic to 2D hexagonal structure. Altering the pore size can be achieved in various changes of specific reaction conditions e.g. p/s ratio, water/ethanol ratio, reaction or carbonization temperature.

1.3.4 Acid or base catalysts

The polymerization of the carbon precursors can be catalyzed with a base or an acid. Via an acidic route, the addition proceeds first via an electrophilic aromatic substitution reaction. Acid catalyzed reactions with an excess of phenol to formaldehyde form novolacs as seen in Figure 1.10. These are long linear or slightly branched polymer chains, in which the monomers are linked together via methylene bridges. The basic route will first deprotonate the

phenol, which leads to a resonance stabilized phenoxide ion, which is followed by a formaldehyde substitution. After formaldehyde addition, prepolymer formation occurs by the condensation reaction between methylolphenols or condensation with phenol as seen in Figure 1.8.

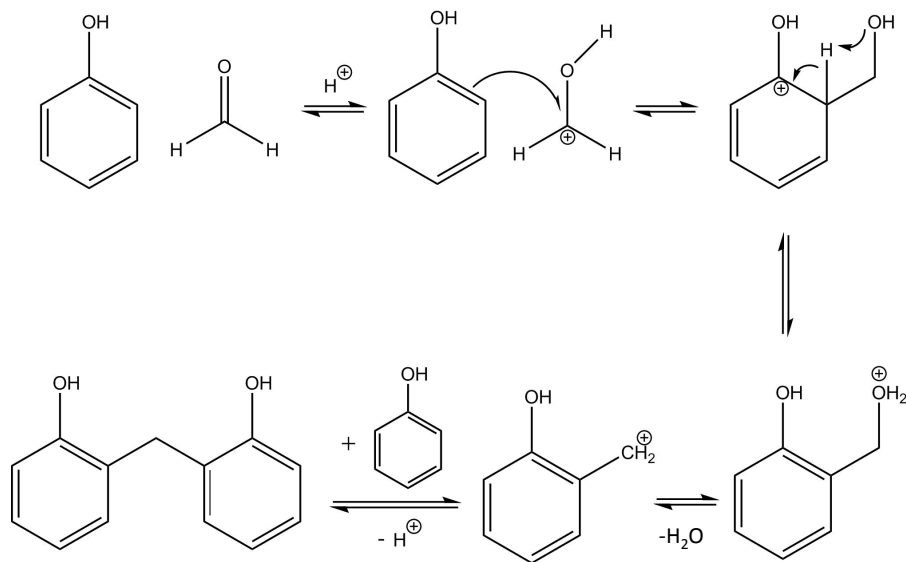


FIGURE 1.8: acid catalyzed reaction mechanism.

Base catalyzed reactions with an excess of formaldehyde to phenol, form resols. This oligomer consists of both methylene and ether bridges, which make resols soluble in organic solvents. When following the basic route, the resol is prepared in a first separate synthesis step, which leads to low molecular weight polymers. In a second step at neutral pH the resol is redissolved in ethanol and mixed with the surfactant. [49, 53, 54]. Both resols and novolacs will transform into a similar type of 3D interconnected polymer network [55].

The polymerization of phenolic resins via the acid or base catalyzed reaction is mostly performed with HCl [18, 46, 56] or NaOH [57]. The pore size is controlled by the surfactant or p/s ratio and the pore size is mostly between 3 and 10 nm. Liu et al. investigated the effect of HCl in a phloroglucinol/formaldehyde/F127 system. A higher acid concentration increased the pore size from the often reported 8.6 nm to 19.2 nm with a broad pore size distribution. These authors suggested that the faster reaction rate due to the high acid concentration resulted in high-molecular-weight phloroglucinol and formaldehyde polymer particles. These particles were scattered and disorderly

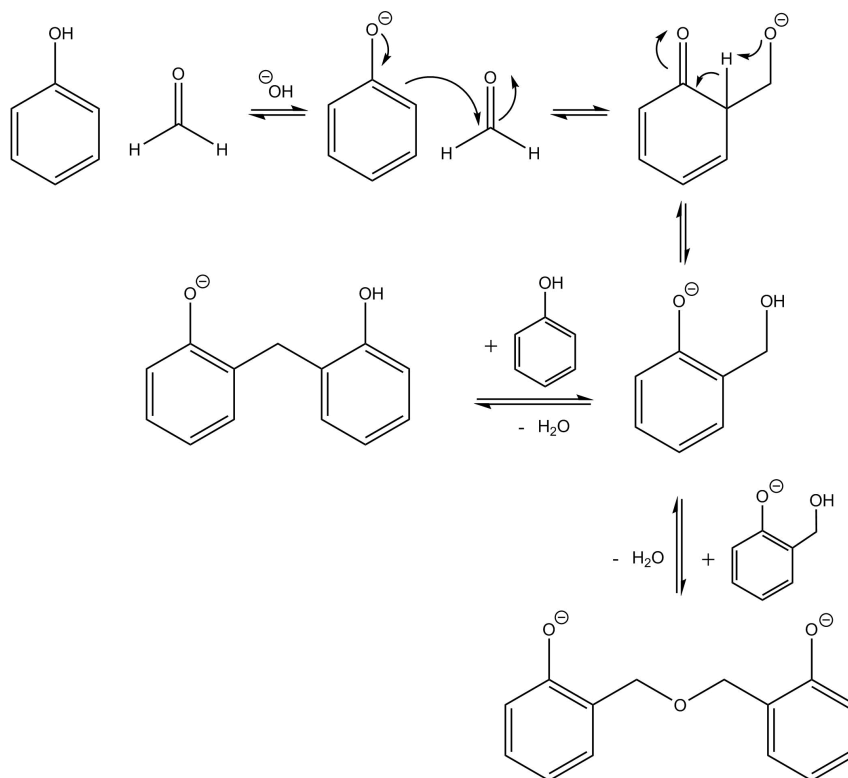


FIGURE 1.9: base catalyzed reaction mechanism.

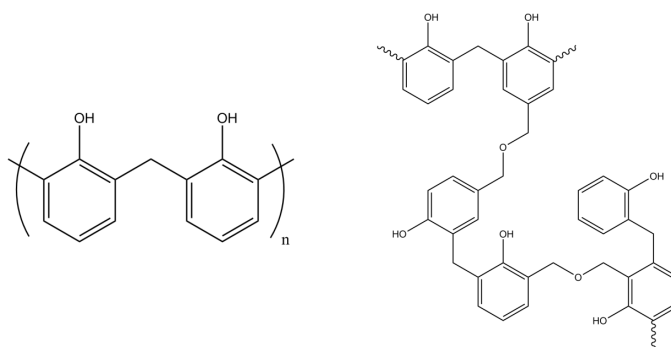


FIGURE 1.10: Novolac structure (left) and resol structure (right) before curing into 3D interconnected polymer.

distributed around the template micelles as seen in Figure 1.11, instead of assembling with the PEO segments and thus increasing large pores throughout the material [46].



FIGURE 1.11: A possible mechanism of ultra-large pores creation in mesoporous carbons by varying acid concentration [46].

Some efforts have been done to find a greener alternative to HCl or NaOH. Examples are amino acids, e.g. glutamic acid, lysine or weak organic acids. Lysine can act as an organic base as well as a mesophase promoter. Lysine molecules can form intra-molecule salt, so the deprotonated carboxyl group and the protonated amine group can form hydrogen bonds with the $-OH$ group of resorcinol and the hydrophilic ethylene oxide ($N-H...O$) of F127. The average pore size was about 6 nm. By doubling the amount of lysine, the pore size increased to 15 nm with a broad pore size distribution [58]. Glutamic acid was also studied as a catalyst. It simultaneously initiated the reaction and enhanced interaction between the R/f polymer and F127 through hydrogen bonding. With pore sizes of around 6 nm, a small difference with the pore size of mesoporous carbon with HCl (7-8 nm) was observed [59]. Choma et al. validated this difference when studying a group of weak organic acid catalysts: citric, acetic, oxalic, succinic and benzoic acid gave pore sizes of around 6.0 nm where HCl resulted in 7.92 nm, which seems to indicate that higher acidity favors the formation of larger micelles [45]. A multitude of acids and bases can be used to catalyze the polymerization of the carbon precursors. High concentrations of catalyst resulted in very fast polymerization of the precursor which led to a disordered pore structure but enabled the synthesis of large pores up to 20 nm.

1.3.5 Synthesis pathways

Three different pathways are most commonly used for synthesizing mesoporous carbons as seen in Table 1.1. A first route is the hydrothermal aqueous pathway. The hydrothermal route consists of a batch process in which the carbon precursor and surfactant react in aqueous solution [55,60]. The synthesized resin FDU-15 had a pore size of 3.8 nm with medium specific surface area of 550 m²/g and pore volume of 0.4 cm³/g. The resin had a small amount of mesoporosity. Upon full carbonization to C-FDU-15, these mesopores shrunk from 3.8 nm to 2.7 nm [61]. Often long reaction times (> 100h) and a very precise pH control are needed. A pH of about 9.0 is required to obtain a rigid and stable mesoporous framework. The high pH weakens the hydrogen bonds, however, reaction in neutral or weak acidic media is too slow, making the narrow pH range a limitation of this technique. The hydrothermal pathway will result in mesoporous carbon powders.

By selecting fast polymerizing resorcinol or phloroglucinol to react with formaldehyde under strongly acidic conditions, the second route, c.q. a macroscopic phase separation, can be observed [18,55,62]. Dai et al. performed a synthesis with resorcinol and F127 in ethanol and HCl solution. After a while the mixture turned cloudy and different phases began to separate and clearly formed two layers. The upper layer, consisting mostly of water and ethanol, was discarded. The lower layer was polymer-rich, containing both oligomers and F127. After aging, curing and carbonization, ultra-stable mesoporous carbons with a narrow pore size distribution around 4.9 nm, specific surface area of 418 m²/g and pore volume 0.35 cm³/g were obtained. Via this technique carbon monoliths are formed, these can be used as such or pulverized to the preferred particle size.

The evaporation induced self-assembly (EISA) is, nowadays, the more favored reaction pathway. The EISA of block copolymer and resols has been demonstrated as one of the most efficient pathways because it is applicable under wide synthetic conditions, such as acidity of the reaction solution, surfactant and p/s ratio [32,36,63–65]. The evaporation of the solvent can simply be performed in a petri dish or via the spin-coating or dip-coating technique. Different solvents such as THF, methanol, acetone or ethanol can be used. By evaporating the solvent, the polymer concentration is enriched, promoting the organic-organic self-assembly between the block copolymer and the resol which is controlled by hydrogen bonding interaction. Mesoporous carbons, prepared via the EISA method, can have a surface area of 714 m²/g, pore volume of 0.55 cm³/g and uniform 2D hexagonal pores of 5.0 nm [59]. Via the EISA procedure thin mesoporous films can be created via spin-coating or dip-coating.

All three pathways lead to the successful synthesis of mesoporous carbons, EISA and phase separation technique seem to have an advantage because of shorter reaction time and no need for precise pH control. The macroscopic morphology can range from powders, films to monoliths and is mostly affected by the choice in synthesis pathway [55].

1.3.6 Carbonization temperature

In the last step of the mesoporous carbon synthesis, the cured resins undergo a temperature treatment in an inert atmosphere (N_2 , Ar). In this step, two crucial processes take place. Firstly the surfactant is removed. The block copolymers consist of ether functionalities which are unstable at temperatures above $350^\circ C$. As they decompose and desorb from the material, they create porosity. Micropores are created where hydrophilic chains were present and ordered mesopores where the hydrophobic micelle cores were. The resulting pore structure is determined by the ordering of the micelles, which can be varied by selecting the precursor to surfactant ratio as described earlier.

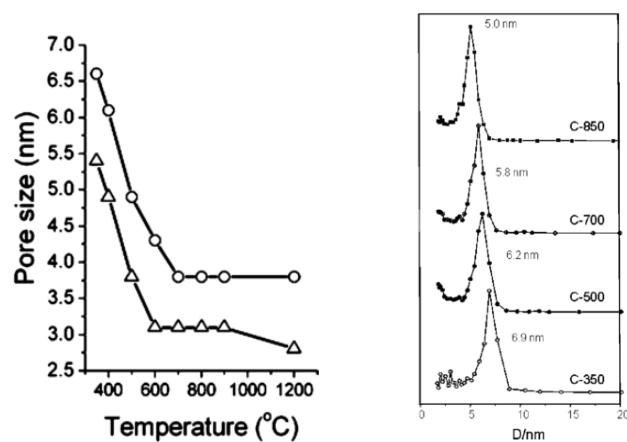


FIGURE 1.12: Effect of carbonization temperature on the pore size of FDU-16 (circles) and FDU-15 (triangles) (left) [7] and the PSD of mesoporous carbons synthesized with R/f/glutamic acid (right) [59].

As the carbonization temperature rises to $400^\circ C$ and higher some mesoporous carbons have encountered significant shrinkage or even collapse [22, 37, 65–67]. The pore size becomes smaller or the porosity is lost. At $400^\circ C$ the material is described as mesoporous polymer or resin, at temperatures above $600^\circ C$ the term mesoporous carbons applies. The pore size of mesoporous

carbon from F108/RF composite shifted from 6.3 to 4.9 nm by increasing the carbonization temperature from 400 °C to 700 °C. Most FDU-materials synthesized by Zhao et al. also show this shrinkage at higher carbonization temperatures, e.g. the pore size of FDU-15 changed from 5.4 to 2.8 nm between 350 °C and 1200 °C as seen in Figure 1.12 or via TEM images in Figure 1.13. [7]. For the R/f glutamic acid mesoporous carbons the pore size shifts from 6.9 nm to 5.0 nm by increasing from 350 °C to 850 °C. Not only morphological changes can be induced by these high carbonization temperatures, the mesoporous carbon enriches in carbon by removal of the remaining oxygen containing functional groups by heating in inert atmospheres [7, 43]. Changing the surface chemistry of the mesoporous carbon changes its point of zero charge (pH_{PZC}), more oxygen-containing groups will increase the pH_{PZC} or acidity, while introducing nitrogen functional groups will decrease the pH_{PZC} or increase the basicity [68]. Most mesoporous resins or polymers contain 70-85 wt% carbon, [40, 61, 69] while most pristine carbons that have been carbonized at 800 °C or higher, have a wt% C of 90 % or higher [37, 40, 61, 69, 70]. The last step of the mesoporous carbon synthesis has the ability to alter two important material characteristics. The hydrophobicity increases by using carbonization temperatures above 400 °C, and some mesoporous carbons are also affected by shrinkage of several nm in pore size as the temperature increases from 400 °C up to 800 °C.

1.3.7 Surface modification

The large variety of applications in separation, catalysis and electronics [39, 71–78] often requires surface modifications, which will introduce hetero-atoms (e.g. N, O, and F) or metallic functionalities to the mesoporous carbon. The chemical modification of the carbon surface is rather difficult due to the low reactivity of the carbon surface. The high carbonization temperatures remove most functional groups or weak C-X bonds [63]. Therefore a post treatment method is needed to introduce new functionalities and modify the carbon surface. Another possibility is the incorporation of a larger amount of hetero-atoms from the start of the synthesis. This can be achieved by using precursors with a high content of the hetero-atoms so that the functionalities are introduced ‘in-situ’ during the polymerization step. For adsorption, hetero-atom modifications can have a beneficial effect when electrostatic interactions are beneficial for the adsorption. Incorporation of metals in adsorption application is often limited to magnetizing the mesoporous carbon with Fe or Ni for easy separation [79, 80] and are not furthered discussed.

N-doping was achieved by treating carbons with an ammonia flow under high temperature. NH_3 is able to replace oxygen containing functionalities with N-containing groups and etching of carbon by radical formation gener-

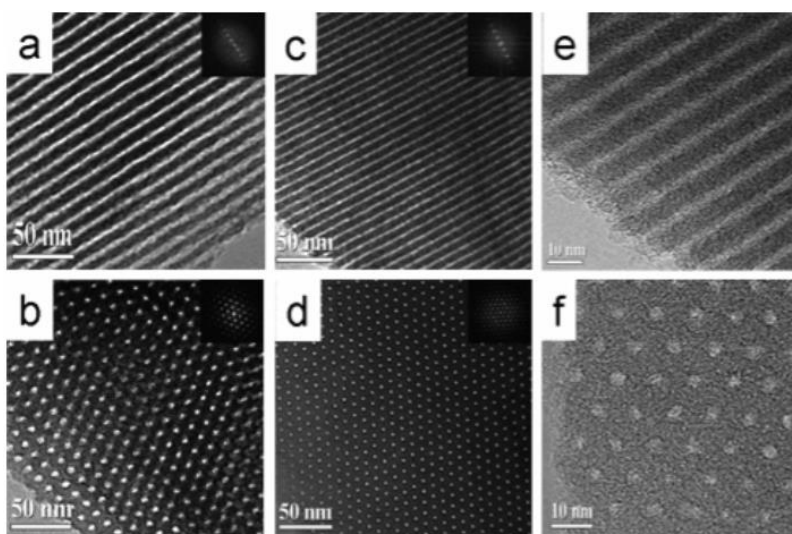


FIGURE 1.13: TEM images (a-d) and HRTEM images (e, f) of mesoporous materials FDU-15 prepared by using F127 as a template via the EISA method after calcination at 350 °C (FDU-15-350; a, b) and at 1200 °C (FDU-15-1200; c-f) under an Ar atmosphere, viewed from the [110] (a, c, e) and [001] (b, d, f) directions [7].

ated by NH_3 decomposition at high temperatures [81,82]. The active N-doped sites are embedded in the stable carbon framework and can be used as electrocatalysts or CO_2 adsorbents [83,84]. By altering or adding new precursor types, Schüth et al. were able to perform an in-situ N-doping in which 1,6-diaminohexane was added to the resorcinol/formaldehyde F127 mixture which led to a N-containing framework [58]. The doping of mesoporous carbons with nitrogen functionalities on their surface as seen in Figure 1.14, will increase their adsorption ability for acidic or anionic species [34, 36]. Other hetero atoms can be introduced in the same way. In-situ fluorinated carbons were synthesized by mixing a fluorinated precursor p-fluorophenol with phenol and formaldehyde to obtain a well dispersed C-F covalent bond functionalization which resisted temperatures of 900 °C. The incorporation of fluorine could be of value for electrocatalytic reactions [85]. To incorporate oxygen functionalities, surface oxidation can be performed with acids, H_2O_2 or ozone via post-modification. This technique introduces primarily carboxylic acids, esters or quinones [12, 41, 86]. This affects the hydrophobicity of the surface, decreasing the wt% C by increasing the wt% O in the mesoporous carbon. This acidification of the surface (Figure 1.14) lowers the pH_{PZC} of the carbon surface and can be important for the adsorption of cationic adsorbates [86].

Sometimes these oxidation steps can be detrimental for the material properties of the porous carbons [86]. Tanaka et al. compared HNO_3 oxidation with the milder ammonium persulfate (APS) oxidation, both methods preserved the ordered structure with some loss in specific surface area and pore volume. APS was able to introduce more oxygen functional groups than HNO_3 . The oxidized mesoporous carbons improved the overall capacitive performance of the supercapacitor and could be useful in a broad range of applications which request long cycle life and high power and energy densities [47]. These multitude of modifications with specific applications show the value and diversity of mesoporous carbons. However, pristine mesoporous carbons can already be utilized as a new interesting family of adsorbents.

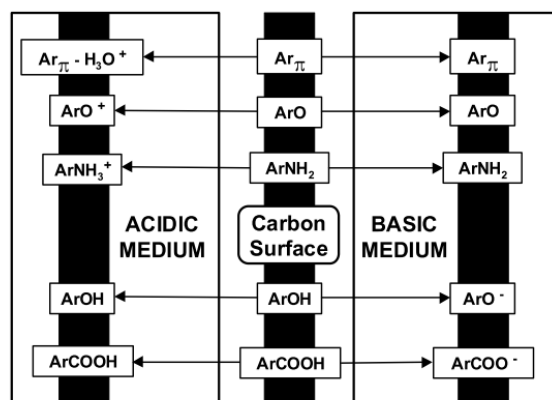


FIGURE 1.14: pH-effect on functionalities of carbon adsorbents in aqueous solutions [87].

1.4 Adsorption of organic pollutants

Adsorption has proven to be an effective technology for the removal of pollutants from water, in which the key factor is the exploitation of economical and efficient adsorbents. Mesoporous carbons are especially suited for the adsorption of organic compounds as these adsorbents are mainly hydrophobic, which increases the affinity towards organic pollutants [21, 88]. These pollutants have a variety of sources ranging from industrial, pharmaceutical to agricultural. The unique physical and chemical properties of mesoporous carbons such as large specific surface area, large pore volume, pore size control and tuning of the hydrophobicity are advantageous in adsorption applications. The presence of mesopores (2-50 nm) is crucial in the adsorption process of various larger organic molecules such as organic dyes, pharmaceuticals, en-

zymes, humic acids, etc. It can increase the maximum adsorption capacity as well as improve the adsorption kinetics.

Most adsorption studies of organic pollutants have been performed on activated carbon [89–91] and hard templated mesoporous carbons which were discovered in 1990 by Ryoo et al. [8,79,92–95]. As explained in Section 1.3, the recent development in soft templated mesoporous carbons allows a faster and more efficient synthesis pathway of mesoporous carbons with good control over pore size and pore geometry. However, only few soft templated mesoporous carbons have been tested as adsorbents for organic pollutants. Therefore, the performance of soft templated mesoporous carbons is compared with the more studied hard templated carbons. Important textural properties can be specific surface area, pore volume or pore size distribution and geometry. The adsorption ability also depends on the adsorbate properties, e.g. size, geometry, polarity and functional groups. A selection of adsorbate examples was chosen with varying properties. Their size, weight and structure are shown in Figure 1.15. Another factor influencing the adsorption is the pH of the solution. The adsorption of organic compounds from aqueous solution is the result of a complex interplay between electrostatic and non-electrostatic interactions. These interactions depend on the characteristics of the adsorbent and adsorbate. Electrostatic interactions appear at conditions in which they are ionized. Non-electrostatic interactions occur due to hydrophobic interaction [87].

BPA is a widely used compound in the production of polycarbonate plastics industry. It is classified as an endocrine disrupting chemical, putting human health and its reproductive system at risk, which makes the efficient removal of BPA a priority [96,97]. BPA is the smallest adsorbate molecule mentioned in Figure 1.15. With its molecular dimensions of $1.07 \text{ nm} \times 0.59 \text{ nm} \times 0.38 \text{ nm}$, it can adsorb in micropores as well as in mesopores. This results in both successful adsorption with AC [98,99] and hard templated mesoporous carbons (Table 1.2). Adsorption capacities were almost unchanged in an initial pH range of 3 to 9, but decreased dramatically from pH 9 to 13, due to the deprotonation of BPA [100]. The electrostatic repulsion between the bisphenolate ion and the negatively charged carbon surface formed at high pH values lowers the adsorption capacity [100].

The effect of material characteristics on BPA adsorption was also investigated for activated carbon (AC) and hard templated (CMK-3). When studying adsorption kinetics, the disordered geometry and small pores of AC resulted in the slowest adsorption [100]. The introduction of larger ordered pores of 4.9 nm in CMK-3, enhanced the adsorption rate of BPA. Comparing the open geometry of the interconnected nanorods in CMK-3 with the disordered micropores of AC, the CMK-3 resulted in faster adsorption kinetics [100] as seen in Figure 1.16.

1.4. Adsorption of organic pollutants

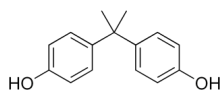
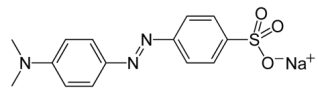
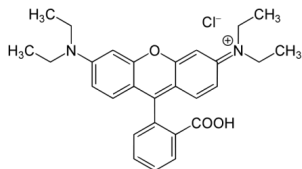
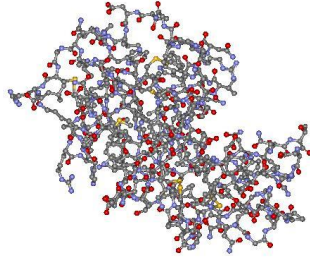
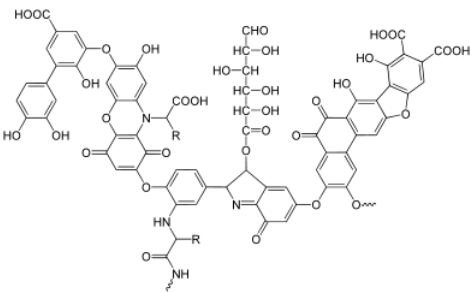
Adsorbates	Molecular dimensions (nm)	MW (g/mol)	Structure
Bisphenol A	1.07×0.59×0.38	228.29	
Methyl orange	1.31×0.55×0.18	327.33	
Rhodamine B	1.59×1.18×0.56	479.02	
Lysozyme	RH* = 2.05	14400	
Humic acid	RH* = 2.2-7.1	500-150000	

FIGURE 1.15: Properties of organic adsorbates with different MW and size or RH = hydrodynamic radius.

Table 1.2: Material characteristics of various carbon adsorbents and their adsorption capacity for BPA. * All adsorption experiments were performed at pH 7.

Material	Type	S_{BET} (m^2/g)	V_{tot} (cm^3/g)	D_p nm	q_{max,BPA^*} mg/g	
AC-PCB	AC	916	0.58	<3.0	263	[98]
CMK-3	HT	921	1.31	4.9	296	[100]

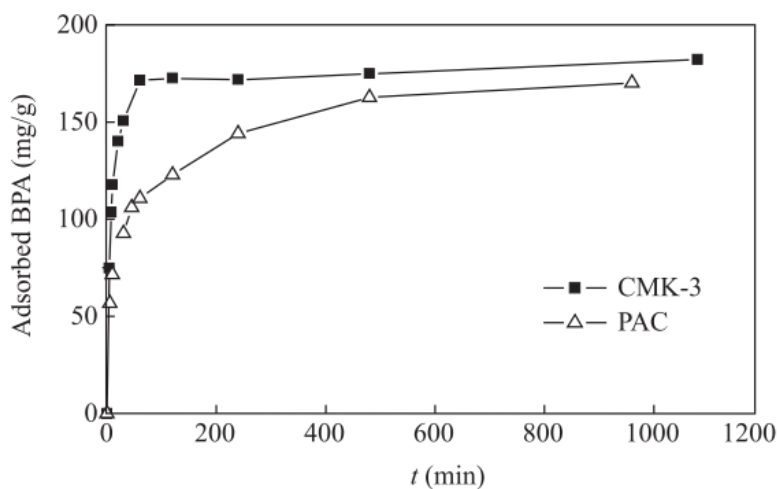


FIGURE 1.16: Adsorption kinetics of 10 mg of CMK-3 (■) and PAC (▲) in 100 mL of 25 mg/L BPA-solution [100].

A second important group of pollutants are the organic dyes, these industrial pollutants may induce mutagenic activity or pose negative effects on aquatic life via obstructing light penetration or oxygen transfer in water bodies. Their removal has been successful to some extent using commercial activated carbons [101]. However larger organic dyes e.g. methyl orange (MO) or rhodamine B (RhB), were more efficiently removed using mesoporous carbons [79, 102, 103].

Dong et al. used hard templated carbon materials (C-1@Fe) to remove both MO and RhB with magnetic Fe particles for easy separation, see Table 1.3. The adsorption capacity of both dyes was improved by increasing

the specific surface area [79]. Zhang et al also reported positive correlations between the specific surface area and adsorption capacities of dyes [79]. Therefore, increasing the specific surface of soft templated mesoporous carbon was investigated. By adding TEOS together with the phenolic resin precursor, silica parts were embedded in the mesoporous carbon framework creating a carbon and silica hybrid material. Removing the silica in a later stage created extremely high surface areas as seen in Table 1.3. The difference between MPC and MPSC/C is this addition of TEOS to the soft template route. The increase in specific surface area resulted in a large RhB adsorption capacity increase from 215 mg/g to 785 mg/g. Teng et al. discovered that by increasing the amount of TEOS, mesoporous carbons were obtained with increasing specific surface areas, pore volumes and pore sizes ranging from 2.1 to 4.6 nm. The adsorption capacity for MO could be increased from 329 mg/g to 558 mg/g [102].

Table 1.3: Material characteristics of various carbon adsorbents and their adsorption capacity (q_{max}) for organic dyes (MO = methyl orange, RhB = rhodamine B). * All adsorption experiments were performed at pH 7.

Material	Type	S_{BET} (m ² /g)	V_p (cm ³ /g)	D_p (nm)	$q_{max,MO}^*$ (mg/g)	$q_{max,MO}^*$ (mg/g)	
C-1@Fe	HT	975	1.08	4.1	422	342	[79]
C3	ST + TEOS	1642	1.02	4.3	558		[102]
MPC	ST	757	0.55	4.5		215	[103]
MPSC/C	ST + TEOS	2580	2.16	6.4	637	785	[103]

Another important factor influencing adsorption is the structural matching between adsorbate and adsorbent, Zhang et al. called this the spatial effect [103]. They investigated dyes of varying size and observed that the pore occupation of small size dye molecules was higher in the carbon with smaller pore size. For larger dyes, pore blockage was observed in the micropores and small mesopores, strongly decreasing the adsorption capacity for the largest dye molecule. The larger pore MPSC/C showed a high pore occupation for large pollutants as seen from the adsorption capacity of MO and Rb in Table 1.3 [103]. The control in mesoporous size is important to obtain a high pore occupation and adsorption capacity.

While the textural properties of the mesoporous carbon is the most important factor, the surface chemistry will also have an effect on adsorption capacity. The mesoporous carbon adsorbent in this study had a pH_{PZC} of 4. When the pH of solution exceeds pH_{PZC} , the adsorbent surface is nega-

tively charged, favoring the adsorption of cationic species; while for a solution pH below pH_{PZC} , the surface is positively charged, favoring adsorption of anionic species [104]. MO is an anionic dye which will undergo electrostatic repulsion forces with the negatively charged species of the carbon surface at high pH values. Varying the pH from 2 to 9 indeed lowered the adsorption capacity from 560 mg/g to 479 mg/g [102]. For RhB, a cationic dye which is positively charged at high pH values, the RhB adsorption capacity of mesoporous carbons increased above a pH of 4, which is explained by the electrostatic attractions [102]. The adsorption of dyes on mesoporous carbons is generally described by pseudo second order kinetics and is reported to occur rapidly [19–22]. A comparative study between activated carbon and mesoporous carbons could further elucidate the difference in adsorption rates on carbon materials with varying pore sizes.

Adsorption of very large organic molecules is an important issue because of the inability of activated carbon to sufficiently remove these large molecules. The small micropores are simply too small to capture and remove very large adsorbate molecules e.g.: lysozyme (Lz) and humic acid with a hydrodynamic radius of respectively 2.05 nm or 2.2 to 7.1 nm [23, 25]. Enzyme adsorption has attracted attention due to its importance and application in medical and food industries for the use as enzymatic catalyst, biosensor or disease diagnostic [8, 21]. Vinu et al. synthesized large pore cage type hard templated mesoporous carbons to adsorb lysozyme (Lz) as seen in Table 1.4. They polymerized sucrose in silica KIT-5 and compared the adsorption capacity to the more known CMK-3 carbon derived from SBA-15. The CMK-3-100 with pore size of only 3.0 nm had a very low lysozyme adsorption capacity of around 141 mg/g. The maximum adsorption of the cage type carbon (CMK-3-150) with larger pore size and volume was 343 mg/g. The increase in pore size and pore volume doubled the Lz adsorption. The lysozyme adsorption was also performed at different pH values. The adsorption capacity decreased at pH lower and higher than 11. At pH 11, the isoelectric point of Lz is reached and it will have a zero net charge, so the hydrophobic interaction with the carbon surface can be optimal [105]. The advancement in soft templated mesoporous carbons allows the synthesis of large mesoporous carbons with the help of new surfactants as seen in Table 1.1. The use of a PEO-PBO-PEO surfactant (C-V-50-T-50-600, Table 1.4) gave pores of 27 nm and an Lz adsorption capacity of 446 mg/g [25]. It is clear that for large molecules the specific surface area is no longer the most important material characteristic influencing the adsorption. Pore size and pore volume become more important as the adsorbate size increases. With the new developments in soft templated mesoporous carbon these can be fine-tuned to the specific needs of the adsorbate.

One of the largest organic pollutants is humic acid (HA). HA is particularly detrimental in drinking water production, as it reacts with the disinfectant

Table 1.4: Material characteristics of various carbon adsorbents and their adsorption capacity for Lysozyme. * All adsorption experiments were performed at pH 11.

Material	Type	S_{BET} (m ² /g)	V_{tot} (cm ³ /g)	D_p nm	$q_{max,Lz}^*$ mg/g	
CMK-3-100	HT	1260	1.10	3.0	141	[106]
CMK-3-150	HT	1350	1.60	5.4	343	[106]
C-V-50-T-50-600	ST	810	1.33	27.0	446	[25]

Cl₂ to form carcinogenic byproducts [107, 108]. As removal with microporous activated carbon was unsuccessful, mesoporous carbons are of great interest. Post treatment of activated carbon to introduce mesoporosity [109] allowed to increase the adsorption of humic acid, see Table 1.5. A hard templated mesoporous carbon CMK-3 with pore size of 3.7 nm (Table Table 1.5) was used for HA adsorption with a maximum capacity of 137 mg/g [24]. Humic acid consists of different biopolymers with various MW and size. The mesoporous CMK-3 was able to adsorb the large HA molecules while AC was not able to do so [24].

Table 1.5: Material characteristics of various carbon adsorbents and their adsorption capacity for humic acid. * All adsorption experiments were performed at pH 11.

Material	Type	S_{BET} (m ² /g)	V_{tot} (cm ³ /g)	D_p nm	$q_{max,HA}^*$ mg/g	
AC/H	Mod. AC	452	0.510	0-50	140	[109]
OMC (CMK-3)	HT	988	1.33	3.7	137	[93]

At low pH, HA is neutral and less electrostatic repulsions occur simultaneously with more hydrophobic interactions between adsorbate and adsorbent which enhances HA adsorption [24]. Increasing the pH makes HA negatively charged which causes electrostatic repulsion with the negative charges on the carbon surface and, hence, decreases the adsorption [110–112]. The investigation of HA adsorption on soft templated mesoporous carbons has not yet been reported, therefore in chapter 3 we investigate how soft templated mesoporous carbon perform as a possible adsorbent as well as investigate the effect of material characteristics on the adsorption of HA.

1.5 Conclusions

Soft templated mesoporous carbons are versatile, highly tunable materials. Changing different synthesis parameters such as type of precursor, surfactant, the p/s ratio, an acid or base catalyst, the synthesis pathway or the final carbonization temperature, has a significant effect on the resulting material properties. The reactivity of the most frequently used precursors increases from phenol to resorcinol to phloroglucinol, which allows faster reaction times but can lead to less ordered materials. Also greener alternative biopolymer type precursors are an emerging class of carbons precursors. Functionalities can be incorporated by selecting the right carbon precursor, e.g. addition of N-containing precursors facilitates the synthesis of N-doped mesoporous carbons.

Surfactant choice is still dominated by the effective pluronics: F108, P123 and F127. These amphiphilic block copolymers provide carbon materials with a homogeneous pore structure and a pore size between 2 and 10 nm depending on the surfactant type and the p/s ratio. To create larger pores, new type of surfactants have been investigated: PEO-PMMA, PEO-PS, PS-P4VP, PEO-PCL and PEO-PBO-PEO. Larger hydrophobic parts lead to larger micelle cores and therefore larger pore sizes up to 30 nm. New types of surfactants could further advance the production of large pore mesoporous carbons. Addition of swelling agents or pore expanders increases the pore size with some extra nanometers.

When changing the p/s ratio, the symmetry of the mesophase can be changed. At lower p/s ratios, the interfacial curvature changes and 2D hexagonal pores shift to a 3D cubic structure, cage-like structure or a 3D open pore network. In some cases the lower p/s ratio was also responsible for an increase in pore size up to 50 nm, this is often accompanied with a broadening of the pore size distribution. More studies towards specific reaction conditions for creating larger pore systems with traditional surfactants could still be discovered.

The macroscopic morphology can range from powders, films to monoliths and is mostly affected by the synthesis pathway. EISA and phase separation pathways are preferred for their shorter reaction time and no need for precise pH control.

Lastly the carbonization temperature increases the hydrophobicity of the carbon material by removing oxygen containing functionalities at higher temperatures, this however can induce shrinkage, and can narrow the pore size with several nm in mesoporous carbons. The further development in surfactants and specific reaction conditions of soft templated mesoporous carbons will allow tunability of large mesopores and macropores. The creation of

materials with micro-, meso- and macropores could lead to new interesting adsorbents capable of adsorbing a variety of pollutants.

Mesoporous carbons have exceptional material properties for use as an adsorbent for organic pollutants. The presence of mesopores allows the adsorption of larger adsorbates and often improves the adsorption rate in comparison to the small disordered microporous activated carbon. Industrial, agricultural and pharmaceutical components have been adsorbed onto mesoporous carbons. Most studies up to date, use hard templated mesoporous carbons as an adsorbent. The more recently developed and more efficient synthesis of soft templated mesoporous carbons could lead to new interesting adsorption applications, because of the tunability of the pores and pore size distribution.

When adsorbing large dye molecules, the specific surface area of the carbon is positively correlated with the adsorption capacity. Mixing the concept of both hard and soft template synthesis steps, and addition of TEOS to the soft template synthesis, created a mesoporous carbon which has a significantly higher specific surface area, leading to increased dye adsorption. The spatial effect or structural matching between the adsorbate and adsorbent pore size is a second important factor in the adsorption process.

When the adsorbates become extremely large for example, humic acid or Lysozyme, very large pore sizes will be required which can easily be obtained via soft templating techniques. The adsorption capacity of very large pollutants is often no longer correlated with the specific surface area but more with the pore size and volume of the mesoporous carbon. Adsorption capacities for large pollutants increase with larger pore sizes and volumes. The adsorption of organic compounds is also an interplay between electrostatic and non-electrostatic interactions which depend on the charges of both the adsorbent and adsorbate at different pH values.

Future work in the synthesis of soft templated mesoporous carbons could reveal new insights. Within the soft template method, the use of new surfactant types or different p/s ratios under specific synthesis conditions are delivering new large pore mesoporous carbons. A carbon material with porosity ranging from micro- to meso- and even macropores could allow the adsorption of a whole range of pollutants and ensure good accessibility to the different adsorption sites. The largest pores will create the possibility to adsorb even the largest pollutants or biomolecules, while the smaller pores can adsorb the smaller pollutants. Their tunability towards pore size, specific surface area, pore volume and surface chemistry provides a toolbox for the synthesis of a new generation of adsorbents for large organic pollutants.

Ordered mesoporous materials (e.g. carbons or boron nitride) require advanced characterization techniques to investigate their material properties: morphology, specific surface area, pore volume, pore size distribution or elemental composition. The techniques used in this work to determine these material properties are described below.

2.1 Nitrogen sorption

Important characteristics of an adsorbent are the specific surface area, pore volume and pore size distribution. A vital technique to determine these material characteristics is nitrogen sorption. This physical adsorption technique consists of exposing a porous solid to an inert gas. As a gas molecule randomly encounters the solid, the molecule is attracted to the surface and is adsorbed on the surface. As the gas pressure increases, the number of molecules hitting and sticking on the surface increases. In other words, the number of molecules adsorbed increase as a function of the pressure. At incremental gas pressures, the amount of adsorbed molecules is measured after equilibrium is reached, this process continues until atmospheric pressure is reached. Next, the same process is followed for decreasing gas pressures. The quantity of molecules adsorbed or desorbed as a function of the relative pressure is plotted as the adsorption and desorption isotherm respectively. [113].

There are 6 types of isotherms that are identified by IUPAC [114]. Only type I and type IV are observed in this work, see Figure 2.1. Reversible Type I isotherms are observed for microporous solids having relatively small external surfaces, e.g. some activated carbons, molecular sieve zeolites and certain porous oxides. A Type I isotherm is concave to the p/p_0 axis and the amount

2. CHARACTERIZATION OF POROUS MATERIALS

adsorbed approaches a limit value. This limited uptake is governed by the accessible micropore volume rather than by the internal surface area. A steep uptake at very low p/p_0 is due to enhanced adsorbent-adsorptive interactions in narrow micropores (micropores of molecular dimensions), resulting in micropore filling at very low p/p_0 . For nitrogen adsorption at 77 K, Type I(a) isotherms are observed in microporous materials having mainly narrow micropores (of width <1 nm); Type I(b) isotherms are observed with materials having pore size distributions over a broader range including wider micropores and possibly narrow mesopores (< 2.5 nm).

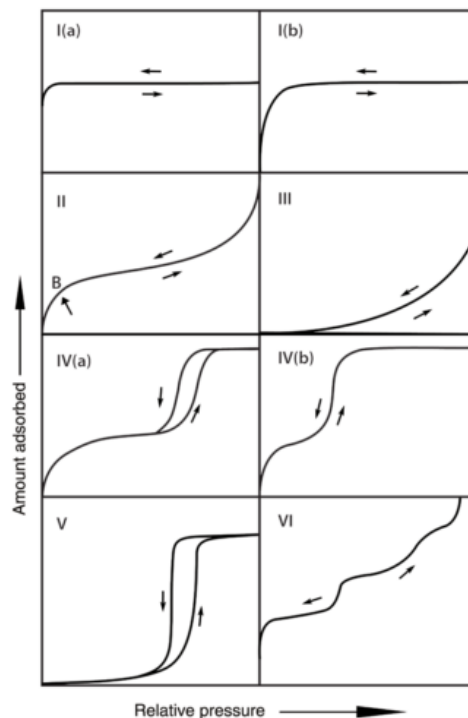


FIGURE 2.1: Different types of N_2 sorption isotherms identified by IUPAC [114].

Type IV isotherms are observed for mesoporous adsorbents such as many oxide gels, industrial adsorbents and mesoporous molecular sieves. The adsorption behaviour in mesopores is determined by the adsorbent-adsorptive interactions and also by the interactions between the molecules in the condensed state. In this case, the initial monolayer-multilayer adsorption on the mesopore walls, which takes the same path as the corresponding part of a Type II isotherm, is followed by pore condensation. Pore condensation is the

phenomenon whereby a gas condenses in a pore at a pressure p below the saturation pressure p_0 of the bulk liquid. A typical feature of Type IV isotherms is a final saturation plateau, of variable length. In the case of a Type IV(a) isotherm, capillary condensation is accompanied by hysteresis. This occurs when the pore width exceeds a certain critical width, which depends on the adsorption system and temperature (e.g., for nitrogen in cylindrical pores at 77 K, respectively, hysteresis starts to occur for pores wider than 4 nm). With adsorbents having mesopores of smaller width, completely reversible Type IV(b) isotherms are observed. In principle, Type IV(b) isotherms are also observed for materials with conical and cylindrical mesopores that are closed at the tapered end [114].

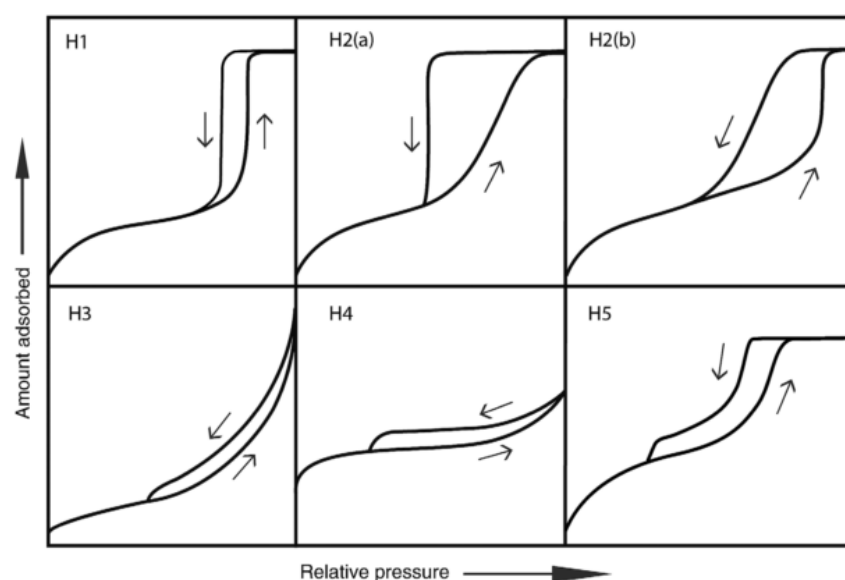


FIGURE 2.2: Different hysteresis types identified by IUPAC [114].

The different types of hysteresis provide additional information about the morphology of the pores, see Figure 2.2. The Type H1 loop is found in materials which exhibit a narrow range of uniform mesopores, as for instance in templated silicas (e.g., MCM-41, MCM-48, SBA-15) and ordered mesoporous carbons. Usually, network effects are minimal and the steep, narrow hysteresis is a clear sign of delayed condensation in the adsorption branch. The type H2 hysteresis is observed for more complex pore structures in which network effects are important. The very steep desorption branch, which is a characteristic feature of H2(a) loops, can be attributed either to pore-blocking/percolation in a narrow range of pore necks or to cavitation-induced evaporation. H2(a) loops are observed for ordered mesoporous materials (e.g.,

SBA-16 and KIT-5 silicas). The Type H2(b) loop is also associated with pore blocking, but the size distribution of neck widths is much larger than H2(a). There are two distinctive features of the Type H3 loop: (i) the adsorption branch resembles a Type II isotherm (ii) the lower limit of the desorption branch is normally located at the cavitation-induced p/p_0 . Loops of this type are observed for non-rigid aggregates of plate-like particles (e.g., certain clays) but also if the pore network consists of macropores which are not completely filled with condensate. The type H4 loop is somewhat similar, but the adsorption branch is now a composite of Types I and II, the more pronounced uptake at low p/p_0 is associated with the filling of micropores. Type H4 loops are often found with aggregated crystals of zeolites, some mesoporous zeolites, and micro-mesoporous carbons. Although the Type H5 loop is unusual, it has a distinctive form associated with certain pore structures containing both open and partially blocked mesopores (e.g., plugged hexagonal templated silicas). As already indicated, the common feature of H3, H4 and H5 loops is the sharp step-down of the desorption branch [114].

Figure 2.3 shows a typical nitrogen sorption isotherm of a mesoporous carbon with a type IV isotherm and H1 hysteresis. At low relative pressure, gas molecules begin to adsorb on the surface. With increasing pressure, a first adsorption layer starts to build up and micropores are being filled, observed between points A and B in Figure 2.3. As the relative pressure further increases, adsorption takes place in multilayers. This is reflected by the linear part of the isotherm between point B and C. Further increasing the pressure, mesopores are filled and capillary condensation occurs, observed by the steep increase of the isotherm between point C and D in Figure 2.3. Ultimately, the absolute pressure approaches the saturation pressure and adsorption is maximized, observed by the plateau between point D and E. Between point E and F, interparticle adsorption of gas molecules occurs.

The specific surface area is determined by the BET equation derived from the BET theory (Brunauer, Emmet and Teller). The BET equation in linear form is given in Equation 2.1 with (V_m) the volume adsorbed for one monolayer, (V_A) the volume adsorbed at pressure p , C the value for the strength of interaction between the gas molecule and the solid.

$$\frac{1}{V_A((p_0/p) - 1)} = \frac{C - 1}{V_m C} * \frac{p}{p_0} + \frac{1}{V_m C} \quad (2.1)$$

If $\frac{1}{V_A((p_0/p) - 1)}$ is plotted versus $\frac{p}{p_0}$, a linear relation is obtained, for the determination of the specific surface area it is crucial that the linear part of the plot is selected. The linear part is mostly found in the region with relative pressure range 0.05 to 0.30, but not always. The relevant parameters should

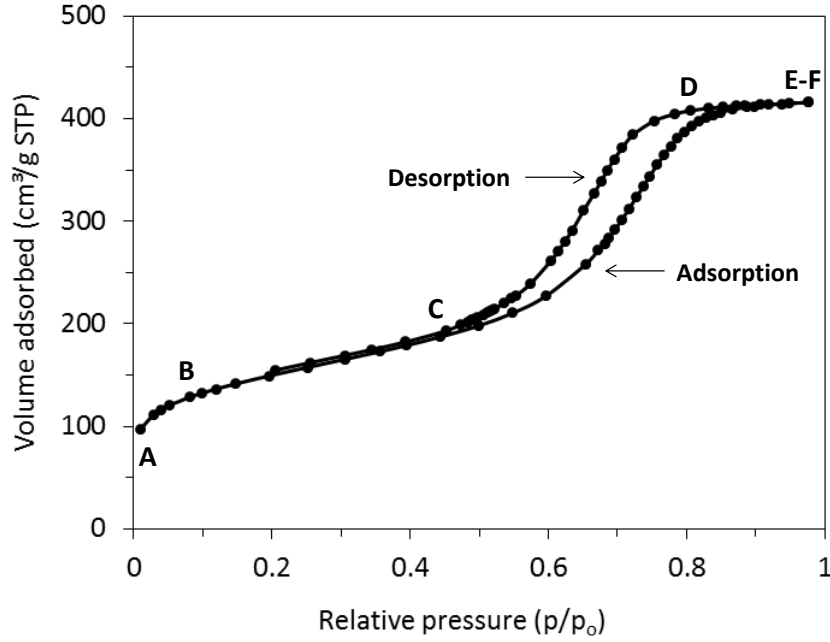


FIGURE 2.3: Different stages of a nitrogen sorption isotherm of a soft templated mesoporous carbon.

always be derived from the linear part. Then, the volume adsorbed for a monolayer (V_m) can be determined and the specific surface area is calculated using Equation 2.2 with N_A the number of Avogadro and A the mean cross sectional area of $N_2 = 0.162 \text{ nm}^2$.

$$S_{BET} = \frac{V_m}{22400} * A * N_A * 10^{-18} \quad (2.2)$$

The total pore volume is calculated at maximized adsorption at relative pressure of around 0.95 via Equation 2.3.

$$V_{tot} = \frac{V_A}{22400} * 34.6 \text{ cm}^3 \quad (2.3)$$

The pore size distribution (PSD) is calculated by the Barrett, Joyner, Halenda (BJH)-method which uses the Kelvin equation (Equation 2.4) to calculate the pore size. With r standing for the Kelvin pore size; γ , the surface tension; V_m ; R , the universal gas constant, and T , the temperature. All stated pore

sizes (D_p) refer to the mean mesopore size. The PSD of microporous activated carbon is determined via DFT using a carbon kernel.

$$\ln \frac{p}{p_0} = \frac{2\gamma V_m}{rRT} \quad (2.4)$$

All samples were measured on a Micromeritics Tristar 3000 or Tristar 2 equipment. Approximately 0.1g of sample is used and pretreated at 120 °C in vacuum.

2.2 Powder X-ray diffraction

When porous materials have ordering, this can be analyzed by means of X-ray diffraction (XRD). When an X-ray beam is scattered by the atoms of the material, interaction with the electrons occurs and the beam is re-radiated in all directions. This phenomenon is called elastic scattering. When a material has a particular ordering or symmetry, constructive interference occurs in a specific direction. This is determined by Bragg's law: $2d\sin\theta = n\lambda$, with d the spacing between diffracting planes, θ the incident angle of the beam, n an integer and λ the wavelength of the beam (Figure 2.5).

When large d -values are investigated, the angle θ needs to be very small. Therefore small angle X-ray diffraction (SAXS) is often required for the analysis of materials with large d values. The walls of mesoporous carbons are amorphous, so reflection in XRD is attributed to the repetitive structure of the pores on the mesoscale. Different pore geometries have been identified, e.g. lamellar, hexagonal or cubic structures. Powder X-ray diffraction (PXRD) patterns of the materials were collected on a Thermo Scientific ARL X'Tra diffractometer, operated at 40 kV, 40 mA using Cu $K\alpha$ radiation with 0.15418 nm wavelength.

2.3 Elemental analysis

With elemental analysis, the wt% of carbon, hydrogen, nitrogen and sulfur of a sample are determined. The analysis is done by burning the sample at 1800 °C in a oxygen rich environment. At this temperature the carbon in the sample is oxidized to CO_2 , hydrogen is oxidized to water, nitrogen will be oxidized to N_2 or NO_x and sulfur will be oxidized to SO_2 . An inert carrier gas (He) transports these reaction gases from the combustion chamber to the gas chromatograph while excess oxygen is removed with a copper catalyst. The gases are separated via gas chromatography and analyzed with a thermal conductivity detector. All samples were analyzed with a Flash 2000 organic element analyzer.

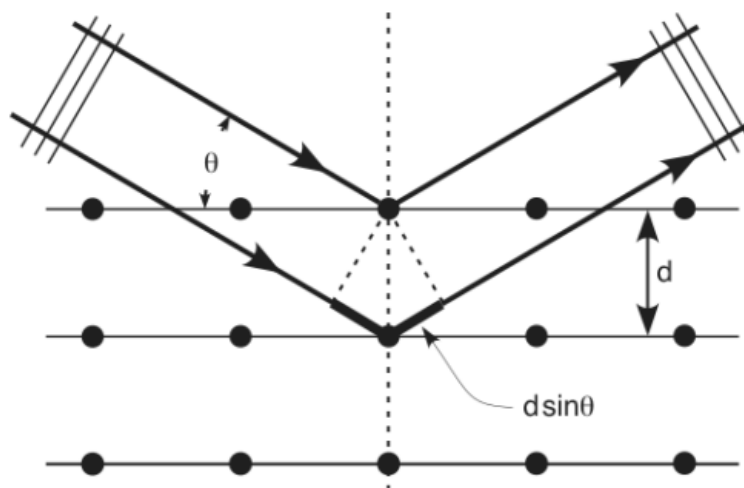


FIGURE 2.4: Schematic representation of Bragg's law.

2.4 DRIFTS

DRIFTS is a spectroscopic technique used to analyze chemical compositions and bonds within a molecule. When the frequency of a specific vibration is equal to the frequency of the IR radiation directed on the molecule, the molecule absorbs the radiation. As a result, different functional chemical groups absorb characteristic frequencies of IR radiation. Those that produce a net change in the dipole moment may result in an IR activity. The total number of observed absorption bands is generally different from the total number of fundamental vibrations. On the one hand, it is reduced because some vibrations are not IR active and on the other hand, additional bands are generated by the appearance of overtones or coupling interactions of two fundamental absorption frequencies. The major types of molecular vibrations are stretching and bending. Diffuse reflectance infrared Fourier transform spectroscopy (DRIFTS) is performed in vacuum at 120 °C on a hybrid IR-Raman spectrophotometer, the Nicolet 6700 (Thermo Scientific) with a liquid nitrogen cooled MCT-A detector, using a Graseby Specac diffuse reflectant cell.

2.5 Raman spectroscopy

Raman spectroscopy is a spectroscopic technique used to observe vibrational, rotational, and other low-frequency modes in a system. Raman spectroscopy is commonly used in chemistry to provide a fingerprint by which molecules can be identified. Scattered light itself can be distinguished between elastic and inelastic scattering. The major part scatters elastic which means that the energy (i.e. wavelength) of the incident light is equal to the emitted light. This phenomenon is referred to as Rayleigh scattering. Only a minor part scatters inelastically where a small fraction of energy is transferred between molecule and photon. It causes changes in the polarization of the molecule which are induced by molecular vibrations. Hence energy and wavelength of incident and scattered light are not equal anymore. The shift in energy gives information about the vibrational modes in the system. Raman analysis on the ammonia borane precursor was performed on a RXN1 Raman spectrometer (Kaiser Optical Systems) fitted with a 532 nm laser operating at 40 mW and using an optical probe.

2.6 Thermogravimetric analysis

TGA is used to determine material characteristics that exhibit either mass loss or gain at increasing temperatures due to decomposition, oxidation, or loss of volatiles. TGA analysis can be used to identify materials characterization through analysis of characteristic decomposition patterns and determine material stability in both nitrogen atmosphere or air, determination of organic content in a sample due to oxidation in air is possible as well as the determination of inorganic (e.g. ash) content in a sample, which may be useful for examining material composition. TGA measurements were performed on a STA 449 F3 Jupiter (Netzsch) in which 10 mg sample was loaded and heated at 10 °C/min in a nitrogen or air atmosphere.

2.7 UV-Vis spectroscopy

Ultraviolet–visible spectroscopy or ultraviolet-visible spectrophotometry (UV-Vis) refers to absorption spectroscopy or reflectance spectroscopy in the ultraviolet-visible spectral region. This means that certain molecules adsorb light in the visible or adjacent near-UV range. In this region of the electromagnetic spectrum, atoms and molecules undergo electronic transitions. The difference in intensity of the incident light beam (I_0) and the transmitted beam (I_t) is correlated to the concentration of organic compound in solution. Bisphenol A and humic acid concentration were determined by constructing a calibration curve at respectively 275 nm and 254 nm by a Thermo scientific Evolution 60 UV/VIS spectrophotometer.

2.8 LC-OCD

Liquid chromatography - organic carbon detection (LC-OCD) is a technique to determine the MW distribution of organic compounds in a solution. The liquid enters the UV-detector (UVD) and then the Organic Carbon Detector (OCD). A side stream after UVD enters a special capillary UV-lamp (DONOX) and then a 2nd UV-Detector measuring at 220nm. Here, Dissolved Organic Nitrogen (DON) and ammonium is determined after conversion to nitrate in the DONOX reactor. The "heart" of the LC-OCD system is the OC-Detector (OCD). The main components of the OCD are the so-called Graentzel Thin-Film Reactor and non-dispersive IR-Detector.

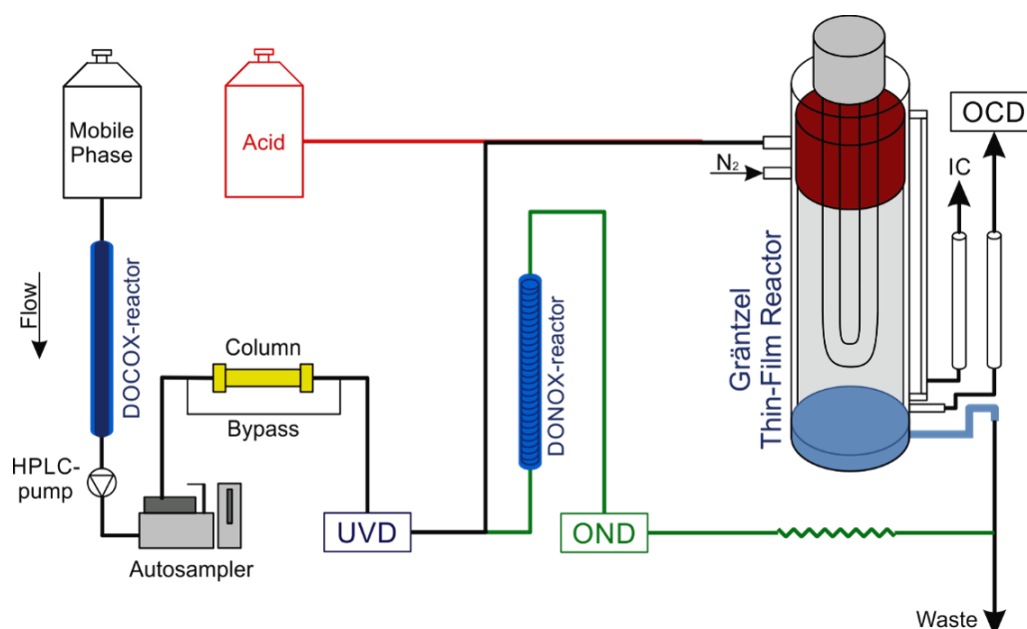


FIGURE 2.5: Schematic representation of LC-OCD setup [115].

The Graentzel thin-film reactor works as following: Carrier N_2 gas enters the reactor in the upper third of the reactor. The gas is split, about two third is flowing upwards and picks up inorganic carbon dioxide, i.e. carbon dioxide released from carbonic salts upon acidification. This gas is released through an outlet hidden behind the reactor. The other one third of the carrier gas flows downwards and picks up the organic carbon dioxide, i.e. the carbon dioxide released upon oxidation. This gas leaves the reactor at an outlet found at the lower end of the reactor (Organic Carbon Flow, OC).

The mobile phase solution and the acidification solution enter the reactor at the upper end where they become mixed by means of Teflon pins placed inside a rotating quartz cylinder. The upper third of the reactor is UV-shielded and the counter-current IC flow strips all carbon dioxide which was either already present, or was formed by acidification from carbonate salts, hence all inorganic carbon. The residence time of the solution in this area is about 20 seconds. The solution continues its way down the inner side of the reactor mantle (gravity-driven) and enters the UV-exposed area where the carrier gas in co-flow direction downwards picks up carbon dioxide released by oxidation (hence organic carbon, OC). The exact position of the gas inlet is such that in a small area the co-flow direction is within the UV-shielded area to prevent a breakthrough of IC into the OC flow. This carbon dioxide is quantified in the IR cuvette. The residence time in the UV-exposed area is about 60 sec. The thinness of the liquid film and the active stirring by the Teflon pins guarantees a rapid oxidation and stripping process. This is the unique feature of the Graentzel reactor, that both reactions are performed quantitatively and in relatively short time. This is necessary to be able to use the system as a chromatographic detector. Another very important feature is that the reactor operates with constant pressure, temperature and volume. No valves are used. This means that the residence time of the measuring gas in the IR cuvette is extremely stable. This allows high-sensitivity analysis even in the sub-ppb-range [115].

2.9 Zeta potential measurements

Zeta potential of AC and SMC materials were determined using a Zetasizer Nano. About 10 mg of adsorbent was added to 50 mL distilled water and then sonicated for 30 min and was placed in a plastic cell between a positive and a negative electrode. An electric field was applied across the electrophoresis cell, causing the particles to move towards the electrodes with a velocity proportional to the ZP and in a direction determined by the sign of their charge. The pH of the solutions was recorded shortly before measuring the ZP of the adsorbent samples. The ZP as a function of pH of the solution was determined, by adjusting the pH with 0.1M HCl or NaOH.

2.10 TEM and SEM

TEM and SEM images are used to visualize the particle size on micrometer scale and investigate the pore structure on nanometer scale. A typical TEM image of a 2D hexagonal mesoporous carbon is shown in Figure 2.6. TEM-images were taken on a JEOL JEM 2200-FS TEM and SEM-images were

taken on an JEOL JSM 7600F FEG SEM.

In a TEM, electrons are directly transmitted through an ultra-thin specimen are detected. In most cases, an electron beam is generated either by thermal emission (using a tungsten filament or a LaB₆- crystal) or by thermally assisted field emission (Schottky field emitter) producing a beam of electrons whose wavelength depends on the acceleration voltage (usually between 80 and 400 kV). A complex lens system is needed for the illumination and the imaging process. The lens systems can be subdivided in three main components. With the condenser lens system various illumination conditions can be chosen. In normal TEM mode, a rather parallel illumination of an area whose size depends on the actual magnification usually is required. Within the sample the intensity of the electron beam is modulated by interaction of the electrons with the specimen atoms. Behind the specimen the objective lens focuses the modulated electron beam again and creates the first magnified image of the sample. Finally the projector lenses further magnify the image and project it on a fluorescent screen or a CCD camera.

Scanning electron microscope (SEM) images are recorded by scanning the sample surface with a high-energy electron beam in a raster scan pattern. In a SEM, the electron beam is also generated by an electron gun (tungsten filament, LaB₆-crystal, field emission gun) but with much smaller accelerating voltages of 0.1 – 30 kV compared to TEM. Unlike TEM, the most common signal used in SEM are secondary electrons generated by the incident electrons, for imaging the surface of a specimen. Due to the imaging of the sample surface in SEM, the requirements for the specimens are not as strict as for TEM samples and the preparation is less extensive [74].

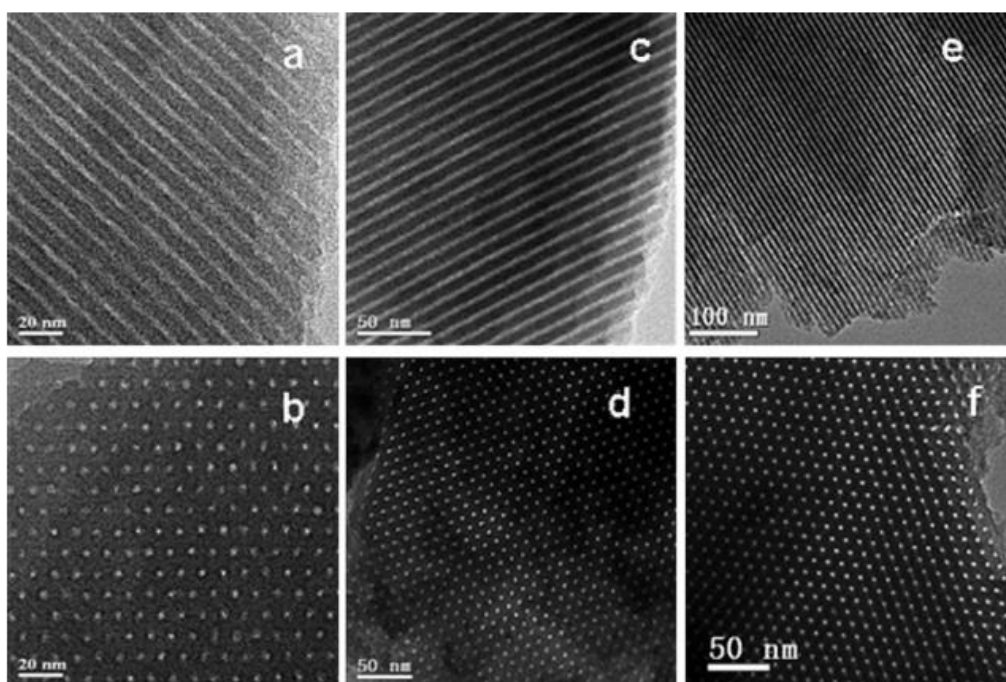


FIGURE 2.6: TEM images of ordered mesoporous carbons viewed along the [110] (a, c and e) and [001] (b, d and f) directions [77].

Optimization of Mesoporous Carbon Synthesis via Definitive Screening Design 3

Published as Libbrecht, W., Deruyck, F., Poelman, H., Verberckmoes, A., Thybaut, J., De Clercq, J., & Van Der Voort, P. (2015). Optimization of soft templated mesoporous carbon synthesis using Definitive Screening Design. *Chemical Engineering Journal*, 259, 126-134. doi:10.1016/j.cej.2014.07.113

In this chapter the synthesis of soft templated mesoporous carbons was optimized with a definitive screening design (DSD), a recently developed design of experiments (DoE) method. Such a design enables to investigate the effect of synthesis parameters including their interactions or quadratic effects, on the material properties with a minimal number of experiments. The DSD was used to find the optimal synthesis conditions to obtain a high mesoporous surface area, which could improve its potential as adsorbent. The optimal conditions were then tested via a validation experiment. The different mesoporous carbons, synthesized according to the DSD, were tested for the adsorption of bisphenol A (BPA). This allowed to investigate the effect of material properties on the adsorption capacity. Via regression analysis, the main factors influencing the adsorption of BPA were investigated.

3.1 Introduction

Mesoporous carbons can be used for various applications, from catalysts and supports, gas storage hosts, electrode materials to adsorbents [21, 72, 77, 83, 116–118]. Among these, soft template mesoporous carbons (SMC), using tri-block copolymer surfactants as templates [26, 61, 119], have attracted a lot of attention [17, 63, 120]. These materials are prepared by polymerizing mainly phenol or resorcinol with formaldehyde around the micelles of e.g. pluronic F127 or P123. The amphiphilic surfactant creates micelles that adopt tailored

3. OPTIMIZATION OF MESOPOROUS CARBON SYNTHESIS VIA DEFINITIVE SCREENING DESIGN

symmetries and interact with the carbon precursor. Via an acid or base catalyzed mechanism the precursors react into a phenolic Novolac or Resol resin [121]. The mesostructure formation is aided by the evaporation induced self-assembly (EISA) at acid or neutral pH conditions or by the self-assembly under weakly basic conditions in a hydrothermal synthesis procedure [28]. Schuster et al. [122] proposed a thermally induced self-assembly based on in-situ SAXS measurements, creating symmetry not in the EISA but during thermopolymerization which cures the resin into a 3D covalent network. In a final carbonization step the surfactant is removed and the polymer transforms into a stable carbon framework.

Various alternative synthesis routes and numerous parameters have been investigated to improve the performance of soft template mesoporous carbons [63,121,123] and as described in Chapter 1. This promising and facile synthesis route is an acid catalyzed evaporation induced self-assembly (EISA). However, a systematic effort to maximize the surface area and the pore volume via design of experiments has, to our knowledge, not yet been performed.

Recently, a new generation of experimental designs, Definitive Screening Design (DSD), was developed which is able to estimate the model coefficients in the descriptive equation for k parameters with only $2k+1$ experiments [124]. The adsorption performance of mesoporous carbons has been studied intensively for dyes [103,125–129], as the hydrophobic carbons show a high affinity towards these organic pollutants [21]. Zhuang et al. [103] found that larger dyes exhibited lower adsorption capacities and pore occupation compared to the smaller dyes because they are unable to enter the micropores.

In the present study, bisphenol A (BPA) was chosen as adsorbate. It is classified as an endocrine disrupting chemical, putting human health and its reproductive system at risk [96,97]. BPA contamination has been detected in industrial wastewater, groundwater, surface water, and even drinking water, making the efficient removal of BPA a priority [130,131]. It is also a well-studied model-adsorbate, with molecular dimensions of 1.068 nm x 0.587 nm x 0.383 nm [100,132–135]. The objectives of this study are understanding the effect of the acid catalyzed EISA synthesis parameters on the material properties of the mesoporous carbons via DSD, finding the optimal set of synthesis parameters for good mesopore formation and investigating the effect of material properties on the adsorption capacity of BPA. The investigated synthesis parameters are mass ratio precursor/surfactant (with pluronic F127 precursor), EISA-time, EISA-contact surface, curing time and carbonization temperature. As material properties, the microporous surface area (S_{micro}), pore volume (V_{micro}), mesoporous surface area (S_{meso}), pore volume (V_{meso}) and carbon content (wt% C) were chosen. Because a carbon with mesopores is the objective, the micropore properties were differentiated from the mesopore properties. Hence, the synthesis parameters that contribute predominantly in the micro- versus mesopores, can be separately identified.

3.2 Experimental

3.2.1 Mesoporous carbon synthesis

The synthesis of a soft templated mesoporous carbon was based on the procedure of Dai and co-workers [18]. For the synthesis with all parameters at central point, 2.2 g of resorcinol ($\geq 99\%$, Sigma Aldrich) and 2.2 g F127 (Sigma Aldrich) were mixed with 9 mL ethanol ($\geq 99.8\%$ purity, VWR) and 9 mL HCl (3M) and stirred for 15 minutes at room temperature in a closed reactor. Then, 2.6 g of formaldehyde (Formalin 37 wt% in water) was added and the solution was stirred again for 15 minutes in a closed reactor. The solution was subsequently poured into a large petri-dish to evaporate the ethanol at room temperature for 15 h. Next, the film was scraped from the petri-dish and put into a Nabertherm muffle oven where the material was cured at 60 °C for 18 h. The cured resin was calcined and carbonized under N₂-flow in a Thermo-lite tubular furnace with a heating rate of 1 °C/min. In a first heating step to 350 °C for 2 h, the surfactant was removed. A second heating step of 2 °C/min to 800 °C for 3 h carbonized the resorcinol/formaldehyde resin. The carbon monolith is then crushed and sieved through a 150 mesh filter.

3.2.2 DSD and data analysis

The design was built around five factors, corresponding with the synthesis parameters, see Section 3.3 for their selection and related ranges. This implies that 11 experiments are required for the DSD. DSD requires 3 levels (minimum, center and maximum) for each factor, to detect and identify any factor causing a strong nonlinear effect. Because the relationship between the material properties Y , also denoted as responses, and the synthesis parameters x_i is expected to be nonlinear involving second order interaction effects, the following model type (Equation 3.1) is proposed. In a DSD the main effects are independent of two-factor interactions and the two factor interactions are not fully confounded but correlated. By using a DSD it is possible to estimate with a minimal number of experiments and with a maximal precision non-confounded main and quadratic effects. Precision of interaction effects is somewhat lower because of co-linearity ($R < 0.5$) between the two-factor interactions.

$$Y = b_0 + b_1x_1 + b_2x_2 + \dots + b_nx_n + \sum b_{ik}x_{ik} + \sum b_{ii}x_i^2 \quad (3.1)$$

The 5 responses considered in the DSD used in the present work are the material properties, a microporous surface area (S_{micro}), pore volume (V_{micro}), mesoporous surface area (S_{meso}), pore volume (V_{meso}) and carbon content (wt% C). Multiple regression analysis quadratic models (Equation 3.1-3.7) were developed for each response to analyze the effect of each synthesis parameter and the effect of its interactions with the other parameters on each response. The significance of each coefficient is tested based on the H_0 hypothesis which assumes that a given coefficient is not significant. Assessment of effect significance is done based on its p-value, the probability for falsely rejecting the H_0 hypothesis. An effect is considered to be significant when $p < 0.05$.

3.2.3 Characterization

Nitrogen gas sorption experiments were conducted at 77 K using a Micromeritics Tristar 3000. Samples were vacuum-dried at 120 °C overnight prior to analysis. The pore size distribution (PSD) was calculated from the adsorption branch using the BJH method. Total pore volume V_{tot} was calculated as the amount of nitrogen adsorbed at a relative pressure of 0.95, V_{micro} and S_{micro} were calculated from the $V-t$ plot. The total surface area S_{BET} was determined using the Brunauer–Emmett–Teller (BET) method. S_{meso} was calculated from the difference between S_{BET} and S_{micro} . Elemental analysis was performed with a CHNS-O analyser Thermo Scientific Flash 2000, with a TCD detector, using the Eager Experience software.

3.2.4 Adsorption tests

Adsorption experiments were performed by adding 10 mg of adsorbent to 100 ml of BPA-solution, (99+% purity, Sigma Aldrich) with BPA-concentrations of 60 mg/l. Subsequently, these solutions were placed in a thermostatic shaking device, Infors HT, multitron standard, for 230 rpm at 25 °C for 24 h. Adsorption equilibrium is reached within 1-2 h already. Next, the solutions were filtered through a 0.45 µm PET syringe filter and the BPA-concentration of the filtrate was analyzed by a Thermo scientific Evolution 60 UV/VIS spectrophotometer at a wavelength of 275 nm. The adsorption capacity was calculated according to Equation 3.2, with q_e (mg/g) the adsorption capacity at equilibrium, C_0 and C_e the initial and equilibrium BPA-concentrations, m the adsorbent mass and V the solution volume. To investigate the relationship between the material properties and the adsorption capacity, a stepwise regression analysis was performed to select the significant parameters. The model was constructed using ordinary least squares.

$$q_e = \frac{(C_0 - C_e)V}{m} \quad (3.2)$$

3.3 Results and Discussion

DSD: synthesis parameter selection and preliminary tests

The synthesis steps of soft template mesoporous carbons are (1) precursor formation, (2) EISA ordering, (3) curing and finally (4) carbonization of the material. In each step, several synthesis parameters can be considered. Due to the high number of variables, a well-considered approach is necessary to select the most important factors for the screening design. Therefore, preliminary experiments were performed and combined with a literature survey. A parameter that has been studied intensively is the precursor/surfactant ratio, which controls the symmetry of the mesostructure [7, 31].

Preliminary experiments confirmed that precursor/surfactant mass ratios of 0.5 and 2 did not result in a mesoporous material. The typical type IV isotherm is no longer visible in the nitrogen sorption measurements in Figure 3.1. The ratio of 2 showed a drastic reduction of the porosity and no mesopores. The ratio of 0.5 however resulted in better material characteristics but with a collapse of the mesostructure and larger pores. The goal is to optimize the synthesis of mesoporous carbons, the presence of mesopores is required and therefore the ratio is selected closer to 0.5. The mass ratio precursor/surfactant was certainly important for mesopore formation and therefore selected as a factor in the DSD, with a minimum of 0.7, 1 as center value and

3. OPTIMIZATION OF MESOPOROUS CARBON SYNTHESIS VIA DEFINITIVE SCREENING DESIGN

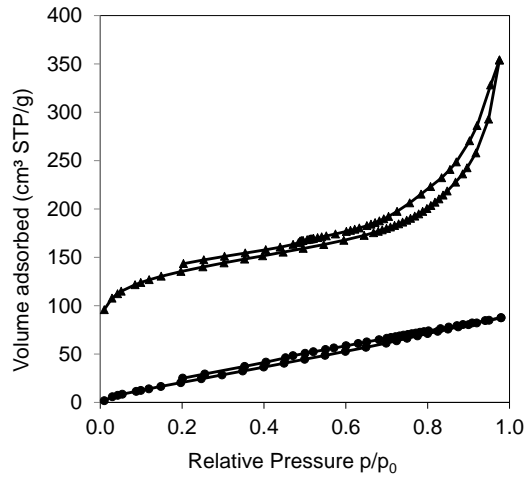


FIGURE 3.1: Nitrogen sorption isotherms with precursor/surfactant ratio 0.5 (triangles) and 2.0 (circles).

a maximum of 1.3.

During the EISA-process, the EISA surface area will determine the evaporation rate. Schlienger et al. [136] found a positive effect between evaporation rate and the ordering of the mesostructure. The duration of the process (EISA time) is also investigated. Both parameters are considered as factors in the DSD, with a minimum of 6 h, resp. 65 cm², 15 h, resp. 143 cm², as center value and a maximum of 24 h, resp. 306 cm².

During curing, also denoted as cross-linking, the pre-polymer is polycondensed into a three dimensional network, building a polymer framework around the template. Since heat curing is mostly applied as cross-linking method, two variables of curing were investigated: temperature and time. Preliminary experiments at curing temperatures of 60 °C and 100 °C showed a negative effect of a higher temperature on the surface area and a broadening of the pore size distribution which indicates a loss of mesostructure. Therefore, the curing temperature was fixed at 60 °C. Test experiments indicated that the duration of curing had an effect on the surface area and pore volume. Therefore, curing time was selected as a factor in the DSD with a minimum of 12 h, 18 h as center value and a maximum of 24 h.

In the final step, the mesoporous resin is carbonized into an amorphous carbon framework. This process has three parameters. A first one is the heat-

Table 3.1: Definitive screening design of 5 factors, with center values marked in bold.

Factor	x_1	x_2	x_3	x_4	x_5
	Carb.	Ratio	EISA	Curing	EISA
	Temp. ($^{\circ}\text{C}$)	p/s	time (h)	time (h)	area (cm^2)
DSD1	800	1.3	24	12	65
DSD2	800	0.7	6	24	306
DSD3	1000	1	6	12	306
DSD4	600	1	24	24	65
DSD5	1000	0.7	15	24	65
DSD6	600	1.3	15	12	306
DSD7	1000	0.7	24	18	306
DSD8	600	1.3	6	18	65
DSD9	1000	1.3	24	24	143
DSD10	600	0.7	6	12	143
DSD11	800	1	15	18	143

ing rate, which is kept slow, $1^{\circ}\text{C}/\text{min}$ and $2^{\circ}\text{C}/\text{min}$, in order to gradually transform the resin into a carbon framework [63]. A second parameter is the carbonization temperature. Mesoporous polymers are formed at temperatures between 400°C and 600°C , while above this temperature carbons are formed. Meng et al. [7] reported a shrinkage of the framework by increasing the temperature from 400°C to 600°C , and a creation of extra microporosity above 600°C . Gorka et al. [137] however, observed an opposite effect: decrease in microporosity with increasing carbonization temperature. Although different synthesis conditions for these mesoporous carbons were used, both indicated an important effect of carbonization temperature.

A second effect that has been reported is the change in surface chemistry by increasing carbonization temperature: higher temperature causes a decrease in oxygen containing functional groups, hereby increasing the hydrophobicity of the surface [7, 138]. Therefore, carbonization temperature was selected as a factor within the DSD, with a minimum of 600°C , 800°C as center value and a maximum of 1000°C . The third parameter is the carbonization time. Because successful carbonization has been reported after 4 h, 3 h and even 2 h, the carbonization time was not included in the DSD and kept constant at 3 h [47, 103, 139].

The number of parameters is kept as low as possible to avoid the risk of overfitting and to yield an accurate estimation of the significant effects. Based on the preliminary experiments and literature review, 5 parameters were selected. The general design structure for the 5 factors and the 11 runs with the appropriate levels is shown in Table 3.1. A randomized experimental sequence was followed in order to minimize the influence of experimental noise by environment effects.

3.4 Characterization of the mesoporous carbons

The N_2 isotherms of all DSD runs, shown in Figure 3.2 (left), were all type IV, typical of mesoporous solids. Three different types of hysteresis (and pore systems) can be observed. (i) experiments 2, 3, 5 and 10 show a H1 hysteresis which indicates cylindrical pores; (ii) the N_2 isotherms of experiments 4, 6, 7 and 11 show a combined H1-H2 hysteresis with a two-step desorption branch, which indicates the formation of plugs within the pores; (iii) experiments 1, 8 and 9 show a pure H2 hysteresis loop indicating ink-bottle pores, which occurs when all the pores have blocked openings [140]. These ink-bottle pores were observed in most materials where high ratios of precursor to surfactant were used.

Table 3.2 shows the material properties of the 11 DSD carbons derived from the isotherms. Microporous surface areas ranged from 79 to 315 m^2/g while mesoporous areas ranged from 66 to 383 m^2/g . Microporous pore volumes varied between 0.03 and 0.13 cm^3/g while mesoporous pore volumes between 0.08 and 0.58 cm^3/g were found. Experiment DSD9 that gave the lowest microporous and mesoporous areas and the lowest volumes, was repeated (DSD9.1) to check if it was an outlier. This repeated DSD9.1 experiment clearly shows it is not an outlier, but represents a combination of very unfavorable synthesis parameters. To improve the DSD results and to verify the reproducibility of the synthesis, two additional experiments (DSD11.1 and DSD11.2) were performed for the center experiment DSD11. The three center points provide quite comparable results which are shown in Table 3.3.

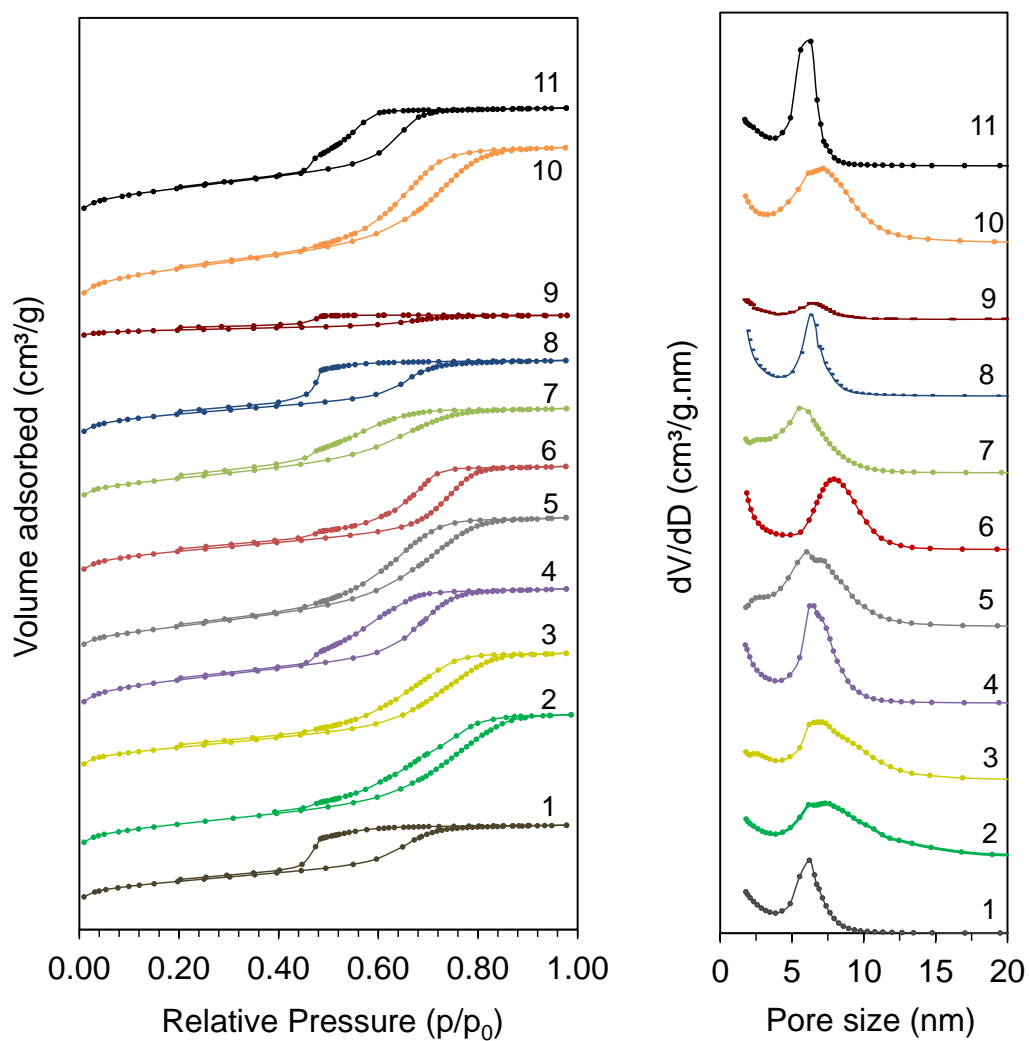


FIGURE 3.2: Nitrogen sorption isotherms (left) with an increasing shift of 150 cm³ STP/g for each isotherm and pore size distributions (right) with a shift of 0.1 cm³/g.nm for each curve of the 11 DSD materials.

3. OPTIMIZATION OF MESOPOROUS CARBON SYNTHESIS VIA DEFINITIVE SCREENING DESIGN

Table 3.2: Material properties of the mesoporous carbons of the DSD experiments.

Material	S_{BET} (m^2/g)	S_{meso} (m^2/g)	S_{micro} (m^2/g)	V_{tot} (cm^3/g)	V_{meso} (cm^3/g)	V_{micro} (cm^3/g)	wt% C (%)	d-value (nm)	D_p (BJH) (nm)
DSD1	554	241	313	0.43	0.30	0.13	94.26	10.3	6.2
DSD2	469	295	174	0.57	0.50	0.07	93.76	13.0	7.3
DSD3	532	260	272	0.55	0.43	0.12	95.75	13.4	6.9
DSD4	530	338	192	0.54	0.46	0.08	90.22	11.3	6.2
DSD5	410	320	90	0.54	0.51	0.03	97.5	10.5	6.0
DSD6	466	265	201	0.49	0.40	0.09	90.16	13.4	7.9
DSD7	497	275	222	0.45	0.36	0.09	94.79	11.0	5.5
DSD8	469	248	221	0.38	0.29	0.09	89.44	10.8	6.2
DSD9	145	66	79	0.11	0.08	0.03	94.31	11.0	6.6
DSD10	676	383	293	0.71	0.58	0.13	90.23	13.0	7.8
DSD11	628	313	315	0.54	0.41	0.10	95.0	10.0	6.3

Table 3.3: Material properties of the reproduced syntheses of DSD9 and DSD11.

Material	S_{BET} (m ² /g)	S_{meso} (m ² /g)	S_{micro} (m ² /g)	V_{tot} (cm ³ /g)	V_{meso} (cm ³ /g)	V_{micro} (cm ³ /g)	D_p (nm)
DSD9	145	66	79	0.11	0.08	0.03	6.6
DSD9.1	200	119	81	0.20	0.17	0.03	7.1
DSD11	628	313	315	0.54	0.41	0.10	6.3
DSD11.1	594	305	289	0.54	0.47	0.07	6.3
DSD11.2	540	304	236	0.53	0.42	0.11	6.3

Table 3.2 also gives the pore diameter, D_p , which ranged between 5.5 and 7.9 nm. Small deviations in diameter could occur due to the different carbonization temperatures because shrinkage is sometimes observed at higher temperatures [66]. The X-ray diffraction pattern of the synthesized mesoporous carbon DSD11 is shown in Figure 3.3. The well resolved (100) and the (110) and (200) peaks indicate a 2D hexagonal symmetry. A well resolved low angle peak was present in the XRD patterns of all samples Figure 3.3. The correspondingly calculated d-values are reported in Table 3.2. In Figure 3.3 a clear 2D hexagonal symmetry was observed for DSD1, 3, 4, 8 and 11. There was no clear effect of varying EISA-parameters on the symmetry of the materials, therefore the ordering of the mesostructure could as well be introduced by thermally induced self-assembly of the material [122]. The elemental analysis (Table 3.2) shows that materials carbonized at 600 °C (DSD4,6,8,10) have a carbon content (wt% C) close to 90%, while a higher carbonization temperature gives a wt % C between 93.76 and 95 (DSD1,2,11) for 800 °C and between 94.31 to 97.5 (DSD3,5,7,9) for 1000 °C. A higher carbonization temperature will remove oxygen containing functionalities from the material, thus increasing the wt% C [7,138].

3.4.1 Definitive Screening Design Model evaluation

The significant effects, i.e., main, interaction or quadratic effects, determining the various responses are listed in Table 3.4, each with its coefficient and the corresponding probability. The p-value is the tail probability in the standard t-distribution curve, it is computed by integrating the standard t-distribution function from t to infinite. A p-value of 0.05 or below 0.05 indicates a significant effect [141].

3. OPTIMIZATION OF MESOPOROUS CARBON SYNTHESIS VIA DEFINITIVE SCREENING DESIGN

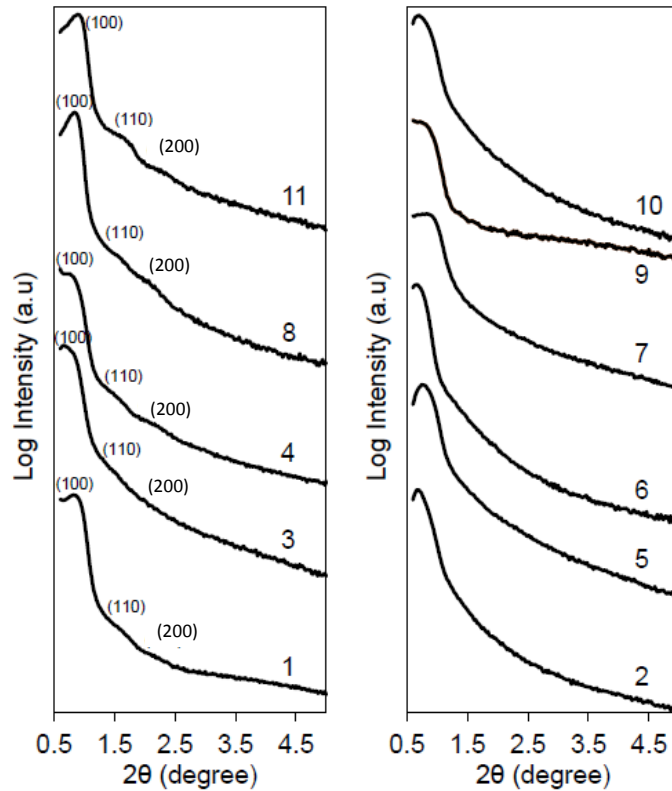


FIGURE 3.3: XRD patterns of ordered 2D hexagonal mesoporous carbons (left) and less ordered carbons (right).

The model for the microporous surface area (S_{micro}), given by Equation 3.3, has an R^2 of 0.89 and its corresponding scatterplot of observations versus predicted responses is shown in Figure 3.4 (left). This model shows a pronounced negative effect of the curing time (x_4) and a quadratic effect of the carbonization temperature (x_1). The model for the microporous volume (Figure 3.4, right), given by Equation 3.4, has an R^2 of 0.89. It shows the same trend as S_{micro} , and identifies the curing time (x_4), the carbonization temperature (x_1), quadratic carbonization temperature (x_1^2) and their interaction effect ($x_1 \cdot x_4$) as significant factors. A longer curing time causes an increased cross-linking within the resin. It is assumed that a more cross-linked resin will be less prone to the creation of micropores (through degradation) at higher temperatures. The quadratic effect observed for the carbonization temperature is a combination of an increase in micropore surface area and pore volume creation up to a certain temperature. This effect is compensated by a decrease and narrowing of micropores at higher carbonization temperatures [48]. The optimal carbonization temperature was found at 840 °C.

Table 3.4: Model coefficients of the significant main, interaction and quadratic effects for the models S_{micro} , V_{micro} , S_{meso} , V_{meso} and wt% C, with their respective p-values.

Synthesis parameters		S_{micro}	V_{micro}	S_{meso}	V_{meso}	wt% C
Constant term		567	0.241	844	1.28	84.7
	p	<0.0001	<0.0001	<0.0001	<0.0001	<0.001
Carbonization T (x_1)		-0.130	-5.03E-05	-0.252	-3.49E-04	0.0123
	p	0.0503	0.0733	0.0008	0.0046	<0.001
Ratio prec/surf (x_2)				-269.1	-0.411	
	p			<0.0001	<0.0001	
Curing time (x_4)		-11.2	-4.91E-03	-3.56	-8.06E-03	
	p	0.0002	0.0002	0.0552	0.0264	
(Carbonization T)* (Carbonization T)		-1.40E-03	-6.23E-07			-4.46E-05
	p	0.0136	0.0118			0.0030
(Carbonization T)* (Curing time)		-3.03E-02	8.02E-07			
	p	0.0214	0.0227			
(Ratio prec/surf)* (Curing time)				-11.4	-0.0212	
	p			0.0867	0.0875	
(Ratio prec/surf)* (Ratio prec/surf)				-541	-0.807	
	p			0.0121	0.0329	

3. OPTIMIZATION OF MESOPOROUS CARBON SYNTHESIS VIA DEFINITIVE SCREENING DESIGN

$$\begin{aligned}
 S_{micro} = & 567 - 0.130x_1 - 11.2x_4 \\
 & - 0.0303[(x_1 - 814)(x_4 - 18.4)] \\
 & - 0.0014[(x_1 - 814)(x_1 - 814)] \quad (3.3)
 \end{aligned}$$

$$\begin{aligned}
 V_{micro} = & 0.241 - 5.03 * 10^{-5}x_1 - 4.91 * 10^{-3}x_4 \\
 & - 8.02[(x_1 - 814)(x_4 - 18.4)] \\
 & - 6.23 * 10^{-7}[(x_1 - 814)(x_1 - 814)] \quad (3.4)
 \end{aligned}$$

$$\begin{aligned}
 S_{meso} = & 844 - 0.252x_1 - 269x_2 - 3.56x_4 \\
 & - 541[(x_2 - 1.02)(x_2 - 1.02)] \\
 & - 11.4[(x_2 - 1.02)(x_4 - 11.4)] \quad (3.5)
 \end{aligned}$$

$$\begin{aligned}
 V_{meso} = & 1.28 - 3.49 * 10^{-4}x_1 - 0.411x_2 - 8.06 * 10^{-3}x_4 \\
 & - 0.807[(x_2 - 1.02)(x_2 - 1.02)] \\
 & - 0.0212[(x_2 - 1.02)(x_4 - 11.4)] \quad (3.6)
 \end{aligned}$$

$$wt\%C = 84.7 - 0.0123x_1 - 4.46 * 10^{-5}[(x_1 - 814)(x_1 - 814)] \quad (3.7)$$

The model for the mesoporous surface area (Figure 3.5 left), given by Equation 3.5, shows a clear negative effect of the ratio precursor/surfactant (x_2), carbonization temperature (x_1) and curing time (x_4). This means that lower values of these parameters will cause an increase in S_{meso} . Longer curing times could be responsible for creating highly cross-linked polymers and more dense carbon materials. Higher carbonization temperatures will cause some shrinking of the mesopores, resulting in a negative effect on S_{meso} and V_{meso} . The quadratic effect of the precursor/surfactant ratio ($x_2 * x_2$) indicates that an optimal value can be found for S_{meso} . At this value, the ideal balance between carbon precursor and the mesostructure creating surfactant is found. Changes in the ratio precursor/surfactant result in different hydrophilic/hydrophobic volume ratios, which will affect the interfacial curvature and resulting mesostructure [123, 138]. The model for V_{meso} (Figure 3.5 right), given by Equation 3.6, contains the same significant factors as the model for S_{meso} : ratio precursor/surfactant (x_2) and its quadratic effect ($x_2 * x_2$), with negative

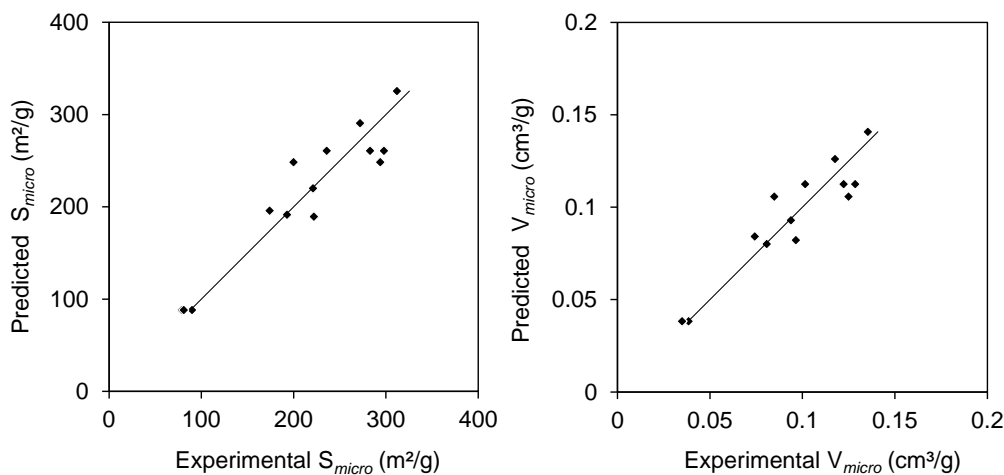


FIGURE 3.4: Predicted versus experimental microporous surface area (left) and microporous volume (right).

effects of carbonization temperature (x_1) and curing time (x_4). The significant factors for S_{meso} and V_{meso} are similar because they are correlated via the pore size.

The model for carbon content with an R^2 of 0.90, described by Equation 3.7, shows a positive and a quadratic effect of the carbonization temperature (x_1) (Figure 3.6). Increasing temperatures will remove oxygen containing functionalities from the surface and increase the carbon content. The quadratic effect indicates that the change in wt% C between 600-800 °C is more pronounced than between 800-1000 °C.

3. OPTIMIZATION OF MESOPOROUS CARBON SYNTHESIS VIA DEFINITIVE SCREENING DESIGN

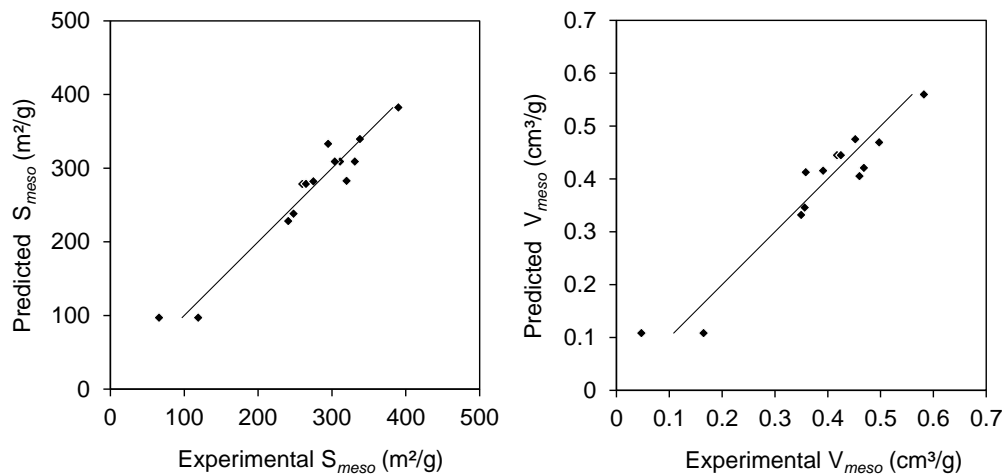


FIGURE 3.5: Predicted versus experimental mesoporous surface area (left) and mesoporous volume (right).

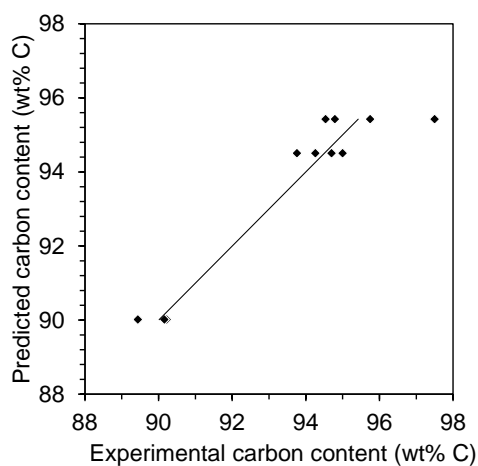


FIGURE 3.6: Predicted versus experimental carbon content.

3.5 Optimization

With the important synthesis parameters for mesopore formation identified, optimal synthesis conditions can be obtained from the model for S_{meso} : Figure 3.7. The quadratic effect for ratio precursor/surfactant gives an optimal value of 0.84 for this ratio. Due to the negative effects of both carbonization temperature and curing time, the lower boundaries of respectively 600 °C and 12 h will give an optimal S_{meso} . A validation experiment was performed with these optimal parameter values. The material properties of this optimal carbon and their predicted values are given in Table 3.5. A high mesoporous surface area, S_{meso} , amounting to 393 m²/g was obtained, which is in agreement with the predicted value for S_{meso} . The microporous surface area S_{micro} differs more substantially from the predicted value. This difference was also observed for S_{micro} in the repeated experiments of DSD11. However, the main focus was the control and optimization of the mesoporous surface area. The N₂-isotherm of the validation experiment in Figure 3.8 showed a type IV isotherm with a H1-type hysteresis. The S_{BET} of 712 m²/g and pore volume of 0.78 cm³/g are higher than reported for acid catalyzed EISA synthesized mesoporous carbons [43,142]. Compared to the base catalyzed phenol/formaldehyde FDU-type material, a higher mesoporous surface area of 393 m²/g is produced. The FDU materials typically have a higher fraction of micropores, yielding a higher total surface area. Pore volumes of the optimized material exceed these of the FDU materials [7].

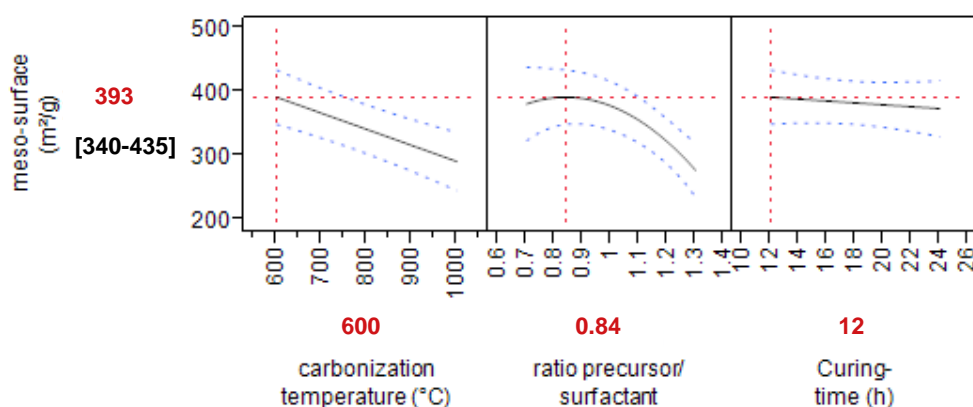


FIGURE 3.7: Optimal values for the significant parameters influencing the mesoporous surface area, and the predicted value (red) together with the lower and upper limits (blue).

3. OPTIMIZATION OF MESOPOROUS CARBON SYNTHESIS VIA DEFINITIVE SCREENING DESIGN

Table 3.5: Material properties of the mesoporous carbon and predicted values with optimized S_{meso} .

Material	S_{BET} (m^2/g)	S_{meso} (m^2/g)	S_{micro} (m^2/g)	V_{tot} (cm^3/g)	V_{meso} (cm^3/g)	V_{micro} (cm^3/g)	Dp (nm)	wt% C C (%)
Optimal	712	393	319	0.78	0.64	0.14	7.8	87.1
Predicted	647	393	250	0.64	0.52	0.12	-	90.1

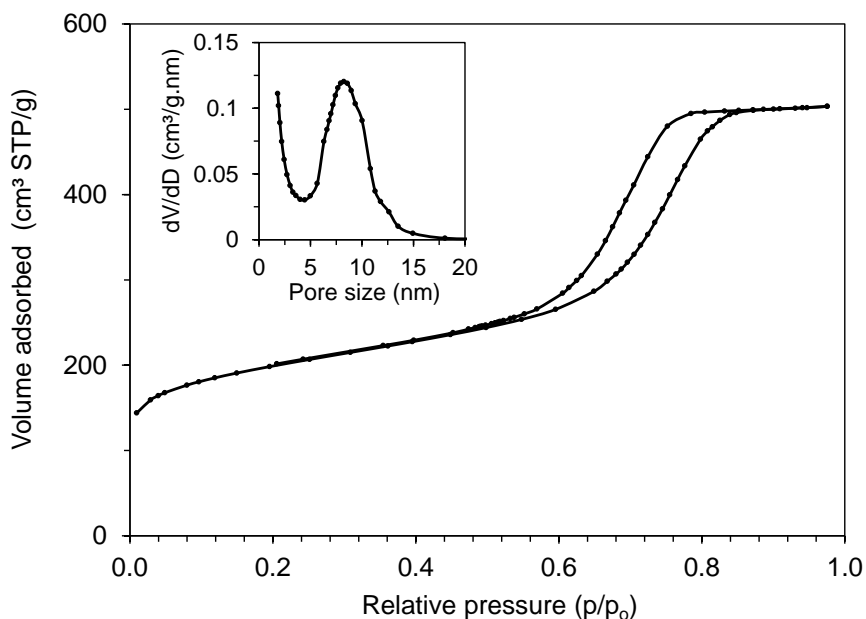


FIGURE 3.8: Nitrogen sorption isotherms and pore size distribution (inset) for the mesoporous carbon with optimized S_{meso} .

3.6 Adsorption experiments

A time resolved uptake of BPA on one DSD material showed that after 1-2 h equilibrium was reached. Adsorption capacities at equilibrium were measured after 24 h. The results of the adsorption tests with the different DSD materials are shown in Table 3.6. The adsorption capacity ranged from 12 mg/g to 163 mg/g. Carbon DSD9 with very poor material properties (see Table 3.2: S_{BET} of 145 m^2/g and V_{tot} of 0.11 cm^3/g) has the lowest adsorption capacity, whereas the highest adsorption capacities were found for materials DSD5 and DSD11, with mesoporous surface areas exceeding 300 m^2/g . These carbons outperform activated carbon materials from wood and carbon nan-

otubes which had a maximum adsorption capacity (q_{max}) of respectively 30 mg/g [133] and 70 mg/g [143]. The mesoporous carbons perform almost as good as graphene which in recent studies proved to be a suitable adsorbent for BPA with a q_{max} of 181.6 mg/g [134]. The best adsorbent for BPA reported so far is an activated carbon modified by a sequential N₂ and air treatment at 600 °C, with a q_{max} of 432 mg/g [144].

Table 3.6: Experimental adsorption capacities ($q_{e,exp}$) for the DSD materials and the optimal material and the predicted adsorption capacities $q_{e,pred}$ for the model with and without DSD 1, 8, 9.

Experiment	$q_{e,exp}$ (mg/g)	$q_{e,pred1}$ (mg/g)	$q_{e,pred2}$ (mg/g)
DSD1	61	95*	110
DSD2	139	120	128
DSD3	130	121	129
DSD4	114	109	117
DSD5	163	171	166
DSD6	88	68	88
DSD7	118	119	128
DSD8	28	52*	76
DSD9	12	2*	44
DSD10	136	137	137
DSD11	154	149	149

*large deviation from predicted adsorption capacity due to ink-bottle pores.

The effects of material characteristics, such as micro- and mesoporous volume and surface area and carbon content, on the adsorption capacity were modeled by stepwise regression analysis. This model (Equation 3.8, Figure 3.9 left), with an R^2 of 0.89, shows only two significant main effects: the mesoporous surface area and the carbon content. The increase of adsorption capacity with mesoporous surface area is obvious: a higher mesoporous surface area provides more accessible adsorption sites per gram of material. A higher carbon content indicates a more hydrophobic adsorbent. Because the interactions between BPA and the carbon material are mainly $\pi - \pi$ interactions [134, 144, 145], BPA is expected to adsorb more readily on hydrophobic adsorbents. This is clearly present in Equation 3.8, showing a significant pos-

3. OPTIMIZATION OF MESOPOROUS CARBON SYNTHESIS VIA DEFINITIVE SCREENING DESIGN

itive effect between carbon content and adsorption capacity.

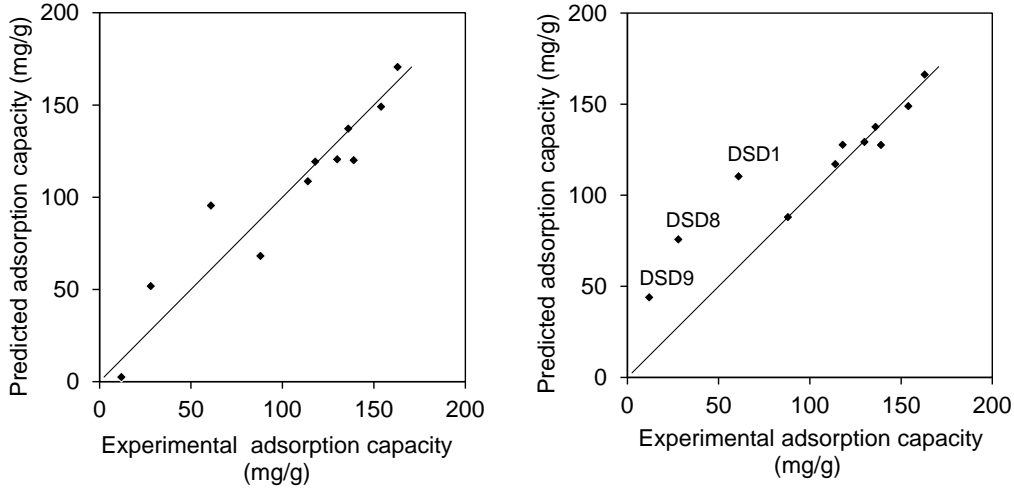


FIGURE 3.9: Predicted versus experimental adsorption capacity with S_{meso} and wt% C as significant factors with DSD1, 8, 9 (left) following Equation 3.8 and without DSD1, 8, 9 (right) following Equation 3.9.

Large deviations between predicted and experimental adsorption capacities (Table 3.6) are observed for the DSD1, DSD8 and DSD9 materials. These carbons showed ink-bottle pores in the N_2 -isotherms (Figure 3.2 left). These ink-bottle pores make it more difficult for BPA to enter the pores, lowering the adsorption capacity. DSD1 and DSD8 were clearly statistical outliers, based on the residual plot. By omitting the materials with ink-bottle pores (DSD1, DSD8 and DSD9), an improved model (Figure 3.9 right, Equation 3.9), with an R^2 of 0.92, and residual plot were found. The material derived from the optimization of the synthesis towards S_{meso} showed an adsorption capacity of 112 mg/g, an intermediate value. The positive effect from the high S_{meso} is countered by a decrease in adsorption due to the low carbon content or lower hydrophobicity.

$$q_{e,pred1} = 1039 + 0.543 * S_{meso} + 10.7 * wt\%C \quad (3.8)$$

$$q_{e,pred2} = 703.3 + 0.387 * S_{meso} + 7.64 * wt\%C \quad (3.9)$$

3.7 Conclusions

The effect of synthesis parameters on the structural characteristics of acid catalyzed EISA mesoporous carbons was investigated via DSD. From the investigated synthesis parameters, i.e., mass ratio precursor/surfactant, EISA-time, EISA-contact surface, curing time and carbonization temperature, microporosity of the carbon was found to decrease with curing time because of increased cross-linking, which could make micropore formation due to degradation harder. The quadratic effect observed for the carbonization temperature is a combination of micropore creation up to a certain temperature with a decrease and narrowing of micropores at higher carbonization temperatures, an optimum carbonization temperature of 840 °C was determined. The most significant factor for mesopore formation was the precursor to surfactant mass ratio, for which an optimum was found at 0.84. Both carbonization temperature and curing time showed a negative effect on S_{meso} and V_{meso} and should be kept low.

The optimal set of synthesis parameters for an optimal mesopore surface area of the carbon was identified and validated. The optimized synthesis gave a carbon with a high S_{meso} of 393 m²/g, a total pore volume of 0.78 cm³/g and a total surface area of 712 m²/g, which is higher than reported in literature for SMCs synthesized via the acid catalyzed EISA procedure. Subsequently, the potential use of the mesoporous carbons as adsorbent for BPA was investigated via stepwise regression analysis. This gave insight into the relationship between the structural characteristics and the BPA adsorption performance of the DSD carbons. This analysis identified S_{meso} and wt% C as significant factors. A higher carbon content or a more hydrophobic surface area, due to the adsorption involving mainly $\pi - \pi$ interactions, as well as a higher mesoporous surface area, increased the adsorption capacity.

Tuning the Pore Geometry of Ordered Mesoporous Carbons for Enhanced Adsorption of Bisphenol-A

4

Published as Libbrecht, W., Vandaele, K., De Buysser, K., Verberckmoes, A., Thybaut, J., Poelman, H., De Clercq, J., Van Der Voort, P. (2015). Tuning the Pore Geometry of Ordered Mesoporous Carbons for Enhanced Adsorption of Bisphenol-A. *Materials*, 8(4), 1652-1665. doi:10.3390/ma8041652

In this chapter, mesoporous carbons were synthesized via both soft and hard template methods and compared to a commercial activated carbon (AC) for the adsorption ability of bisphenol A (BPA) from an aqueous solution. The three porous carbons were fully characterized and the material properties were investigated to identify their effect on the adsorption of BPA. Both equilibrium and kinetic studies were performed on the materials.

4.1 Introduction

Porous carbon materials are important in many areas of modern science and technology, with a wide variety of applications, such as catalyst support, electrode material and adsorbents for gas and liquid purification [63]. The popularity of these materials can be attributed to their high specific area, large pore volume, chemical inertness and good mechanical stability [14, 55]. Activated carbon (AC) is the most commonly applied carbon material for adsorption due to its low production cost and the possibility for large scale processing. Major disadvantages are the disordered structure, limitation of pore size to micropores (<2 nm) and irregular pore size distribution. The micropores could limit the mass transfer [100], or decrease pore accessibility for larger adsorbates. Further developments in the field of chromatography, Li-based

4. TUNING THE PORE GEOMETRY OF ORDERED MESOPOROUS CARBONS FOR ENHANCED ADSORPTION OF BISPHENOL-A

batteries, electrodes and adsorption demand for materials with increased pore sizes and a controlled pore size distribution [21, 24].

The first hard templated ordered mesoporous carbons that were synthesized, used MCM-48 mesoporous silica molecular sieves as template. The resulting replicated mesoporous carbon CMK-1 exhibited porous structures consisting of two disconnected interwoven three-dimensional pore systems [146]. In a similar manner, a well-defined hexagonally ordered mesoporous carbon denoted CMK-3, was synthesized by using SBA-15 mesoporous silica as template [147]. Next to sucrose solution, as in the original paper [6], also furfuryl alcohol or other carbon precursors such as glucose, xylose, acenaphthene, indene, etc. were impregnated in the silica template via the incipient wetness technique [14, 148, 149]. Therefore, an amount of precursor solution equal to the total pore volume of the template is added. It is believed that the whole solution infiltrated the pores through capillary action. The carbon precursor was typically polymerized by means of a sulfuric acid catalyst and subsequently carbonized under inert conditions. The silica template can be removed either under basic conditions or by means of HF. Unfortunately, in all of the above-mentioned methods, the incipient wetness technique was unsuccessful to fill the pores uniformly due to the difficulty to homogenize a powder. Also pore blocking occurs when subsequent impregnations of a precursor solution via the wet impregnation method are performed. In order to obtain a high surface area, it is important that no carbon precursor is deposited outside the template because this would lead to external carbon upon calcination.

Soft templated synthesis of ordered mesoporous materials by self-assembly of tri-block copolymer surfactants and carbon precursor was pioneered by Dai et al., Nishiyama et al. and Zhao et al. [26, 42, 47]. Variation of morphology is possible by applying different reaction parameters or synthesis mechanisms as described in Chapter 1.

To investigate the adsorption capabilities of both mesoporous carbons: soft templated (SMC) and hard templated (CMK-3), BPA was chosen as an adsorbate because it is classified as an endocrine disrupting chemical, putting human health and its reproductive system at risk, which makes the efficient removal of BPA a priority [96, 97, 130, 150]. The adsorption of BPA on activated carbon has been studied intensively [98, 133, 144], and maximum adsorption capacities (q_{max}) from 30 mg/g [133] to as high as 430 mg/g are reported [144]. Important differences are the natural source of the AC, varying from wood [144], to coconut shell [98], to charcoal [144], which will affect the specific surface area as well as surface chemistry by altering the amount of acidic oxygen-containing groups. More recently developed advanced carbon materials tested for BPA adsorption were carbon nanotubes [143] and graphene sheets [65] with a q_{max} of, respectively, 70 mg/g and 182 mg/g.

The objective of this study was to understand the effect of different material characteristics, such as specific surface area, hydrophobicity, pore diameter and pore geometry on the adsorption of BPA by comparing both types of mesoporous carbons and commercial activated carbon. A simple method for the synthesis of CMK-3 was developed. In this synthesis toluene is added after furfuryl alcohol impregnation to avoid the deposit of excess furfuryl alcohol onto the external surface of the silica template. This resulted in a high surface area CMK-3 with well-ordered symmetry. Also, the quick and easy acid-catalyzed EISA synthesis for soft template mesoporous from Chapter 3 is used. The synthesis can be performed at room temperature without any pH adjustments or purification steps and results in a well-ordered 2D hexagonal mesoporous material.

4.2 Experimental Section

4.2.1 Synthesis of Ordered Mesoporous Carbons

A commercial activated carbon was supplied by Desotec (Roeselare, Belgium). For the hard templated mesoporous carbon CMK-3 synthesis, 2.5 g of the template SBA-15 was impregnated with 10 mL solution of 25 v% furfuryl alcohol ($\geq 98\%$ purity, Sigma-Aldrich) in toluene ($\geq 99.5\%$ purity, Sigma-Aldrich). To catalyze the reaction, 200 μL of 0.1 M H_2SO_4 (Sigma-Aldrich) is added. The solution was refluxed for 36 h at 90 °C while stirring vigorously. Next, the impregnated silica is filtered and washed 3 times with toluene and dried at 150 °C for 5 h in a Nabertherm muffle oven. The composite material is carbonized at 1100 °C for 1 h in a Carbolite tubular furnace under 5% H_2 in Ar atmosphere with a heating rate of 2 °C/min. The silica is leached out by stirring with a 10% HF solution (Sigma-Aldrich) for a minimum of 6 h. Less than 3 wt % SiO_2 was detected in the CMK-3 by X-ray fluorescence (Rigaku NEX CG, Tokyo, Japan).

The soft templated mesoporous carbon synthesis of Chapter 3 was used. Resorcinol (2.2 g; Sigma-Aldrich) and F127 (2.2 g; Sigma-Aldrich) were mixed with 9 mL ethanol (99.8% purity VWR) and 9 mL HCl (3 M) and stirring for 15 min at room temperature. Then, 2.6 g of formaldehyde (Formalin, 37 wt % formaldehyde in water; Sigma-Aldrich) was added and the solution was stirred again for 15 min. The solution was subsequently poured onto a glass plate to evaporate the ethanol at room temperature for 6 h. Next, the film was scraped from the glass plate and put into a petri-dish in a Nabertherm muffle oven where the material was cured at 60 °C for 12 h. The cured resin was calcined and carbonized under N_2 -flow in a Thermolite tubular furnace with a heating rate of 1 °C/min. In the first heating step to 350 °C for 2 h, the

surfactant was removed. The second heating step to 800 °C for 3 h carbonized the resorcinol/formaldehyde resin.

4.2.2 Adsorption Tests

Kinetic experiments were performed by adding 100 mg of adsorbent with a particle size of 62 to 88 µm to 1 L of 30 mg/L BPA (>99% purity; Sigma-Aldrich) solution. These mixtures were stirred at room temperature at 600 rpm. 5 mL samples were taken at different time intervals up to 100 min, filtered through a 0.45 µm PET syringe filter and the BPA concentrations were analyzed with a Thermo scientific Evolution 60 UV/VIS spectrophotometer at a wavelength of 275 nm. In order to ascertain that the obtained data are free from external diffusion limitations across the solid-liquid interface, preliminary kinetic experiments at different agitation speeds (300, 600 and 900 rpm) confirmed that external mass transfer resistance is negligible from an agitation speed of 600 rpm for all three adsorbents (results not shown) [151].

The internal mass-transfer effect was studied by using different adsorbent particle sizes for AC and SMC. Both materials were crushed and sieved in three different particle sizes (62–88 µm, 177–250 µm and 510–700 µm) with a Mini-sieve micro sieve set (Sigma-Aldrich). No visual deterioration of the particles was observed after the adsorption tests, more accurate measurements of the particle size could be performed via dynamic light scattering (DLS). Because CMK-3 is a very fine powder, only the smallest particle size fraction was available. Pelletizing of CMK-3 gave larger particle sizes, however upon mixing in solution the particles disintegrated back to the very fine powder.

Isotherm experiments were performed by adding 10 mg of adsorbent to 100 mL of aqueous BPA solution with different BPA concentrations (ranging from 5 mg/L to 70 mg/L). Subsequently, the solutions were placed in a thermostatic shaking device (Infors HT, multitron standard) at 25 °C for 24 h. Next, the solutions were filtered through a 0.45 µm PET syringe filter and analyzed for its BPA concentrations. Both kinetic and isotherm experiments were performed in triplicate. The adsorption capacity at time t was calculated according to Equation 4.1.

$$q_t = \frac{(C_0 - C_t)V}{m} \quad (4.1)$$

with q_t (mg/g) the adsorption capacity at time t, C_0 (mg/L) and C_t (mg/L) the initial concentration and concentration at time t, m (g) the adsorbent mass and V (L) the solution volume.

The isotherm data were fitted to the well-known Langmuir (Equation 4.2) and Freundlich (Equation 4.3) isotherms.

$$q_e = \frac{(q_{max}K_L C_e)}{1 + K_L C_e} \quad (4.2)$$

$$q_e = K_F C_e^{1/n} \quad (4.3)$$

with q_{max} (mg/g) the maximum adsorption capacity, C_e (mg/L) the equilibrium concentration, K_L (L/mg) the Langmuir constant, K_F (mgL^{1/n})/(mg^{1/n}g) and n (-) the Freundlich constants.

The kinetic data were fitted to the pseudo-first-order (Equation 4.4), the pseudo-second-order (Equation 4.5), and the Weber-Morris kinetic model (Equation 4.6).

$$q_t = q_e(1 - e^{-k_1 t}) \quad (4.4)$$

$$q_t = \frac{q_e t}{\frac{1}{k_2 q_e} + t} \quad (4.5)$$

$$q_t = k_d t^{1/2} + C \quad (4.6)$$

with k_1 (1/min) the pseudo-first-order rate constant, k_2 (g/(mg min)) the pseudo-second-order rate constant, k_d (min g/mg) the intraparticle diffusion rate constant and C (mg/g) the intercept.

4.3 Results and Discussion

4.3.1 Characterization of the Adsorbents

The N₂-isotherms of the three adsorbents are shown in Figure 4.1. The specific surface areas, pore volumes, and density functional theory (DFT) pore diameters are listed in Table 4.1. The AC surface area and pore volume are 1027 m²/g and 0.50 cm³/g, respectively, containing mainly micropores, confirmed by the type I isotherm, with a pore diameter below 2.5 nm. The CMK-3 material has a very high surface area (1420 m²/g) and pore volume (1.14 cm³/g) with a pore diameter of 4 nm. The soft templated mesoporous carbon (SMC) has a surface area of 476 m²/g, pore volume of 0.49 cm³/g and an average pore diameter of 7.2 nm. Both mesoporous materials exhibit a type IV isotherm with a type H1 hysteresis indicating uniform cylindrical pores. The capillary condensation of CMK-3 occurs at a lower p/p₀ than SMC indicating a smaller pore size as seen in Table 4.1.

Table 4.1: Structural properties of the carbon adsorbents.

Material	S_{BET} (m ² /g)	V_{tot} (cm ³ /g)	D_p (nm)	Unit cell parameter a (nm)	Wall thickness h (nm)
AC	1027	0.50	<3	-	-
CMK-3	1420	1.14	4.0	9.6	5.6
SMC	476	0.49	7.0	11.6	4.6

Powder X-ray diffraction patterns of the synthesized mesoporous carbons are shown in Figure 4.2. The SMC shows a well resolved (100) reflection at $2\theta = 0.88^\circ$ and high order reflection (110) and (200) of the highly ordered 2D hexagonal symmetry. The CMK-3 material also shows a (100) reflection at $2\theta = 1.06^\circ$ with higher order reflections indicating the 2D hexagonal symmetry. The cell parameter (a_0) of SMC and CMK-3 were calculated from d(100), d(110) and d(200) and were 11.6 nm and 9.6 nm, respectively. The successful synthesis of highly ordered hard and soft template mesoporous carbons was validated by the TEM images of Figure 4.3. Both pore size diameters and structures are in agreement with nitrogen sorption isotherms and XRD patterns.

The elemental analysis (Table 4.2) shows a 93 wt % carbon for both mesoporous carbons. These materials consist mainly of pure carbon walls with a small amount of oxygen containing functional groups. The AC on the other hand has about 86 wt % carbon and a higher amount of oxygen (Table 4.2),

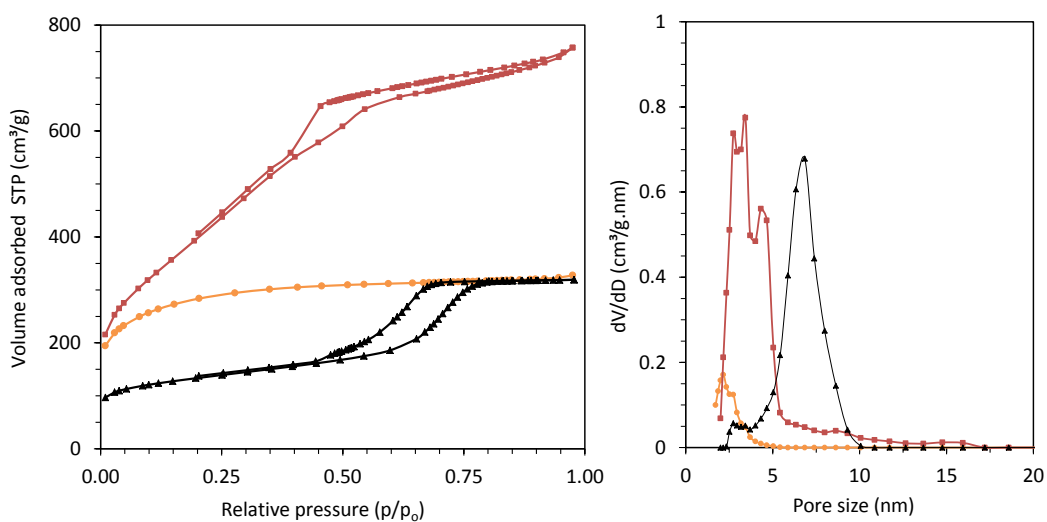


FIGURE 4.1: N₂ sorption isotherms (left) and their corresponding pore size distributions obtained by density functional theory (DFT) method (right) of CMK-3 (■), AC (●) and SMC (▲).

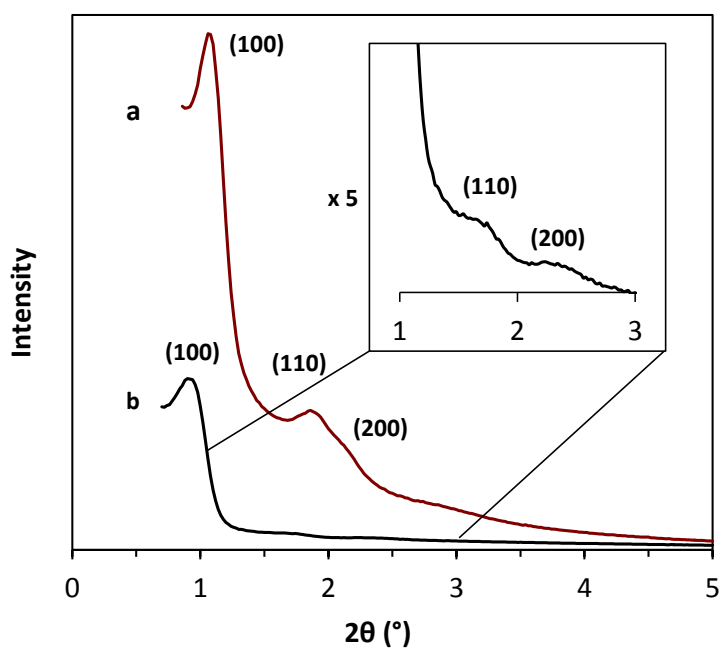


FIGURE 4.2: Powder X-ray diffraction patterns of CMK-3 (a) and SMC (b).

4. TUNING THE PORE GEOMETRY OF ORDERED MESOPOROUS CARBONS FOR ENHANCED ADSORPTION OF BISPHENOL-A

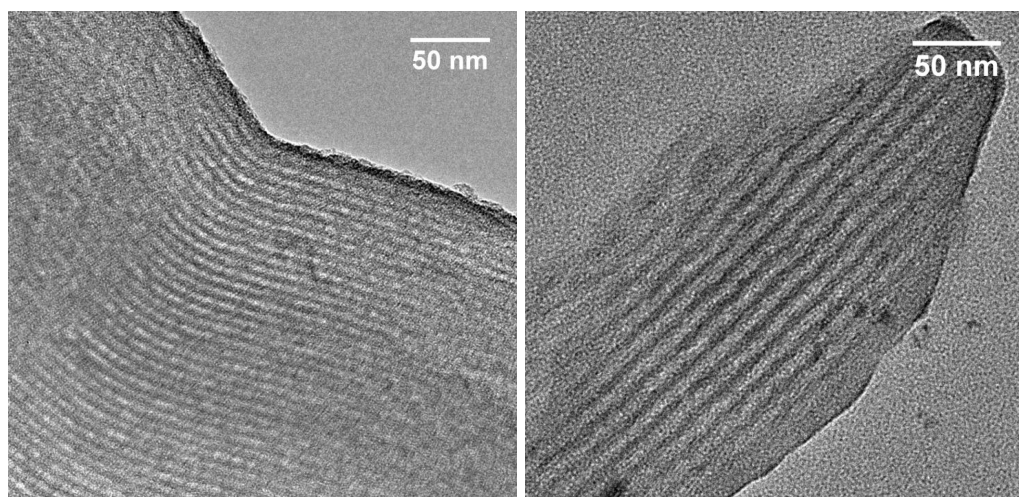


FIGURE 4.3: Transmission electron microscope (TEM) images of CMK-3 (left) and SMC (right).

Table 4.2: Elemental composition of the three carbon adsorbents.

Material	Elemental analysis (wt%)			
	C	H	N	O*
AC	85.90	0.45	0.29	13.36
CMK-3	93.33	0.68	0.07	5.92
SMC	93.93	0.50	0.08	5.49

* $100 - \text{wt}\% (\text{C} + \text{H} + \text{N})$

which is due to the steam activation process during production. The increasing carbon or decreasing oxygen amount indicates a more hydrophobic surface of the mesoporous carbons [24, 144]. Because the interactions between BPA and the carbon material are mainly π - π interactions, BPA is expected to adsorb more readily on hydrophobic adsorbents [134, 152].

4.3.2 Adsorption Isotherms

Figure 4.4 shows the adsorption isotherms of CMK-3, SMC and AC. CMK-3 has the highest adsorption capacity, followed by AC and SMC. The experimental data were fitted with Langmuir and Freundlich isotherms (Table 4.3). The isotherms of the mesoporous materials are better described by the Freundlich model (Equation 4.3), while the experimental AC-data are better described by the Langmuir model (Equation 4.2). This implies multilayer adsorption could occur within the wide pores of the mesoporous materials, while for AC, mainly consisting of micropores, adsorption will be limited to a monolayer. The observed maximum adsorption capacities are 474 mg/g, 290 mg/g, and 154 mg/g for, respectively, CMK-3, AC and SMC. To the best of our knowledge the adsorption capacity of 474 mg/g for CMK-3 is the highest reported.

Table 4.3: The observed maximum adsorption capacity in mg/g and converted to molecules per nm², parameters describing the adsorption isotherms of BPA on AC, CMK-3 and SMC modeled by Langmuir and Freundlich.

Material	Experimental		Langmuir			Freundlich		
	q_{max} (mg/g)	Adsorbed BPA (molecules/nm ²)	q_{max} (mg/g)	KL (L/mg)	R ²	1/n	KF ((mgL ^{1/n})/(mg ^{1/n} g))	R ²
AC	290	0.75	307	0.64	0.98	0.14	181	0.93
CMK-3	474	0.88	447	2.81	0.82	0.12	296	0.99
SMC	154	0.86	156	0.40	0.87	0.19	74	0.98

BPA adsorption from water on a carbon adsorbent is mainly influenced by specific surface area and hydrophobicity of the surface due to π - π interactions between BPA and the adsorbate [93, 134, 152]. As the specific surface area increases from SMC, over AC to CMK-3 (Table 4.1), the adsorbed BPA amount increases. To compare the materials without the effect of specific surface area, the observed maximum adsorption capacities are converted to the number of adsorbed molecules per nm² (Table 4.3). The more hydrophobic mesoporous carbons, CMK-3 and SMC, with about 94 wt% carbon, have a higher amount of molecules adsorbed per nm²: 0.88 molecules/nm² and 0.86 molecules/nm² compared to the less hydrophobic AC (0.75 molecules per nm²).

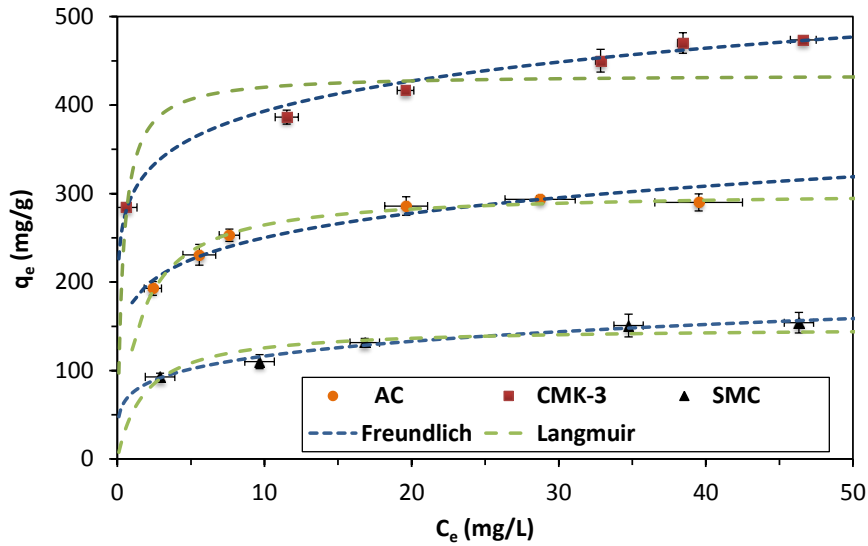


FIGURE 4.4: Adsorption isotherms of 10 mg of CMK-3 (■), AC (●) and SMC (▲) in 100 mL of BPA-solution, experimental data were fitted with the Langmuir and Freundlich model, the error bars represent the standard deviation of the triplicate measurements.

4.3.3 Adsorption Kinetics

The adsorption kinetics of BPA on AC, CMK-3 and SMC for the smallest particle size (62–88 μm) are shown in Figure 4.5, where the adsorption capacity q_t , normalized to the equilibrium adsorption capacity q_e is given as function of time. This allows comparison of the three materials with different equilibrium adsorption capacities (q_e) and therefore a different driving force for BPA removal. It is clear that adsorption on CMK-3 is the fastest, reaching equilibrium after 20 min. SMC reaches equilibrium at about 60 min, while AC has not yet reached equilibrium after 90 min. It is noteworthy that SMC adsorbs faster than AC, although SMC has a lower equilibrium adsorption capacity than AC: 154 mg/g versus 290 mg/g.

The experimental data were fitted with the pseudo-first-order, pseudo-second-order and Weber-Morris kinetic model (Table 4.4). The kinetics for all three materials were best described by the pseudo-second-order kinetic model. The adsorption kinetics of organic pollutants on carbon materials

has often been described with pseudo-second-order kinetics [98, 100, 134, 144]. Based on the Weber-Morris kinetic model, a plot of q_t versus $t^{1/2}$ should be linear if intraparticle diffusion was involved in the adsorption process. Moreover, if the straight line passes through the origin, intraparticle diffusion is the rate-determining step. Only the AC data showed a straight line, with an extrapolation passing almost through the origin. This suggests that intraparticle diffusion contributes to the adsorption kinetics of AC.

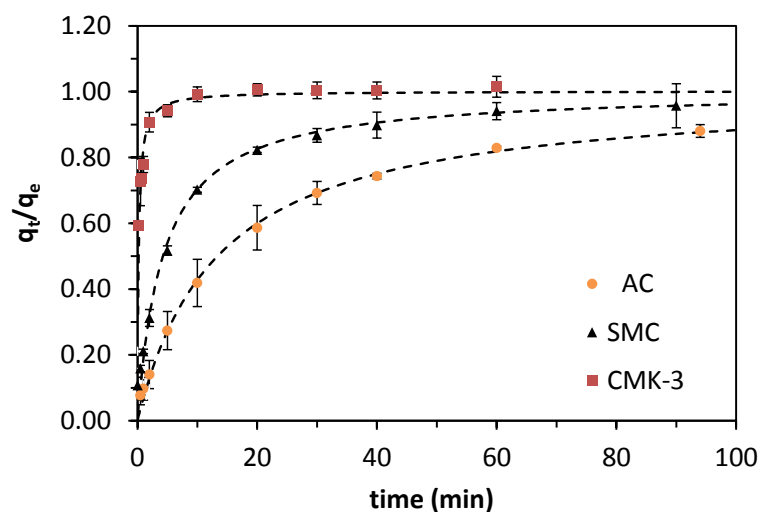


FIGURE 4.5: Adsorption kinetics of 100 mg of CMk-3 (■), AC (●) and SMC (▲) in 1 L of 60 mg/L BPA-solution, particle size is between 62 and 88 μm , the error bars represent the standard deviation of the triplicate measurements, the dashed lines represent the pseudo-second-order kinetic model descriptions.

Table 4.4: Parameters of the pseudo-first-order, pseudo-second-order and Weber-Morris kinetic models for adsorption of BPA on AC, CMK-3 and SMC.

Material	Pseudo-first-order model				Pseudo-second-order model				Weber-Morris		
	$q_{e(\text{exp})}$ (mg/g)	$q_{e(\text{calc})}$ (mg/g)	k_1 (1/min)	R^2	$q_{e(\text{calc})}$ (mg/g)	k_2 (g/(mg min))	$t^{1/2}$ min	R^2	k_d (min g/mg)	C (mg/g)	R^2
AC	277	264	0.0657	0.98	315	0.00024	13.4	0.99	31.2	13.2	0.94
CMK-3	295	281	2.64	0.77	291	0.01647	0.208	0.96	13.7	215	0.65
SMC	147	137	0.0236	0.97	149	0.00157	4.27	0.99	15.0	29.6	0.86

Although the BPA-molecule with molecular dimensions of $1.068 \text{ nm} \times 0.587 \text{ nm} \times 0.383 \text{ nm}$ [132–135] is able to enter micropores and AC has been reported as a successful adsorbent in multiple studies [98, 144, 153], the observed

4. TUNING THE PORE GEOMETRY OF ORDERED MESOPOROUS CARBONS FOR ENHANCED ADSORPTION OF BISPHENOL-A

adsorption kinetics in Figure 4.5 show that the larger pores of mesoporous carbons increase the efficiency of these materials beyond that of AC. This is consistent with literature reporting that the use of mesoporous materials as adsorbent has proven to increase adsorption rate and efficiencies [19,24,100]. The BPA molecule diffuses more readily in the larger mesopores and is adsorbed faster. The difference in rate between CMK-3 and SMC can be attributed to the pore geometry. SMC consists of 2D hexagonal arranged long pores, while CMK-3 consists of interconnected nanorods (Figure 4.6). This open pore system of CMK-3 allows for a faster intraparticle diffusion and removal rate of the adsorbate, as observed in Figure 4.5.

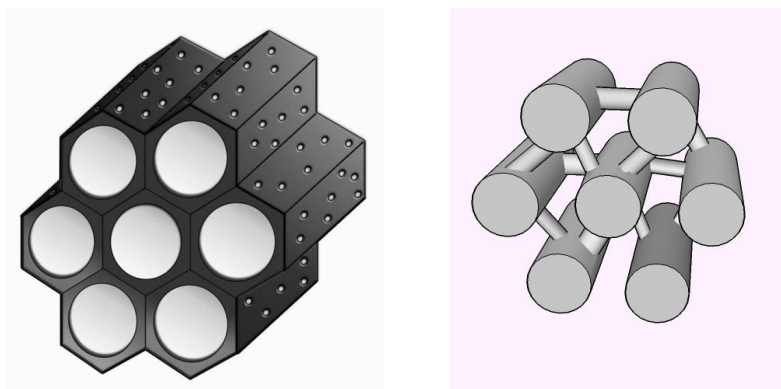


FIGURE 4.6: Schematic representation of 2D hexagonal mesoporous structure of SMC (left) and the interconnected nanorod structure of CMK-3 (right).

The effect of particle size on the adsorption kinetics was further investigated for SMC and AC (Figure 4.7). With increasing particle size, the removal rate of BPA on AC is considerably lowered. The irregular structured micropores of the AC particles clearly indicate that intraparticle diffusion is the rate-controlling step. This was also confirmed by fitting the AC data of Figure 4.1 to the Weber-Morris kinetic model (Table 4.5).

Remarkably, in the SMC with larger pores and a well-ordered structure, intraparticle diffusion also controls the removal rate (Figure 4.7). This could be explained by the pore structure: in larger particles, the average distance travelled by diffusion in the long 2D hexagonal pores will be longer. Fitting the SMC data of Figure 4.7 to the Weber-Morris kinetic model confirmed the contribution of intraparticle diffusion in larger SMC particles (Table 4.5). However, the effect was much smaller than in AC, the removal rate of BPA

on SMC is still higher than that of AC, because the mesopores allow a better diffusion through the material.

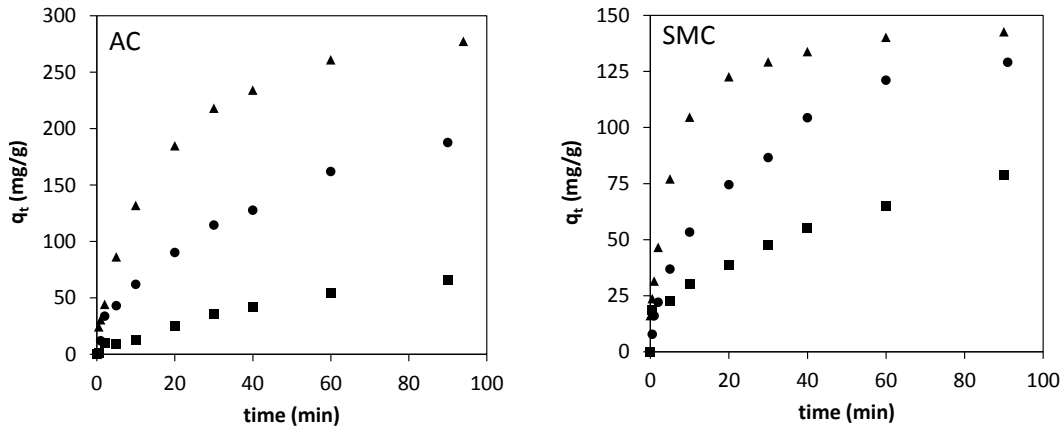


FIGURE 4.7: Effect of particle size 62–88 μm (\blacktriangle), 177–250 μm (\bullet) and 510–700 μm (\blacksquare), on the adsorption kinetics of 100 mg of AC (left) or SMC in 1 L of 60 mg/L BPA-solution (right).

Table 4.5: Parameters of the Weber-Morris kinetic model for adsorption of BPA on AC and SMC with different particle sizes.

AC	k_d (min g/mg)	C (mg/g)	R^2
62–88 μm	31.2	13.2	0.94
177–250 μm	20.9	–3.93	0.99
510–700 μm	7.62	–6.68	0.98
SMC	k_d (min g/mg)	C (mg/g)	R^2
62–88 μm	15.0	29.6	0.86
177–250 μm	13.5	6.10	0.97
510–700 μm	8.33	2.60	0.99

4.4 Conclusions

Commercial activated carbon and synthesized hard and soft templated mesoporous carbons were fully characterized and tested for their BPA adsorption capacity and kinetics. Both mesoporous materials showed a well-ordered 2D hexagonal structure, SMC consists of cylindrical pores with a size of 7.0 nm while CMK-3 has an interconnected nanorod structure with an average pore size of 4.0 nm. The observed maximum adsorption capacity increased with the specific surface area of the material, CMK-3 showed a very high adsorption capacity of 474 mg/g, and outperforms AC with an adsorption capacity of 290 mg/g. When calculating the number of molecules adsorbed per nm², both mesoporous materials, i.e. SMC and CMK-3, performed better than AC. This difference was attributed to the more hydrophobic nature of SMC and CMK-3 compared to AC.

The adsorption kinetics showed a clear advantage of mesoporous materials over AC. The BPA removal rate of CMK-3 was fastest followed by SMC and AC. For both SMC and AC the increase in particle size resulted in a slower BPA removal, which shows that the adsorption is controlled by intraparticle diffusion, although this effect was more pronounced for AC than SMC. In conclusion, mesoporous carbons are promising adsorbents for the removal of BPA, especially CMK-3 with its interconnected nanorod structure and high specific surface area resulting in the highest removal rate as well as adsorption capacity.

Tunable Large Pore Mesoporous Carbons for the Enhanced Adsorption of Humic Acid 5

Submitted as Libbrecht, W., Verberckmoes, A., Thybaut, J., Van Der Voort, P., De Clercq, J. (2016). Tunable Large Pore Mesoporous Carbons for the Enhanced Adsorption of Humic Acid. *Microporous and Mesoporous Materials*.

In this chapter a new way to synthesize large pore mesoporous carbon via the acid catalyzed EISA synthesis was investigated. The introduction of large pores could allow the successful removal of larger adsorbate types from water. The ability of soft templated mesoporous carbons to remove humic acid (HA) was evaluated. Both equilibrium as well as kinetic studies were performed with soft templated mesoporous and activated carbon.

5.1 Introduction

Mesoporous carbons have been studied extensively because of their wide variety of applications [12, 21, 72, 77, 88, 116, 117]. This variety comes from the ability to control material characteristics such as specific surface area, pore volume, pore size and morphology. The pore size control is a challenge within mesoporous carbon synthesis. In soft templated synthesis the choice of surfactant is most crucial to determine the pore size as described in Chapter 1.

Large mesoporous carbons find their applications as support for nanoparticles, catalysts and as adsorbents for larger molecules e.g. enzymes, bulky dyes or humic acid (HA) [24, 25, 41, 155]. HA adsorption was selected in this study. HA is a mixture of organic molecules (MW of 350-50000 g/mol) and is undesirable in the production of drinking water. HA reacts with Cl_2 , a popular disinfectant, to form trichloroalkanes which are carcinogenic [107, 108]. HA can be

removed via different mechanism, including anionic exchange resins, coagulation, membrane filtration or advanced oxidation processes. The two main HA adsorption mechanisms are based on electrostatic or hydrophobic interaction. The electrostatic interactions are observed between the negatively charged functional groups of HA, e.g., carboxyl, carbonyl and hydroxyl groups, and the positive charges of, e.g., soil minerals [111] or aminopropyl-functionalized SBA-materials [99]. SBA-15 itself is not suited for HA adsorption, but the introduction of 1.8 mmol/g aminopropyl functionalities increased the maximum adsorption capacity to 117.6 mg/g, which is considerably better than activated carbon (AC) with 52.4 mg/g [99]. Hydrophobic interactions through π - π -stacking are observed between the carbon adsorbents surface and the hydrophobic moieties (aromatic domains) of HA [24,109,155]. Activated carbons possess the right type of surface to interact with HA, but the small pores often prohibit a sufficient adsorption capacity. Liu et al. investigated the HA adsorption by covalent triazine frameworks (CTF). By changing the monomer from 1,4-dicyanobenzene to 4,4-biphenyldicarbonitrile, the CTF pore size was increased resulting in CTF-1 and CTF_{DCBP} respectively. The microporous CTF-1 (< 2 nm) showed almost no HA adsorption in contrast to the mesoporous CTF_{DCBP} with pores up to 14 nm which had an adsorption capacity of 140 mg/g [156]. The same size exclusion effect was observed with AC with a pore size of around 0.5 nm [24] in comparison to hard template mesoporous carbon CMK-3 with a pore size of 3.7 nm, which was able to adsorb the larger HA molecules.

In this study, the effect of carbon precursor to F127 surfactant (p/s) ratio and carbonization temperature on the mesoporous carbon material characteristics and HA adsorption was investigated. By fine-tuning the p/s ratio, mesoporous carbons with a high degree of control in both pore volume as well as pore size can be synthesized. To our knowledge mesoporous carbons with an average pore size of 50 nm and a broad pore size distribution with pores up to 80 nm have not yet been synthesized by using the commercial F127 surfactant.

5.2 Materials and methods

Mesoporous carbon synthesis

An acid catalyzed EISA soft templated mesoporous carbon synthesis method was used. 2.2 g resorcinol ($\geq 99\%$, Sigma Aldrich) and varying amounts of F127 (Sigma Aldrich, 2.65 g - 4.4g - 8.8 g), resulting in p/s mass ratios of 0.83, 0.5 and 0.25, were selected and mixed with 9 mL ethanol ($\geq 99.8\%$ purity, VWR) and 9 mL HCl (3M) and stirred for 15 minutes at room temperature in a closed reactor. Then, 2.6 g formaldehyde (Formalin 37 wt% in

water) was slowly added and the solution was stirred again for 15 minutes in a closed reactor. The solution was subsequently poured into a large petri-dish to evaporate the ethanol at room temperature for 6 h. Next, the film was scraped from the petri-dish and put into a Nabertherm muffle oven for curing at 60 °C for 12 h. The cured resin was calcined and carbonized under N₂-flow in a Nabertherm tube furnace. In a first heating step of 1 °C/min to 350 °C for 2 h, the surfactant was removed. A second heating step of 2 °C/min to carbonization temperatures of 400 °C, 800 °C or 1200 °C was performed and the temperature was subsequently kept constant for 3 h. The carbon monolith was then crushed and sieved through a 150 mesh filter. Samples were named SMC-x-y, where x and y represent the carbonization temperature and p/s ratio respectively.

5.2.1 Adsorption Tests

To dissolve HA (99+% purity, Sigma Aldrich) in water, the pH was increased by adding 0.1M NaOH solution to a pH of 12 and the HA solution was placed in an ultrasonic bath for 30min. Next, the pH was decreased to 7 by addition of 0.1M HCl. The HA-concentration in solution after adsorption was determined by filtering the mixture through a 0.45 µm PET syringe filter and analyzing the HA-concentration of the filtrate with a Thermo scientific Evolution 60 UV/VIS spectrophotometer at a wavelength of 254 nm.

The adsorption capacity of all synthesized adsorbents was determined by adding 10 mg adsorbent to 50 mL HA-solution with a concentration of 500 mg/L. Samples were placed in a thermostatic shaking device, Infors HT, multitron standard, for 7 days at 25 °C and stirred at 200 rpm. The remaining HA-concentration after adsorption experiment was measured to determine the amount retained on the adsorbent. All adsorption experiments were performed in triplicate. To investigate the relationship between the material characteristics and the adsorption capacity, a stepwise regression analysis was performed to select the significant parameters. Single, interaction and quadratic effects were investigated. The significance of each effect is tested based on the H₀ hypothesis which assumes that a given effect is not significant. Assessment of effect significance is done based on its p-value, the probability for falsely rejecting the H₀ hypothesis: an effect is considered to be significant when $p < 0.05$.

Adsorption kinetics were measured by adding 100 mg adsorbent to 500 mL of 40 mg/L HA-solution. Both AC (Desotec, Belgium) and SMC-800-0.25 were used. The experiments were carried out at room temperature (RT) and the mixture was stirred at 700 rpm. Samples were taken at different time intervals and analyzed. The adsorption capacity at time t (q_t) was calculated according to Equation 5.1 with C_0 and C_t the initial HA-concentration and the

5. TUNABLE LARGE PORE MESOPOROUS CARBONS FOR THE ENHANCED ADSORPTION OF HUMIC ACID

HA-concentration at time t (mg/L), m the adsorbent mass (g) and V the solution volume (L). The experimental data were fitted with the pseudo-second order and the Weber-Morris model (Equation 4.6).

$$q_t = \frac{(C_0 - C_t)V}{m} \quad (5.1)$$

Adsorption isotherm experiments were performed by adding 10 mg adsorbent to 100 mL HA-solutions ranging from 5 to 1000 mg/L. Subsequently, these mixtures were placed in a thermostatic shaking device, Infors HT, multi-tron standard, for 7 days at 25 °C and stirred at 200 rpm to reach equilibrium. The adsorption capacity at equilibrium (q_e) was calculated according to Equation 1, with C_t replaced by the equilibrium HA-concentration C_e (mg/L). The experimental data were fitted with the Langmuir and Freundlich model.

Molecular size distributions of a 80 mg/L HA-solution before and after adsorption with AC and SMC-800-0.25, were analyzed via liquid chromatography organic carbon detection (LC-OCD). The adsorption conditions were 50 mL HA-solution and 50 mg adsorbent at 25 °C and 200 rpm for 7 days. The effect of different initial pH values on the adsorption capacity of SMC-800-0.25 was investigated. 10 mg SMC-800-0.25 was added to 50 mL of HA-solution (40 mg/L) for 7 days at 25 °C and 200 rpm with initial pH values of 3, 5, 7, 9 and 11. The experiment was performed in triplicate.

5.3 Results and Discussion

5.3.1 Effect of p/s ratio on material characteristics

Nitrogen sorption measurements (Figure 5.1) show a type IV isotherm with H1 hysteresis for the SMC-800-y materials indicating mesoporous materials. The narrow hysteresis for all isotherms indicates that the pores are easily accessible and there is no pore blocking, ink-bottle pores or cage like pores. For AC, a type I isotherm indicates the presence of predominantly micropores. Lowering the p/s ratio shifts the hysteresis to a higher value of p/p_0 , indicating an increase in pore size as seen in Figure 5.1. Together with an increasing average pore size, an extensive broadening of the pore size distribution is observed. This broadening could be attributed to the destabilization of the mesostructure. An increase in pore volume can be explained by a change in the modified packing parameter. This parameter has been used to describe the surfactant organization in the self-assembly arrays and to predict the resultant mesostructures. Lower p/s ratios lead to a large modified packing parameter which creates a 3D pore network [44,47]. At low p/s ratios the low amount of carbon precursor will not form 2D hexagonal walls around each micelle, and the change in interfacial curvature will shift the 2D hexagonal structures to 3D porous networks with higher pore volumes [50,51]. In case of SMC-800-0.25 this creates a broad-range mesoporous material with additional macropores up to 80 nm. The average pore size for SMC-800-0.83, -0.5 and -0.25 were respectively 6.2, 23.7 and 43.8 nm as shown in Figure 5.1 and observed via SEM (Figure 5.2). SMC-800-0.83 shows a narrow pore size distribution typical for a 2D hexagonal ordered mesoporous carbon. Decreasing the p/s ratio to 0.5 resulted in a profound broadening of the pore size distribution ranging from 4 to 40 nm. A decrease to 0.25 further increased this effect creating a material with a broad pore size distribution with a pore size range from 4 to 80 nm. This means that the lowest p/s ratio (0.25) was able to create a porous carbon with accessible micro-, meso- and macropores.

The specific surface area of SMC-800-0.83, 0.50 and 0.25 were respectively 670, 663 and 534 m^2/g (Table 5.1). No clear effect of p/s ratio or carbonization temperature was observed on the specific surface area which varies between 422 m^2/g and 670 m^2/g as seen in Table 5.1. The specific surface area of AC was 1027 m^2/g which is higher than for the mesoporous carbons. The mesoporous volume follows the same trend as the pore size and increases by decreasing the p/s ratio as seen in Figure 5.1 and Table 5.1. The pore volume almost doubles from 0.74 cm^3/g to 1.37 cm^3/g for SMC-800-y by decreasing the p/s ratio from 0.83 to 0.25. The extra pore volume is created by a change in the mesoporous volume whilst the microporous volume remains almost constant.

5. TUNABLE LARGE PORE MESOPOROUS CARBONS FOR THE ENHANCED ADSORPTION OF HUMIC ACID

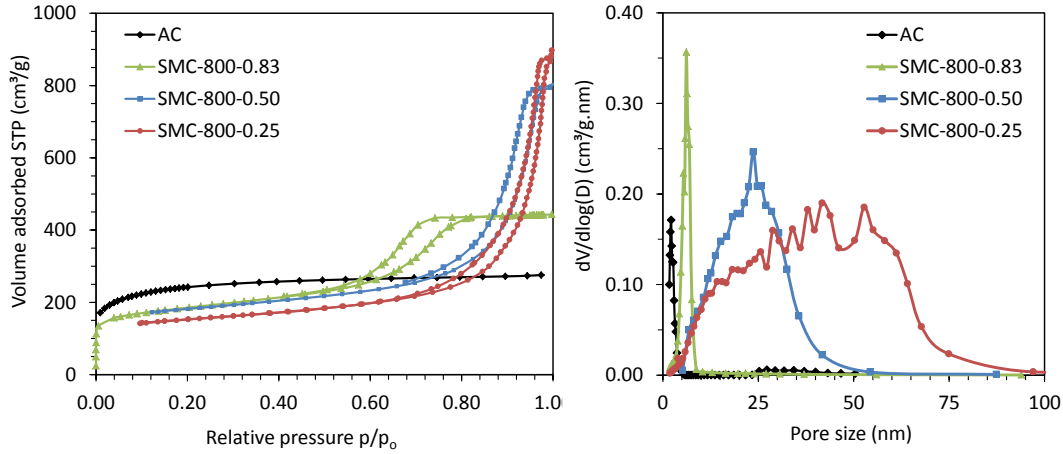


FIGURE 5.1: Nitrogen sorption isotherms (left) and PSD (right) of AC and SMC-800-y materials.

The ordered 2D hexagonal structure of SMC-800-0.83 was validated by TEM (Figure 5.2). XRD patterns of SMC-1200-y are shown in Figure 5.3, the large (100) peak is visible for all three materials indicating mesoporosity. No higher order diffraction peaks are visible due to the broad pore size distributions. The (100) peak of SMC-1200-0.25 appears at a lower angle than for SMC-1200-0.5, and SMC-1200-0.83 has the highest angle. The angle is correlated to the cell parameter and pore size of the material. Higher angles are the result of a smaller pore size.

Table 5.1: Material characteristics of AC and SMC-x-y materials.

Material	S_{BET} (m^2/g)	V_{tot} (cm^3/g)	V_{meso} (cm^3/g)	V_{micro} (cm^3/g)	D_p BJH (nm)	C (wt%)	H (wt%)	N (wt%)	O (wt%)
AC	1027	0.50	-	-	2.3	86.1	0.3	4.5	9.1
SMC-400-0.83	506	0.74	0.69	0.05	7.0	76.6	3.3	1.5	18.7
SMC-400-0.50	550	1.36	1.28	0.08	29.4	76.6	3.7	1.7	18.1
SMC-400-0.25	558	1.56	1.48	0.08	40.0	82.3	3.9	0.0	13.8
SMC-800-0.83	670	0.74	0.60	0.14	6.2	90.5	1.3	1.2	7.0
SMC-800-0.50	663	1.26	1.09	0.17	23.7	95.2	0.5	1.5	2.8
SMC-800-0.25	534	1.37	1.24	0.13	43.8	91.9	0.5	1.8	5.8
SMC-1200-0.83	631	0.79	0.67	0.12	6.0	92.2	0.3	1.1	6.4
SMC-1200-0.50	454	1.08	1.00	0.08	21.5	95.3	0.1	2.3	2.4
SMC-1200-0.25	422	1.31	1.23	0.08	39.9	93.3	0.3	2.2	4.2

5. TUNABLE LARGE PORE MESOPOROUS CARBONS FOR THE ENHANCED ADSORPTION OF HUMIC ACID

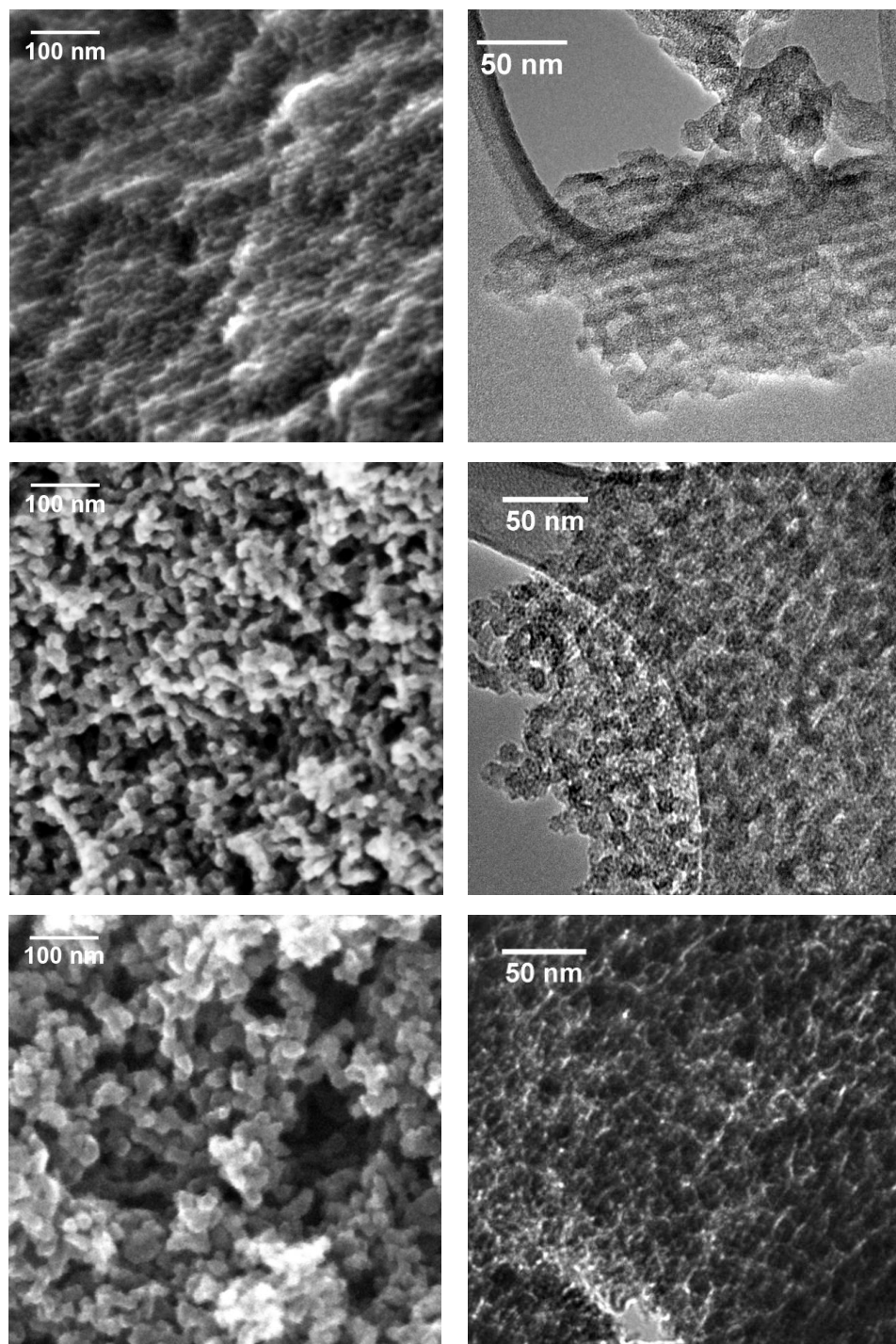


FIGURE 5.2: SEM pictures (left) and TEM pictures (right) of SMC-800-0.83 (top) -0.50 (centre) -0.25 (bottom).

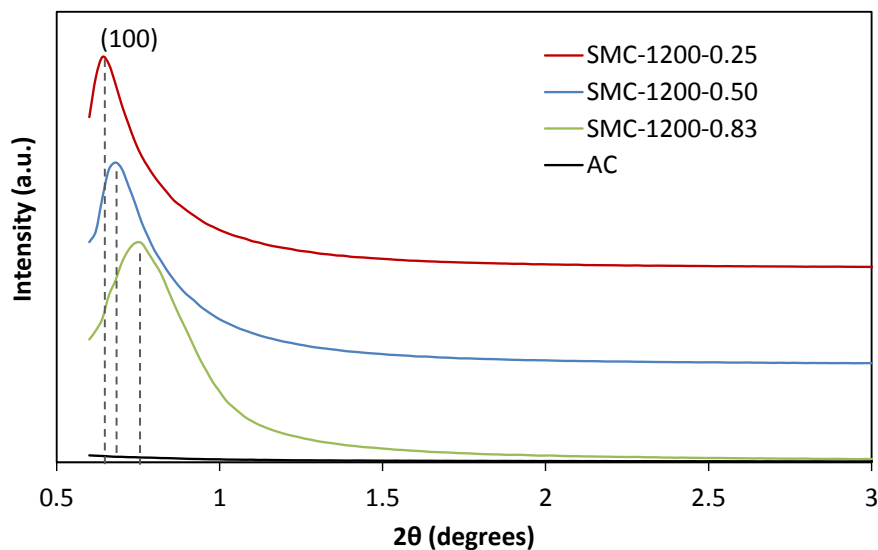


FIGURE 5.3: Powder X-ray diffraction patterns for AC and SMC-1200-y materials.

5.3.2 Effect of carbonization temperature on material characteristics

The effect of carbonization temperature was investigated for the different p/s ratios. At 400 °C a mesoporous polymer material is formed and the transformation to a carbon material is not yet complete. SMC-400-y materials show a distinct brown color instead of the black carbon of SMC-800-y and SMC-1200-y. By examining the elemental composition in Table 5.1, a difference in wt% C is observed between the mesoporous polymers and carbons. The wt% C increases with carbonization temperature. However the difference between 400 °C and 800 °C, going from 77 wt% C to more than 90 wt% C, is more noticeable than the effect from 800 °C to 1200 °C (between 92-95 wt% C). This increase in wt% C is accompanied with a decrease in wt% O. The high temperatures under inert atmosphere remove oxygen containing functional groups such as hydroxyl and carboxyl groups. This increases the hydrophobicity of the material, which in turn is expected to impact on its adsorption capabilities [7, 43].

The temperature effect on the structural properties was investigated with nitrogen sorption in Figure 5.4. For the SMC-x-0.83 materials, some shrinkage could be observed when transforming from a polymer network to the carbon framework reducing the pore size with almost 1 nm. For the 0.5 ratio and

5. TUNABLE LARGE PORE MESOPOROUS CARBONS FOR THE ENHANCED ADSORPTION OF HUMIC ACID

0.25 ratio, the mesoporous volume also decreased with increasing carbonization temperature. The difference in pore size between 800 °C and 1200 °C is minimal as seen from the pore size distribution in Figure 5.4. Shrinkage of mesoporous polymers has been reported to start at temperatures exceeding 400 °C and can range from 1 up to 5 nm depending on the stability of the carbon framework [22, 65, 66, 157]. An increased carbonization temperature also induced a pore volume loss from respectively 1.48 cm³/g to 1.23 cm³/g (Table 5.1).

In conclusion, for all p/s ratios a carbonization at 800 °C gave good material characteristics such as high pore volume, and broad pore size distribution and a wt% C above 90%. Carbonization at a temperature of 1200 °C did not profoundly enhance the material characteristics. Therefore, the in-depth HA adsorption study was performed with SMC-800-0.25.

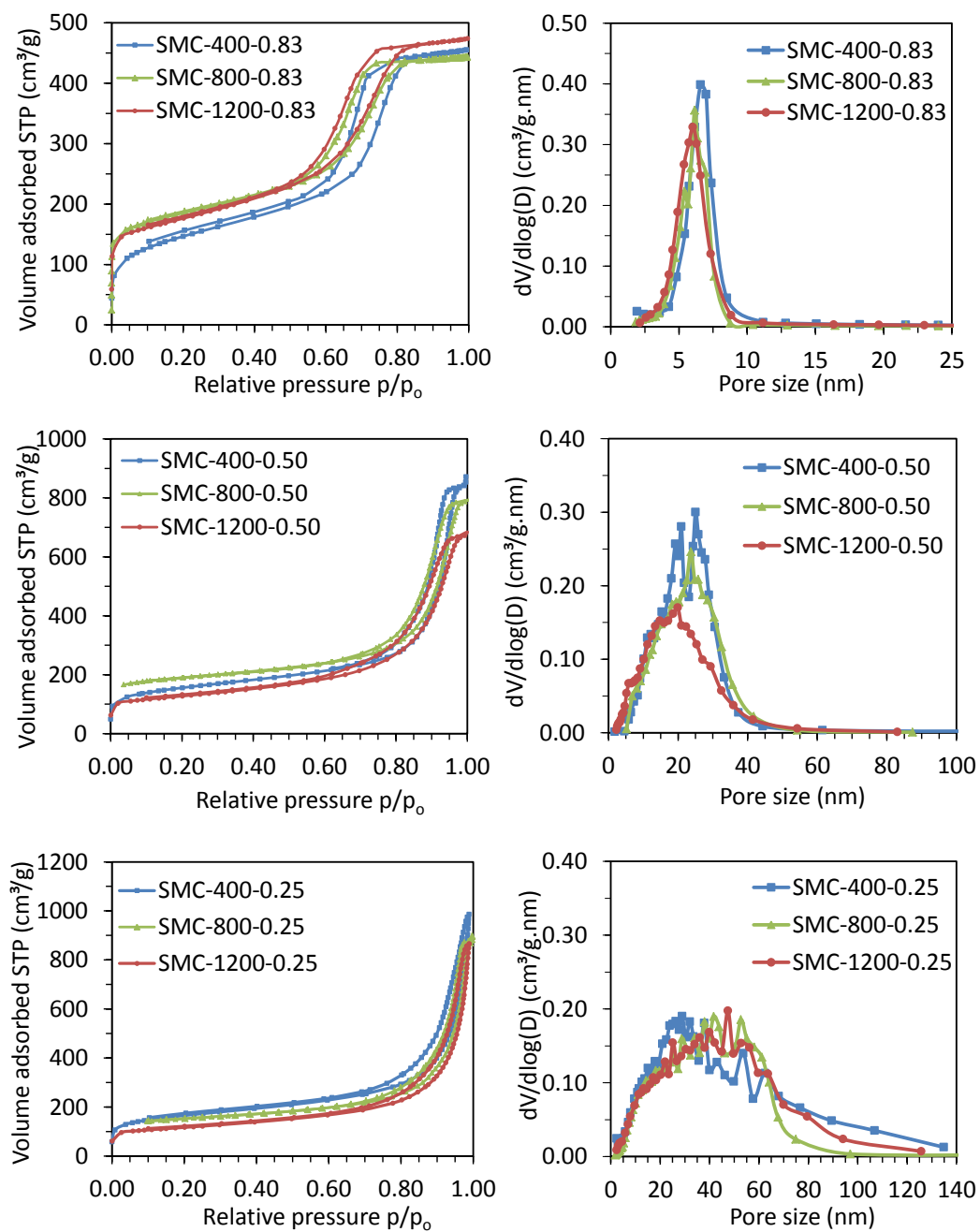


FIGURE 5.4: Nitrogen sorption isotherms for all SMC-x-y materials (left) and PSD (right).

5.3.3 Humic acid adsorption

Adsorption capacity of all SMC-x-y materials

The potential use of SMC-x-y materials as adsorbents for the large humic acid (HA) was investigated. The adsorption experiments were performed at neutral pH values, which is typical for water purification plants. The adsorption capacities at initial concentrations of 500 mg/L HA are shown in Table 5.2. They increased with a decrease in p/s ratio. The carbons with large pores, broad pore size distribution and large pore volume were significantly better at adsorbing HA. This trend was observed regardless of the carbonization temperature, the 0.25 ratio always adsorbed more HA than the other ratios. For a carbonization temperature of 800 °C, adsorption capacities for the ratios 0.83, 0.5 and 0.25 were respectively 260, 294 and 352 mg/g. The effect of carbonization temperature is most pronounced between 400 °C and 800 °C which increased the adsorption capacity from 155 to 260 mg/g for the 0.83 ratio; from 221 to 294 mg/g for the 0.5 ratio; and from 250 to 352 mg/g for the 0.25 ratio. The more hydrophobic carbon is beneficial for the interaction between the adsorbent surface and HA. This supports the idea that most adsorption will occur via π - π -stacking of the aromatic rings of HA with the carbon surface at neutral pH conditions.

Table 5.2: Experimental and predicted (Equation 5.2) adsorption capacities (10 mg adsorbent in 50 mL of 500 mg/L HA-solution, RT, 200 rpm, pH = 7), together with the significant material characteristics pore size D_p and wt% C.

Material	D_p (nm)	wt% C (%)	$q_{e,exp}$ (mg/g)	$q_{e,pred}$ (mg/g)
AC	2.3	86	189 ± 17.2	209
SMC-400-0.83	7.0	77	155 ± 2.0	160
SMC 400-0.5	29.4	77	221 ± 20.1	209
SMC-400-0.25	40.0	82	261 ± 1.3	266
SMC-800-0.83	6.2	90	260 ± 10.6	244
SMC-800-0.5	23.7	95	294 ± 16.6	316
SMC-800-0.25	43.8	92	352 ± 19.8	341
SMC-1200-0.83	6.0	92	275 ± 0.5	257
SMC-1200-0.5	21.5	94	312 ± 12.8	305
SMC-1200-0.25	39.9	93	332 ± 0.5	339

The significant material characteristics were investigated by constructing a model via stepwise regression. The specific surface area, micro and mesoporous volume, pore size and wt% C were selected as factors. Only the pore size and wt% C were significant factors with $p < 0.05$. With these factors, a model (Equation 5.2) was constructed with an R^2 of 0.95 that is able to predict the experimental adsorption capacities, as shown in Table 5.2. The adsorption capacity of HA on these mesoporous carbons can be predicted via Equation 5.2 in which only the average pore size and wt% C contribute to an increased adsorption capacity. An increase in pore size or wt% C will have a beneficial effect on the adsorption capacity.

$$q_e = -365 + 2.22D_p + 6.60wt\%C \quad (5.2)$$

5.3.4 Adsorption kinetics of SMC-800-0.25 and AC

The experimental HA adsorption kinetics of SMC-800-0.25 and AC are shown in Figure 5.5. Because the pseudo-second order kinetic model has been used frequently to describe HA adsorption kinetics [99,109,156,158,159], this model was fitted to the experimental data (Figure 5.5). The pseudo-second order fit had an R^2 of 0.904 for AC and 0.925 for SMC. The higher k_2q_e value of SMC-800-0.25 versus AC clearly showed a faster HA adsorption on SMC-800-0.25. The presence of large mesopores clearly increases the HA adsorption rate. The Weber-Morris model was investigated as well to identify intraparticle diffusion effects [112,160]. As seen in Figure 5.5, the Weber-Morris plot shows multilinearity. The first linear part is typically related to diffusion into macro- and mesopores, the diffusion coefficient of this part $k_{d,1}$ is larger for SMC-800-0.25 than for AC as seen in Table 5.3 [99,109]. When observing the second linear part, typically attributed to diffusion in micropores, the diffusion coefficients ($k_{d,2}$) of both AC and SMC-800-0.25 are almost equal. Both plots do not intersect at zero, which is an indication that boundary-layer diffusion still plays a role [109]. The HA adsorption kinetics are therefore influenced by three effects: the boundary layer diffusion, the diffusion in meso- and macropores, which is faster for the SMC-800-0.25 with large mesopores compared to AC, and the micropore diffusion which is the same for both materials.

Table 5.3: Kinetic parameters for pseudo-second order and Weber-Morris model for SMC-800-0.25 and AC.

Material	Pseudo-second order			Weber-Morris			Morris		
	k_2 g/(mg min)	q_e (mg/g)	R^2	$k_{d,1}$ mg/(g min ^{1/2})	C_1 (mg/g)	R^2	$k_{d,2}$ mg/(g min ^{1/2})	C_2 (mg/g)	R^2
AC	0.000207	20.6	0.90	0.312	5.63	0.98	1.02	12.4	0.98
SMC-800-0.25	0.000227	27.3	0.93	0.620	5.79	0.98	0.917	19.8	0.94

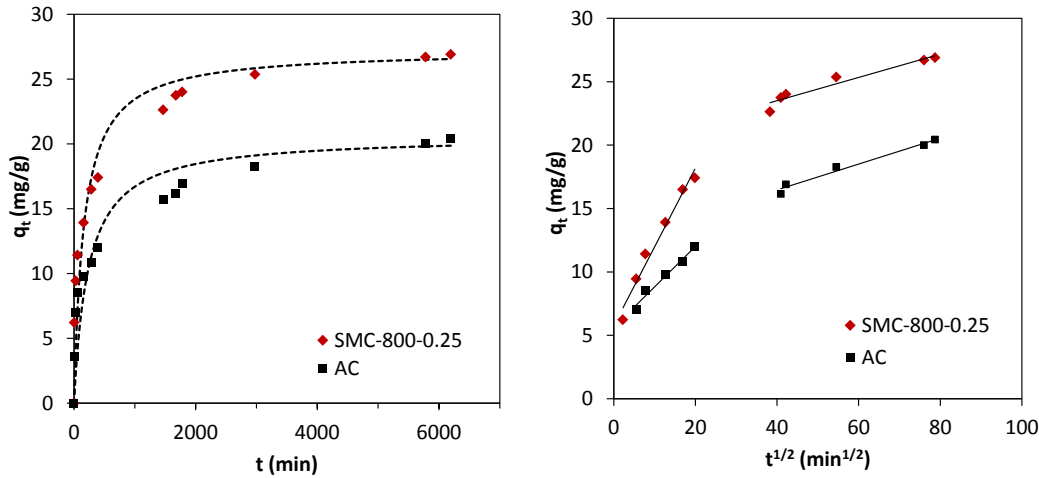


FIGURE 5.5: Adsorption kinetics of 50 mg SMC-800-025 and AC in 500 mL 40 mg/L HA-solution at RT, 700 rpm and pH of 7. The pseudo-second order model (left) and the Weber-Morris model (right) were fitted to the data.

5.3.5 Adsorption isotherms of SMC-800-y and AC

Both mesoporous carbons with larger pores, SMC-800-0.5 and -0.25, were selected for further HA adsorption tests. Their experimental adsorption isotherms are shown in Figure 5.6. The studied AC reaches an adsorption capacity of 200 mg/g, which is quite high compared to other reported AC [109,159,161]. However, the mesoporous carbons performed much better with an adsorption capacity of 364 mg/g and 420 mg/g for SMC-800-0.5 and -0.25 respectively. Moreover, the conclusion that the pore size affected the HA adsorption, is validated by the adsorption isotherms: as the average pore size increases from AC over SMC-800-0.5 to SMC-800-0.25 (Table 5.2), the adsorption capacities increase as well. The larger mesopores of SMC-800-0.25 are able to adsorb more HA than the smaller mesopores of SMC-800-0.5. HA adsorption isotherms are often described by the Langmuir and Freundlich equations [99,111,159]. Both Freundlich and Langmuir fit the data quite well (Table 5.4). The Langmuir fit is slightly better. Given the large size of HA molecules, the adsorption will probably be limited to a monolayer. The q_{max} of the fitted Langmuir isotherms are 236, 470 and 540 mg/g for respectively AC, SMC-800-0.5 and -0.25, which indicates the advantage of a larger pore size on the adsorption of HA. The zeta potential for AC, SMC-800-0.50 and SMC-800-0.25 was studied at pH 7 and were respectively -27.1, -20.3 and -20.9 mV (Figure 5.7). Electrostatic repulsions between charged HA molecules and the negatively charged surface will have a negative effect on the adsorption capacity.

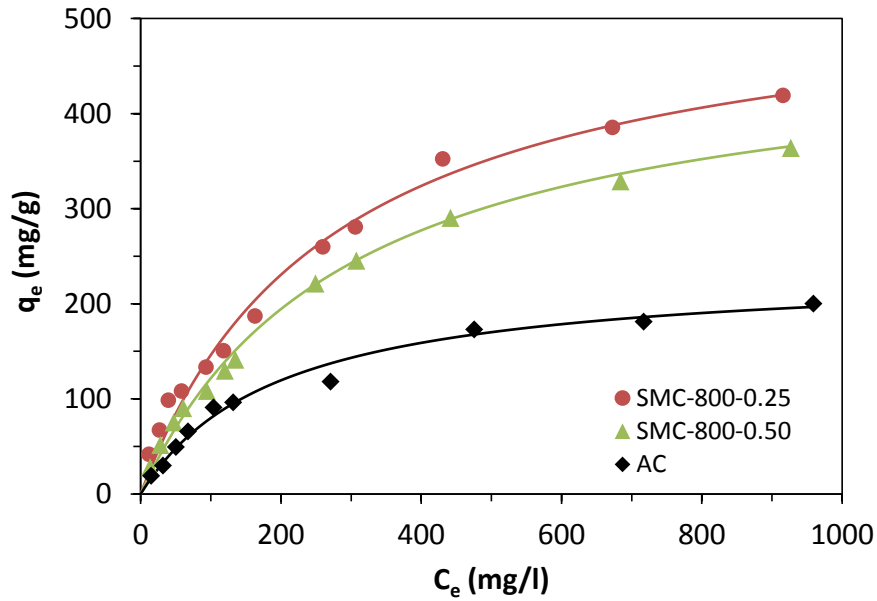


FIGURE 5.6: Adsorption isotherms of SMC-800-0.25, SMC-800-0.5 and AC with Langmuir fit, 10 mg of adsorbent was added to 50 mL HA-solution of various concentrations at 25 °C, 200 rpm for 7 days.

Table 5.4: Langmuir and Freundlich parameters for SMC-800-0.25, SMC-800-0.5 and AC.

Material	Langmuir			Freundlich		
	K_L (L/mg)	q_{max} (mg/g)	R^2	K_F ((mgL ^{1/2})/(mg ^{1/2} g))	1/n	R^2
AC	0.00440	236	0.986	9.64	0.451	0.968
SMC-800-0.25	0.00370	540	0.985	15.9	0.490	0.978
SMC-800-0.5	0.00340	470	0.996	12.2	0.509	0.973

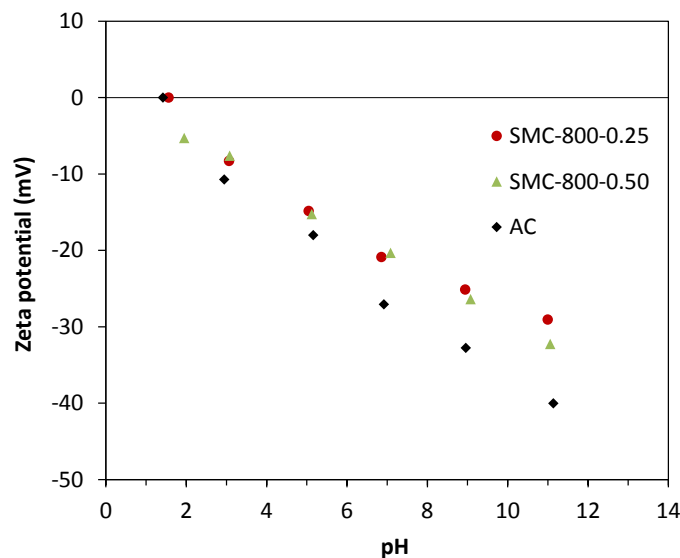


FIGURE 5.7: Zeta potential measurements at varying pH of AC, SMC-800-0.50 and SMC-800-0.25.

5.3.6 Influence of the pH

The wt% C of the mesoporous carbons significantly affected the adsorption capacity, as shown in Equation 5.2. This was explained by the hydrophobic interactions between HA and the adsorbent being the main adsorption interaction. To confirm the hydrophobic adsorption interaction, the effect of pH on the HA adsorption on SMC-800-0.25 was studied at different initial pH values (3, 5, 7, 9 and 11). As seen in Figure 5.8, the HA adsorption increases dramatically at lower pH values. At low pH, the electrostatic repulsions between HA and the carbon surface decrease because the carboxyl and phenolic hydroxyl groups of HA are protonated [162]. The zeta potential SMC-800-0.25 goes up when the pH is lower (Fig. 5.7). The carbon surface will then be less negatively charged. This allows more hydrophobic interactions to occur and, hence, increases the adsorption [24]. Upon a pH increase, the carboxyl groups deprotonate first (pKa5) and at higher pH values the phenolic hydroxyl groups (pKa10) deprotonate as well. This makes HA more hydrophilic, causes electrostatic repulsion with the hydrophobic carbon surface and, hence, decreases the adsorption [110–112]. To achieve the highest adsorption capacity with these mesoporous carbons, working at low pH (<4) is recommended. Although at a neutral pH, there are still enough hydrophobic interactions to remove HA efficiently.

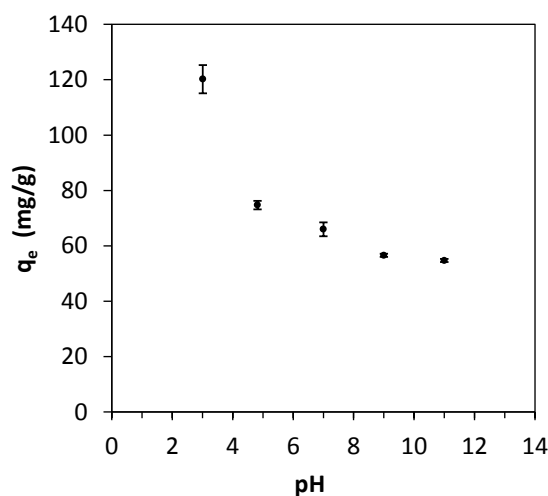


FIGURE 5.8: Influence of initial pH on the adsorption capacity of 10 mg SMC-800-0.25 in 50 mL HA-solution (40 mg/L) for 7 days at 25 °C and 200 rpm.

5.3.7 Molecular weight distribution of HA

The importance of the adsorbent pore size for the removal of HA is further elucidated by analyzing the molecular weight distributions of HA before and after adsorption on SMC-800-0.25 and AC via LC-OCD, see Figure 5.9. The MW-distribution of HA shows a dual distribution indicating two different sizes of HA [24, 115]. The peaks at 40 and 53 min correlate with HA molecules with very different number molecular weights (M_n) of respectively above 1000 g/mol and around 350 g/mol. As expected the entire chromatogram is lower for SMC-800-0.25 compared to AC. This indicates that the mesoporous carbon is able to adsorb more HA of each molecular size. This is attributed to the pore structure of SMC-800-0.25 shown in Figure 5.2, containing micro-, meso- and macropores. Between 30 and 38 min, the largest molecules are detected and the size exclusion effect of AC becomes visible because the AC curve coincides with the original HA curve and therefore, no adsorption occurred for the larger molecules. On the other hand, the SMC curve is lower compared to the HA curve and therefore able to adsorb the largest HA molecules. This clearly demonstrates the importance of the pore size in the adsorption of large molecules. The newly synthesized soft templated mesoporous carbons SMC-800-0.25 with large pores and a broad pore size distribution are able to adsorb both smallest and largest HA molecules.

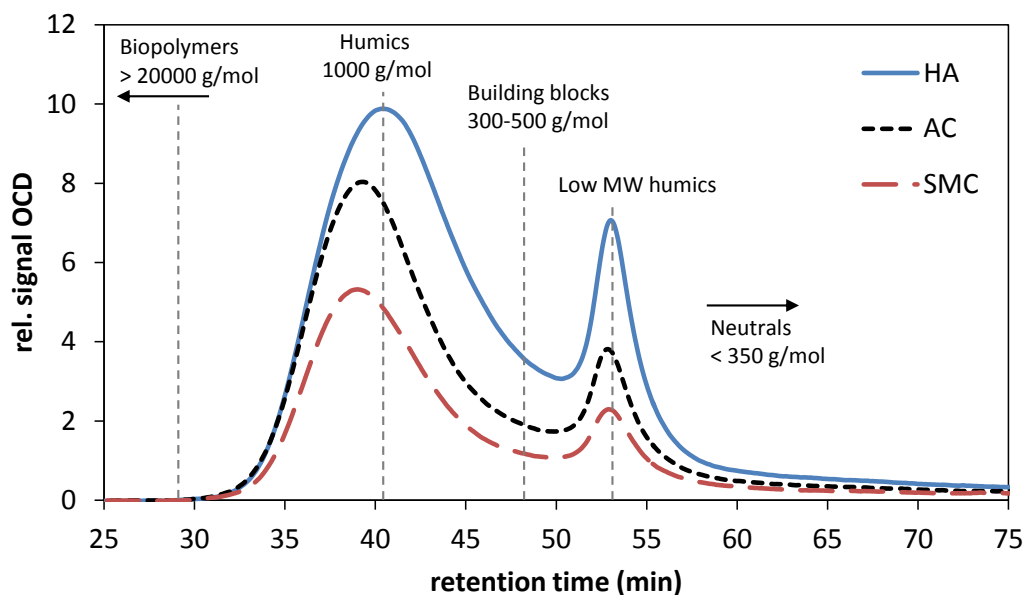


FIGURE 5.9: LC-OCD chromatograms of 50 mL HA-solution (80 mg/L) before (HA, blue line) and after adsorption for 7 days at 25 °C at 200 rpm, with 50 mg adsorbent (AC, short dash and SMC-800-0.25, long dash).

5.4 Conclusions

The well-known organic self-assembly of resorcinol/formaldehyde with F127 was investigated to synthesize large pore mesoporous carbons. By decreasing the p/s ratio, the mesophase changed to a disordered large pore mesopores network and the average pore size increased from the typical 7 nm up to 25 nm and even 50 nm. With increasing pore size, the pore size distribution became broader. With the lowest p/s ratio of 0.25 a porous carbon was synthesized with micro-, meso- and even macropores. The effect of carbonization temperature was most pronounced in the material composition: the wt% C and, hence, hydrophobicity increased with the carbonization temperature. These large pore mesoporous carbons were tested for HA adsorption. The adsorption capacity increased with pore size and wt% C, indicating that both size exclusion effects occur together with a hydrophobic π - π -stacking adsorption mechanism. This hydrophobic interaction mechanism was validated by pH experiments. At low pH (<4) HA becomes protonated which will reduce electrostatic repulsion with the carbon surface and allow more hydrophobic π - π -stacking adsorption interactions to occur. The molecular weight distribution of HA before and af-

ter adsorption showed that the high MW fractions were not adsorbed by AC because of the size exclusion effect. SMC-800-0.25 with the largest average pore size and broad pore size distribution adsorbed HA molecules of all sizes. The mesoporous carbon with the largest pores had a HA adsorption capacity twice that of AC and the presence of large pores also contributed to faster adsorption kinetics compared to AC.

This chapter provides some insights into the synthesis of porous boron nitride (BN). BN has recently shown to be a promising new adsorbent type. A hard template BN synthesis, in which ammonia borane is impregnated into CMK-3 and a template-free BN synthesis in which melamine diborate is transformed into porous BN were investigated. The resulting material characteristics were evaluated and some preliminary adsorption experiments for BPA were performed.

6.1 Introduction

Hexagonal boron nitride (h-BN) is well known for its chemical and thermal stability. Therefore a broad range of applications have been developed, from heavy duty lubricant over cosmetics to thermally stable parts [163, 164]. The interest in BN as porous material and potential adsorbent has been increasing in the last decade [91, 165–171]. The main challenges within the porous BN synthesis are finding suitable precursors, ceramization temperatures or template materials. Porous BN can be obtained via three methods.

A first route is the hard template route, where 3D porous template materials such as silica or carbons are filled with BN-forming precursors. To obtain an efficient filling of the hard template pores, precursors with a high ceramic yield are used such as ammonia borane, borazine, polyborazylene and trimethylaminoborazine (TMAB) [165]. After removal of the hard template a porous BN is obtained that is a negative replica of the parent material. Activated carbon as hard template was mixed with boron trioxide and heated in

N₂ atmosphere at 1580 °C. An intermediate material consisting of boron, nitrogen and carbon was observed. After air treatment at 600 °C, the carbon was removed and a porous BN with a specific surface area amounting to 168 m²/g and a pore diameter of 3.2 nm was obtained [167]. Miele et al. compared the mesoporous hard templates SBA-15 and CMK-3 [172]. The impregnation of TMAB precursor into CMK-3 was more successful than SBA-15, which resulted in better turbostratic (t-BN) material characteristics with a higher specific surface area (500 m²/g versus 140 m²/g for SBA-15) and higher pore volume (0.59 cm³/g versus 0.22 cm³/g for SBA-15) [172]. The t-BN indicates a low crystalline BN structure which is located between amorphous BN and the highly ordered h-BN. Zeolite derived carbons have also been used as a hard template leading to porous amorphous BN with a bimodal pore size distribution, a high pore volume of 0.78 cm³/g and specific surface areas up to 570 m²/g [166].

Although porous BN was successfully obtained through the hard template route, recently a second and third route were developed which were faster and less expensive synthesis methods. The second method is the soft template route where the material is synthesized around micelle-forming surfactants. This method is more challenging compared to the hard template method, as most of the BN ceramization temperatures are higher than the degradation temperature of typical micelle forming polymers e.g. P123, F127. Maleki et al. succeeded in polymerizing ammonia borane (NH₃BH₃) around a tailor made PS-b-PEO surfactant. A heating treatment in ammonia atmosphere to 1150 °C was performed to remove the surfactant and ceramize the polymerized ammonia borane, this introduced large worm-like mesopores of around 20 nm. The material consisted of turbostratic BN (t-BN) and had a specific surface area of 350 m²/g and pore volume of 0.5 cm³/g [170]. Li et al. used the soft template P123 and mixed it with melamine and boric acid. This mixture was calcined at 546 °C for 2 h and then heated at 1300 °C for 8 h in N₂ atmosphere. The porous t-BN had a very high specific surface area of 2078 m²/g and pore volume of 1.66 cm³/g with multimodal microporous/mesoporous structure with three main characteristic pore sizes of 1.3, 2.7 and 3.9 nm [169].

The third method is a template-free route, in the absence of templates. Here, the porosity is introduced by selecting precursors that release gasses: N₂, NH₃, H₂O, CO and CO₂ during ceramization [168, 173]. Lei et al. used boron trioxide and guanidine hydrochloride as boron and nitrogen sources which were heated at 1100 °C for 2 h under 15%H₂/85%N₂ atmosphere [91]. The porous h-BN nanosheets had a large specific surface area of 1427 m²/g and pore volume of 1.09 cm³/g with pore diameter in the range from 20 to 100 nm. The use of boron trioxide and urea in a 1:10 molar ratio and heating to 1000 °C under 5%H₂/95%N₂ flow resulted in an interconnected flexible

network of h-BN nanosheets with a specific surface area amounting to 1156 m²/g, a pore volume of 1.17 cm³/g and micro- and mesopore diameters between 2 and 10 nm [173]. Ammonia borane polymerization has also been used as a precursor for template-free synthesis of porous t-BN. The highest specific surface area and pore volume (542 m²/g and 0.244 cm³/g) were obtained by isothermal heating of ammonia borane at 70 °C for 32 h before being subjected to ceramization at 1300 °C [170]. Melamine diborate crystals with different boric acid to melamine ratios were used as precursor as well [168,174]. Mixtures with ratios of 1:6 and 1:2 were heated at respectively 1100 °C and 1460 °C which resulted in h-BN with a specific surface area of respectively 627 m²/g and 1687 m²/g. This template-free method has the advantage that no template or surfactant is required, making the synthesis faster, cost-effective and more efficient [173,175]. The porosity introduced by the release of gases is disordered in nature [168,176], while hard or soft templating routes lead to more ordered materials [172].

Introducing porosity in BN combines the advantageous intrinsic BN properties such as high thermal stability with interesting adsorbent characteristics such as large surface area and high pore volume [169,175]. Porous BN are becoming a novel adsorbent family and have already been used to adsorb dyes [173,177] and oils [91] from water.

In this chapter, the synthesis of a porous BN will be investigated, both via a hard template route, by impregnating the carbon template CMK-3 with NH₃BH₃, and via a template-free route, with melamine diborate. NH₃BH₃ was selected as precursor for the hard template route because of its high BN yield and easy synthesis via a salt exchange reaction. The synthesis of porous BN via the impregnation of NH₃BH₃ precursor in the hard template CMK-3 has not been reported. For the template-free route, the melamine diborate complex, with its low cost and easy synthesis was evaluated as precursor for h-BN synthesis. The effect of ceramization temperature on the template-free BN material characteristics was investigated. The capabilities of the BN adsorbent for removal of bisphenol A (BPA) from water were also evaluated.

6.2 Experimental

6.2.1 Hard template porous BN synthesis

For the synthesis of ammonia borane (NH₃BH₃), 0.1 mol (3.783g) sodium-borohydride (NaBH₄, purity 98%, Sigma Aldrich) and an excess of 0.1 mol (13.238g) ammonium sulfate ((NH₄)₂SO₄, purity 99%, Sigma Aldrich) were added in 600 ml THF (purity >99%, Sigma Aldrich). The mixture was stirred at 40 °C for 2h. The Na₂SO₄ precipitate was removed via filtration. The

NH_3BH_3 is retrieved via evaporation of the THF in a rotavapor.

The mesoporous BN was synthesized by using the CMK-3 as hard template, CMK-3 was synthesized as described in chapter 4. CMK-3 was impregnated with a 0.05 g/mL ammonia borane in methanol solution (purity 99.8%, Sigma Aldrich). After evaporation of the methanol in a rotavapor, the impregnated CMK-3 was placed in a tube furnace (Nabertherm) at 1400 °C for 12h (2 °C/min) under nitrogen atmosphere for the ceramization of BN. Next, heat treatments in air were performed at different temperatures to remove the carbon template.

6.2.2 Template-free porous boron nitride synthesis

As boron and nitrogen source, boric acid (H_3BO_3 , Sigma-Aldrich, 99+%) and melamine (Sigma-Aldrich, 99%) were used respectively. These precursors were mixed in a molar ratio of 2:1, the 3.71 g boric acid and 3.78 g melamine are dissolved in 500 mL distilled water at 85 °C for 16h in an oil bath. Next, the mixture remains in the oil bath to ensure a slow cooling as melamine diborate crystals begin to form. The precipitate is filtered and dried at 90 °C for 12h.

The ceramization was performed by placing the melamine diborate crystals in a tube furnace (Nabertherm), where the ceramization temperature was varied from 1400 °C to 1700 °C with a heating rate of 2 °C/min under nitrogen atmosphere. The different BN materials were denoted as BN-x, with x the ceramization temperature.

The stability was tested by immersing 0.150 g BN-1700 material in 300 mL of distilled water for 24h at RT while stirring at 200 rpm. The stability at high temperatures in air was tested by placing 0.150 g BN-1700 in a muffle oven and heating at 5 °C/min to 500 °C for 4h and 24h.

6.2.3 Characterization

Diffuse reflectance infrared Fourier transform (DRIFT) spectroscopy is performed in vacuum at 120 °C on a hybrid IR-Raman spectrophotometer, the Nicolet 6700 (Thermo Scientific) with a liquid nitrogen cooled MCT-A detector, using a Graseby Specac diffuse reflectant cell. Commercial h-BN (Sigma Aldrich, 98% purity) was analyzed with XRD and IR as a reference. Raman analysis on the ammonia borane precursor was performed on a RXN1 Raman spectrometer (Kaiser Optical Systems) fitted with a 532 nm laser operating at 40 mW and using an optical probe. TGA measurements were performed on a STA 449 F3 Jupiter (Netzsch) in which 10 mg sample was loaded and heated at 10 °C/min in a nitrogen atmosphere.

6.2.4 Adsorption tests

Adsorption of bisphenol A (BPA, Sigma-Aldrich, >99% purity) was tested by adding 10 mg BN to 100 mL of 60 mg/L BPA solution which was stirred at 200 rpm at 25 °C and different adsorption times: 1h, 4h and 24h. After adsorption, the BPA concentration in solution was determined by filtering the mixture through a 0.45 μm PET syringe filter and analyzing the BPA concentration of the filtrate with a Thermo scientific Evolution 60 UV/VIS spectrophotometer at 275 nm.

6.3 Results and Discussion

6.3.1 Hard templated h-BN

Synthesis of precursor ammonia borane

Ammonia borane is synthesized via a salt-exchange reaction of sodium borohydride (NaBH_3) and ammonium sulfate $(\text{NH}_4)_2\text{SO}_4$ (Equation 6.1). Hydrogen gas is released and sodium sulfate is formed as byproduct. The precursor is made in-house before each impregnation. Raman spectroscopy was performed to check the purity of the ammonia borane by comparing its spectrum with that of pure NH_3BH_3 (Sigma Aldrich, 97% purity). As seen in Figure 6.1, both spectra are practically identical indicating no impurities in the synthesized precursor. The characteristic peaks of NH_3BH_3 are present: (a) symmetrical stretch of NH and BH-functionalities and BH_3 and NH_3 deformation.

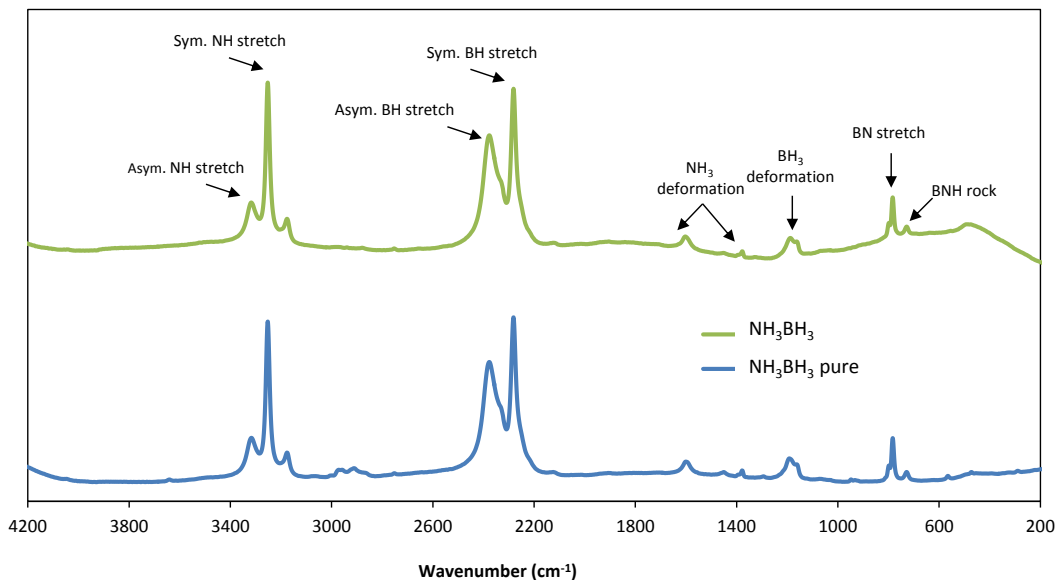


FIGURE 6.1: Raman spectra of synthesized (top) and pure NH_3BH_3 (bottom).

When producing BN from NH_3BH_3 , the starting precursor is already predominantly composed of nitrogen and boron. Therefore, its theoretical yield of

80% will exceed that obtained with other precursors, e.g. guanidine chloride, melaminediborate or almost as high as polyborazylene and trimethylaminoborazylene (80-90%). The actual yield is quantified via TGA of NH_3BH_3 shown in Figure 6.2. A yield of 50% is observed at 1100 °C while the theoretical maximum yield is 80% when only hydrogen gas would be eliminated from the reaction. The extra 30% mass loss is probably due to the formation of borazine gas as seen in Figure 6.3. Perdigon-Melon et al. investigated the ceramic yield of different h-BN precursors and found similar results for ammonia borane with a ceramic yield of 49%, a yield of 55% for trimethylaminoborazine (MAB), 19.4% for trianilino-aminoborazine (AAB) and 25.6% for tribenzylaminoborazine (BAB) [165].

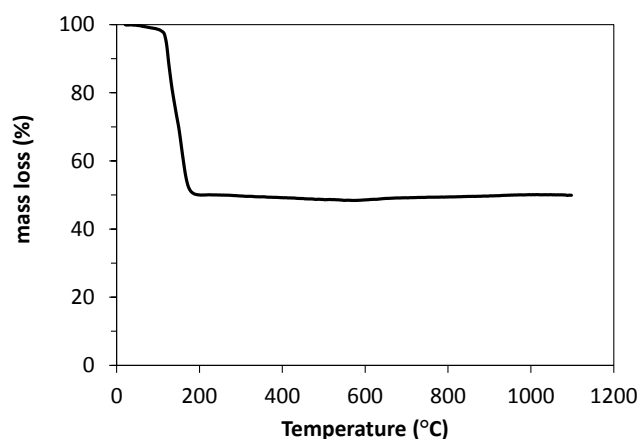


FIGURE 6.2: TGA curve of NH_3BH_3 at 10 °C/min in nitrogen atmosphere.

Figure 6.3 shows the reaction mechanism for NH_3BH_3 as precursor. In the first step polyaminoborane is formed and hydrogen gas is released (3). The polyaminoborane is in equilibrium with its monomer (2). At higher temperatures polyiminoborenes (5) are formed and more H_2 gas is released. A possible side reaction is the formation of borazine (4). At temperatures between 1170 °C and 1500 °C h-BN is formed (6). The formation of h-BN from the synthesized NH_3BH_3 was first evaluated by synthesizing BN from in-house synthesized NH_3BH_3 at 1400 °C for 12h. The obtained white powder with a ceramic yield of 37% was evaluated via XRD and compared to commercial h-BN as seen in Figure 6.4. The characteristic diffraction peaks of BN, the (002), (101) reflections at respectively 26° and 42° indicated hexagonal type BN [175, 179–181]. The following step is to investigate if the transformation from NH_3BH_3 into h-BN can be done inside the porous carbon template.

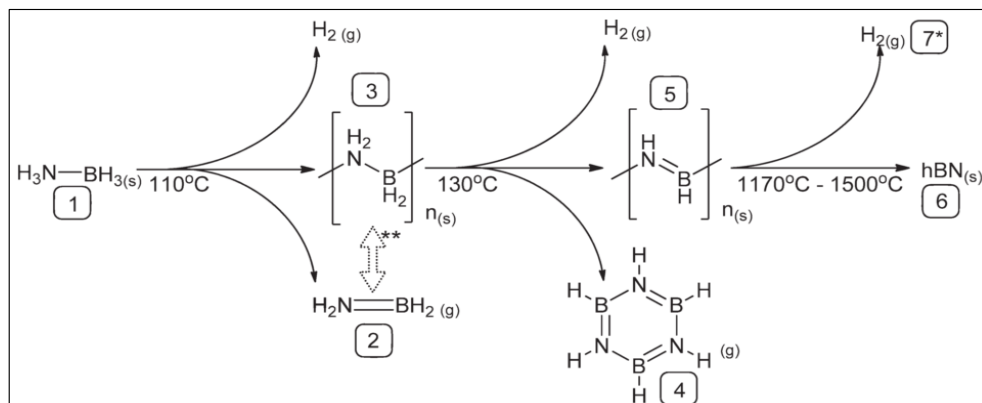


FIGURE 6.3: Reaction mechanism of h-BN from ammonia borane [7*]. Hydrogen abstraction by the evolution of molecular hydrogen at high temperature is assumed. **Reversibility between molecular aminoborane and PAB [178].

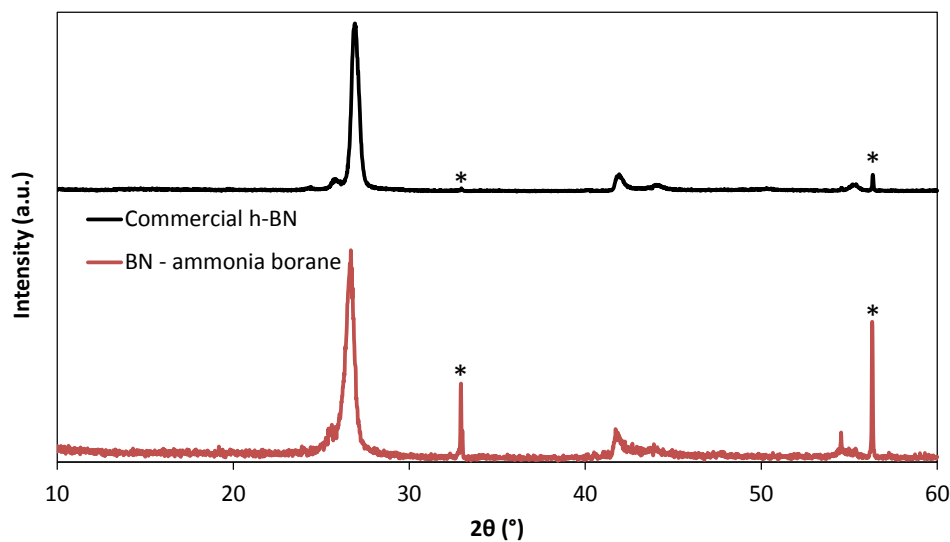


FIGURE 6.4: Powder X-ray diffraction patterns of commercial h-BN and BN from ceramization of pure NH_3BH_3 at 1400°C , * = sample holder peaks.

Impregnation and ceramization of NH_3BH_3 in CMK-3

The next step in the porous BN synthesis is the impregnation of the precursor in the hard template CMK-3. The porosity after impregnation was evaluated with nitrogen sorption of the template material before and after impregnation and ceramization. 1 g of CMK-3 can be impregnated with a theoretical maximum of 0.65 g NH_3BH_3 based on the template pore volume and the precursor density. The mass of the impregnated CMK-3 amounted to 1.54 g, indicating that more than 80% of the template pores were filled. As seen in Figure 6.5 the porosity of the CMK-3 is almost completely gone after impregnation with NH_3BH_3 solution and ceramization of the precursor. The specific surface area of CMK-3 decreases from $1293\text{ m}^2/\text{g}$ to $80\text{ m}^2/\text{g}$ (Table 6.1). This indicates that BN has formed inside the carbon template and filled the pores of CMK-3.

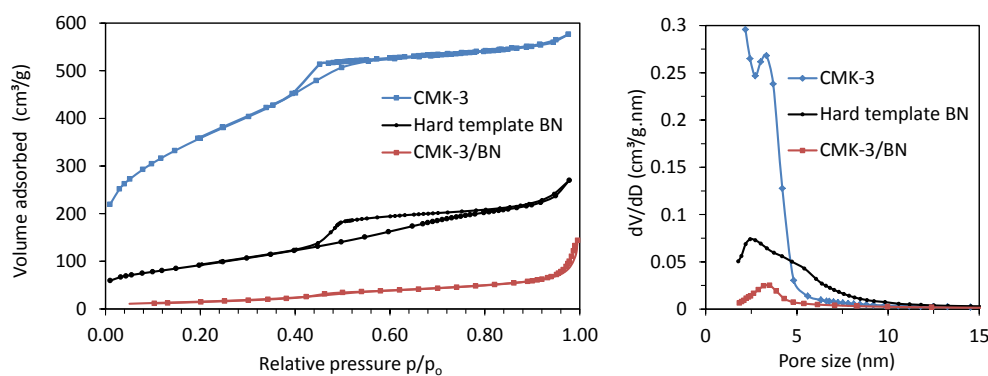


FIGURE 6.5: Nitrogen sorption isotherms of CMK-3, CMK-3/BN and hard template BN-500 °C-air (left) with PSD (right).

Table 6.1: Material characteristics of CMK-3, CMK-3/BN and BN.

Material	S_{BET} (m^2/g)	V_{tot} (cm^3/g)	D_p (nm)
CMK-3	1293	0.87	3.3
CMK-3/BN	80	0.08	3.1
BN-500 °C-air	325	0.37	2 to 6

Removal of CMK-3

TGA was performed on CMK-3 and CMK-3/BN to identify the temperature for complete removal of CMK-3. It is clear from Figure 6.6 that the presence of BN inside CMK-3 profoundly increases the degradation temperature of CMK-3 from approximately 450 °C to 550 °C. The remaining 30% of material after burning of the carbon is BN. At around 900 °C a small increase in weight is noticed which is due to the oxidation of boron nitride to boron trioxide

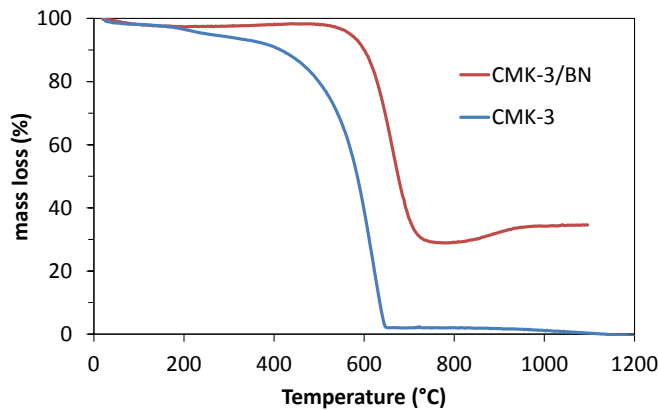


FIGURE 6.6: TGA curves of CMK-3 and CMK-3/BN material at 10 °C/min in air.

The removal of the carbon template should result in mesoporous BN. The heat treatment in air of the CMK-3/BN composite was performed at different temperatures to remove the carbon. Table 6.2 shows that at 500 °C the

Table 6.2: Properties of hard template BN after carbon removal at different temperatures in air.

Temperature (°C)	500	550	600	650	800
Mass loss (%)	47	72	67	66	/
Colour	black	gray	gray-white	gray-white	gray-white
S_{BET} (m ² /g)	325	none	none	none	/

resulting powder was still black but some porosity was found, evidenced by a specific surface area amounting to 325 m²/g and pore volume of 0.37 cm³/g. The removal of carbon was completed at higher temperatures of minimum 550 °C indicated by the color or mass loss of about 70%. The color of the material changed from black to gray-white indicating the removal of carbon from the material. However, higher temperatures resulted in the collapse of the structure. This could be due to the insufficient structural stability of the material formed in the CMK-3 template pores. With a ceramic yield of 37% there may not be sufficient BN to form a stable porous network. The best material in terms of porosity is the one treated at 500 °C. However, the porosity of this material is too low compared to other porous BN materials and is unable to compete with state of the art BN or carbon adsorbents [21,91,168]). Therefore, a new synthesis pathway was investigated to obtain porous BN.

6.3.2 Template-free h-BN

Synthesis of the precursor melamine diborate complex

This alternative synthesis route is based on a template-free mechanism, in which the precursor is able to introduce porosity by forming gasses during the synthesis. The selected precursor was melamine diborate. For the preparation of the melamine diborate complex, melamine and boric acid are dissolved in water at elevated temperature. By gradually cooling the mixture, melamine diborate crystals precipitate. A melamine:boric acid ratio (1:2) precursor was synthesized and the purity was evaluated by elemental analysis (Table 6.3). The composition is close to the calculated theoretical wt% for pure C₃H₆N₆ x 2H₃BO₃. The 1:2 ratio allows the planar triangular boric acid molecules and the melamine molecules to form a three-dimensional hydrogen-bonded supramolecular structure as seen in Figure 6.7 involving O–H · · · O, N–H · · · O and O–H · · · N hydrogen bonds [182].

The gradual transformation of the melamine diborate supramolecular structure to h-BN as followed by TGA starts at 110 °C where a first mass loss

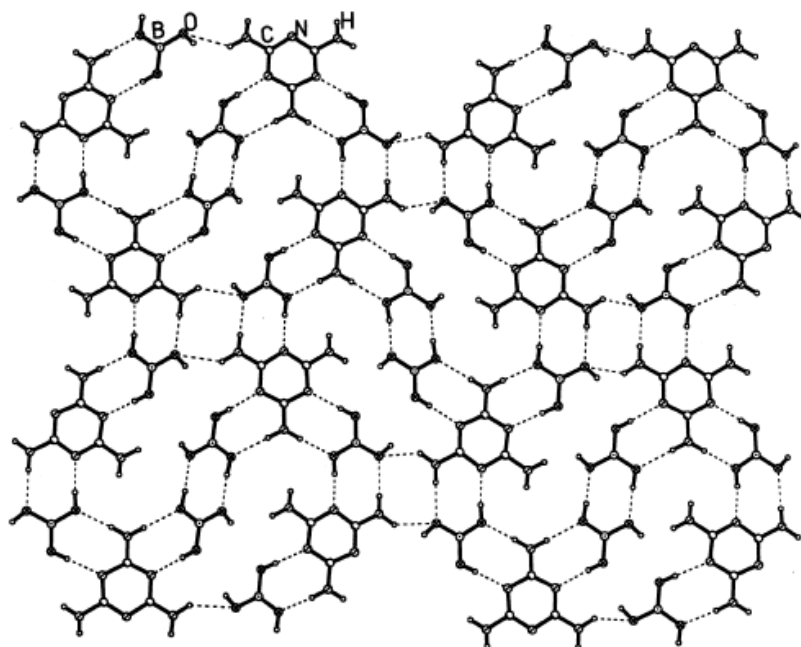
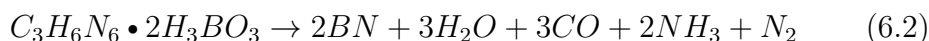


FIGURE 6.7: Supramolecular structure of melamine diborate precursor.

develops amounting to about 30 wt% up until 250 °C. It is attributed to the dehydration of boric acid to metaboric acid and boron trioxide [183]. At 400 °C different reaction gasses (N_2 , H_2O , CO and NH_3) are released during melamine diborate decomposition. The formation of BN is explained by the reaction of boron trioxide and NH_3 at high temperatures [183]. The theoretical ceramic yield derived from melamine diborate following the reaction in Equation 6.2 is limited to 19.9% only.



Effect of ceramization temperature

The nitrogen isotherms of the BN-x materials are shown in Figure 6.8. All isotherms are type IV, and reveal the characteristics of micro- and mesopores. A clear hysteresis H4 can be observed between relative pressures (p/p_0) from 0.42 to 1.0. This long delayed desorption isotherm indicates the presence of slit-shaped pores. The pore size distribution indicates a high amount of micropores (<2 nm) together with mesopores between 2 and 40 nm. An increase in specific surface area and pore volume from respectively 855 to 959 m^2/g

Table 6.3: CHNS analysis for the melamine diborate complex synthesized with melamine to boric acid.

Precursor:	N	C	H	B + O*
$C_3H_6N_6:H_3BO_3$	(wt%)	(wt%)	(wt%)	(wt%)
Theoretical	33.6	14.4	4.80	47.1
1:2	33.5	15.3	4.81	46.4

*wt% B + O is calculated via $100\% - \text{wt}\% (C+N+H)$.

and 0.45 to 0.55 cm^3/g was observed with an increase in ceramization temperature from 1400 °C to 1700 °C (Table 6.4). Between 1400 °C and 1600 °C the most significant change was the increase in pore diameter from 13 nm to 22 nm. More important and interesting is the increased mesoporosity when the ceramization of melamine diborate was performed at 1700 °C.

Table 6.4: Material characteristics of the template-free BN-x with ceramization at different temperatures.

Material	S_{BET}	S_{meso}	S_{micro}	V_{tot}	V_{meso}	V_{micro}	D_p
	(m^2/g)	(m^2/g)	(m^2/g)	(cm^3/g)	(cm^3/g)	(cm^3/g)	(nm)
BN-1400	855	185	670	0.45	0.16	0.29	13
BN-1600	815	233	582	0.40	0.16	0.24	22
BN-1700	959	521	438	0.55	0.24	0.31	27

With powder XRD, the phase purity and crystal structure of the BN-x materials were investigated (Figure 6.9). The appearance of the two broad peaks at 24–26° and 43–46° are attributed to (002) and unresolved (10) reflections of turbostratic BN (t-BN) phase with low crystalline BN structure. The broadened peaks indicate the possible presence of highly defective and randomly stacked layers of the BN sample [175, 180, 181, 184]. The sharp (002), (101) peaks as seen from non-porous commercial h-BN in Figure 6.9 indicate a hexagonal type crystal structure. Increasing ceramization temperatures results in a more narrow and intense diffraction peak 26°, this indicates an increase in h-BN phase. Higher temperatures resulted in an increase in crystallinity from t-BN to more h-BN. t-BN is a disordered BN-phase with high amount of microstructural defects [185]. Increasing temperatures have shown to transform the microstructural defects of t-BN to a more ordered and stable h-BN [186]. The BN-1700 however still shows both turbostratic and hexagonal BN phase.

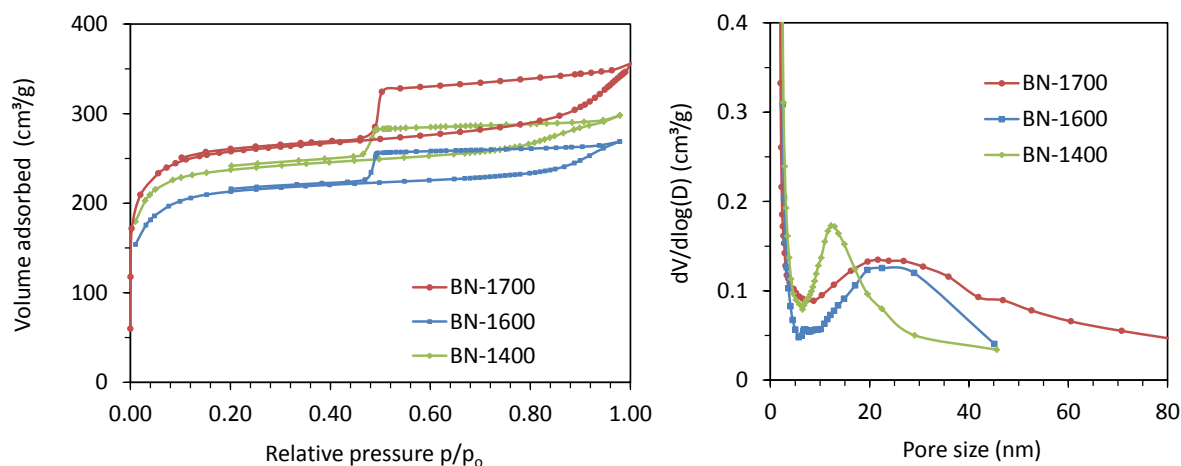


FIGURE 6.8: Nitrogen sorption isotherms of the template-free BN- x materials.

The porous BN-1700 was analyzed via IR and compared to commercial h-BN in Figure 6.10. The most important information deduced from the spectra was the strong peak at around 1370 cm^{-1} that was attributed to the stretching frequency of B–N bond and the peak at around 760 cm^{-1} that was ascribed to the bending of B–N–B [164, 169, 187]. Both peaks were found in the commercial h-BN as well as in BN-1700. No other surface bonds were found in the IR spectra of the synthesized BN which indicate B–OH (3420 cm^{-1}), B–NH₂ (3250 cm^{-1}), B–N–O (930 cm^{-1} and 1160 cm^{-1}) or C–O bonds (1080 cm^{-1}) are absent [187].

Via SEM (Figure 6.11) and TEM (Figure 6.13) the morphology and the porosity of BN-1700 was investigated. The BN-1700 structure retains the structure of the melamine diborate crystals and mesoporosity seems to be present between different layers of BN, as observed in Figure 6.11. The material seems to have slit-shaped pores with a diameter between 2 and 50 nm. TEM visualizes the nanostructure of the material: Figure 6.13 shows the typical interplanar distance of 0.34 nm between two h-BN layers which corresponds to the (002) plane. The structure is composed of multiple ordered h-BN domains in between disordered amorphous or t-BN as well.

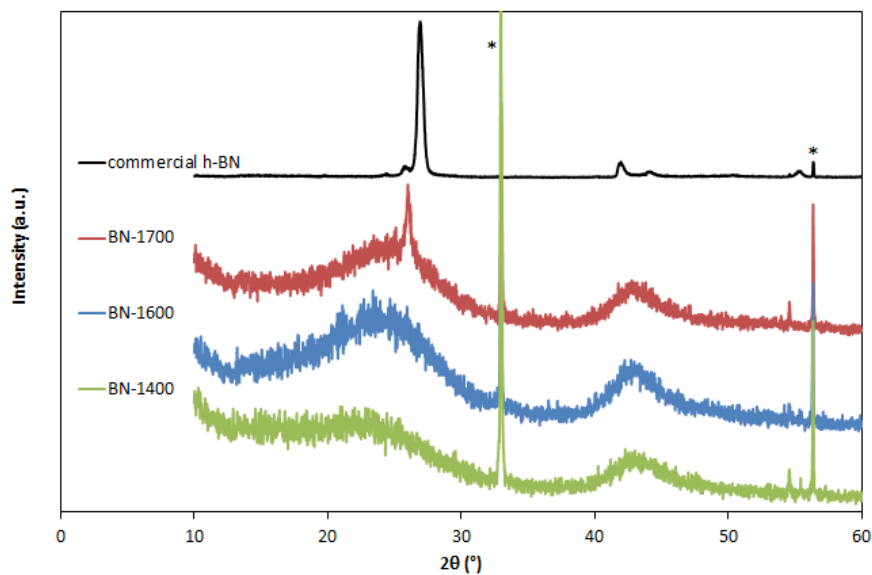


FIGURE 6.9: Powder X-ray diffraction patterns of commercial h-BN and template-free BN-x, * = peaks from sample holder.

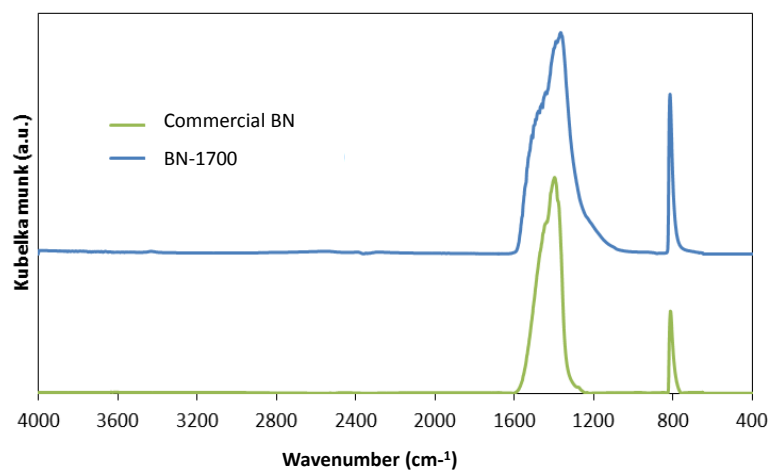


FIGURE 6.10: IR spectra of template-free BN-1700 and commercial h-BN.

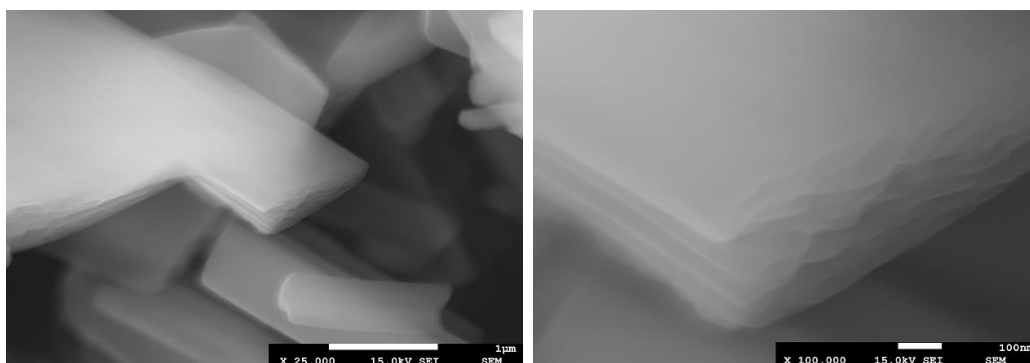


FIGURE 6.11: SEM pictures of template-free BN-1700 with a clear lamellar structure of the slit shaped pores at 25k magnification (left) and 100k magnification (right).

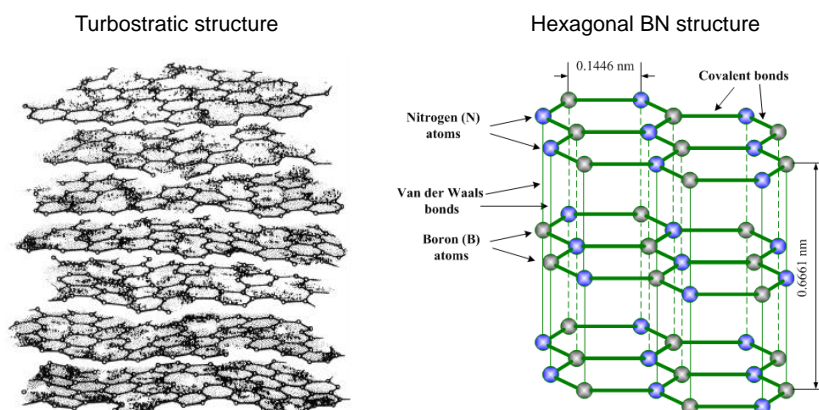


FIGURE 6.12: Schematic representation of turbostratic and hexagonal BN.

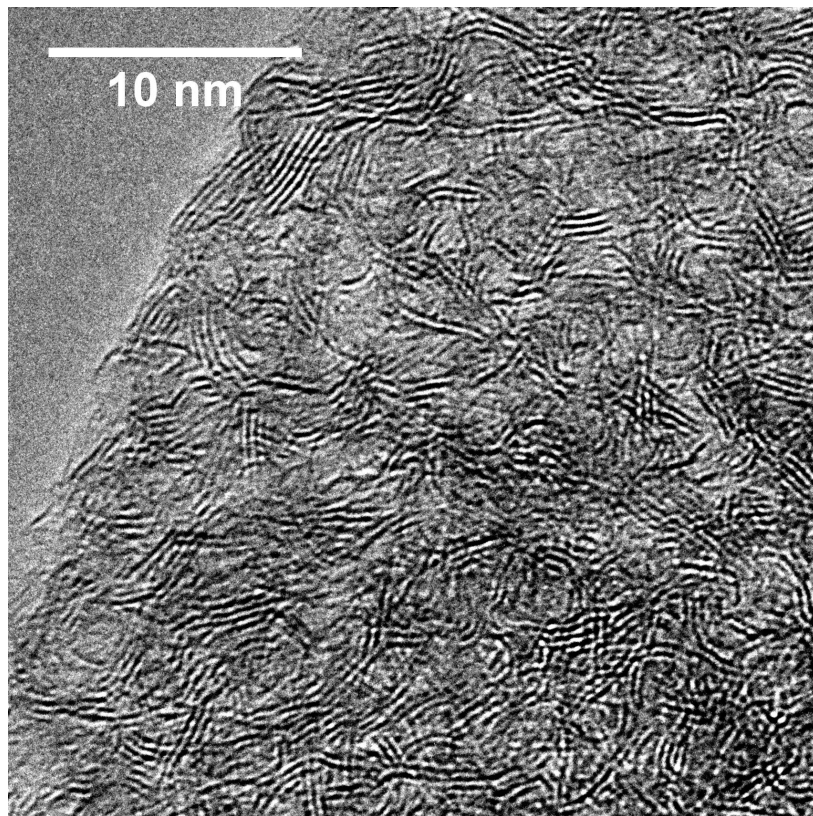


FIGURE 6.13: TEM picture of template-free BN-1700 comprised of disordered h-BN sheets with an interplanar distance of 0.34 nm.

6.3.3 Adsorption experiments

Adsorption of the organic pollutant BPA was performed on the BN-x samples: Figure 6.14. The most important adsorbent material characteristic is often the specific surface area. Although the specific surface area of the different BN-x samples does not vary that much, e.g. from BN-1400 to BN-1700 the specific surface area increases from $855 \text{ m}^2/\text{g}$ to $959 \text{ m}^2/\text{g}$, the BPA adsorption capacity after 1h increases from 175 mg/g to 290 mg/g . A possible explanation is that the mesopores are more important for BPA adsorption. As they are more easily accessible, the adsorption capacity increases with the mesoporous surface area. Another explanation could be the increasing h-BN phase present in the material, which is clear from the XRD spectra (Figure 6.9).

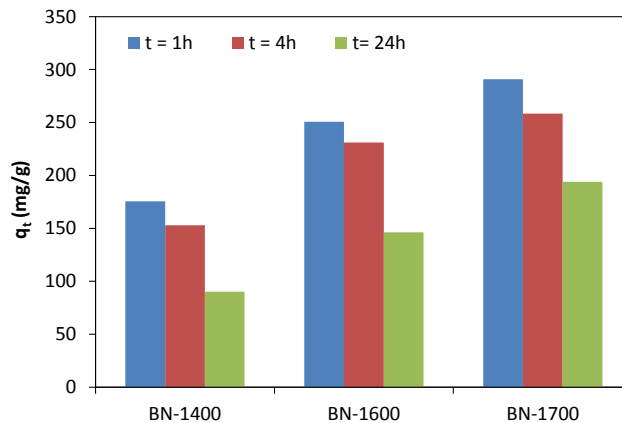


FIGURE 6.14: BPA adsorption capacities of BN-x after 1h, 4h and 24h adsorption time. 10mg of BN material was added to 100 mL of 60 mg/L BPA-solution, stirred at 200 rpm at 25 °C.

Xue et al. attributed methylene blue adsorption onto h-BN surface to hydrophobic π - π -stacking interactions [174], so the aromaticity of BPA could also result in a π - π -stacking adsorption mechanism. An increasing h-BN phase being more prominent in the adsorption material allows for more π - π -stacking interaction, hence, increasing the total adsorption capacity. However, a significant decrease of the adsorption capacities after 4h and 24h was observed. The materials appeared to be unstable in aqueous solution thereby releasing BPA. The BN-1700, with increased amount of h-BN phase, appeared to be more stable than the other materials but still experiences degradation.

The adsorption of another organic pollutant, toluene was tested. The application of porous BN to adsorb toluene vapor was tested via the autochem equipment (Micromeritics). At first the samples were pretreated at 300 °C in a helium flow. Secondly, a fixed number of toluene vapor pulses were sent over the adsorbent at a temperature of 50 °C with a helium flow. Afterwards the sample was heated and thermal programmed desorption (TPD) measurements were performed as seen in Figure 6.15. Via the TPD-curve and the mass of adsorbent used, the adsorption capacities were calculated and resulted in 456 mg/g and 516 mg/g for BN-1700 and AC respectively. Porous BN was capable of adsorbing almost as much toluene vapor as AC. Further testing of the regeneration and stability of BN is necessary, but the material already showed its stability in 500 °C in air. This thermal stability could make BN an interesting adsorbent material in which organic pollutants could be burned off easily and the adsorbent recovered.

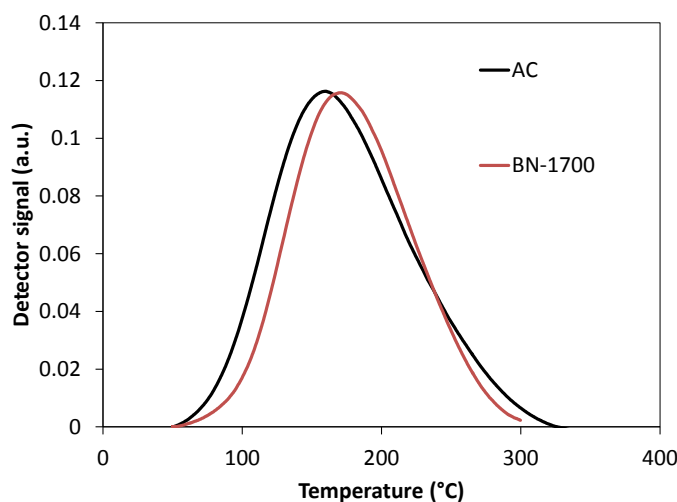


FIGURE 6.15: TPD curves of toluene from AC (black) and BN-1700 (red) heated at 30 °C/min to 400 °C.

6.3.4 BN stability

The adsorption experiments showed promising results at first, but a gradual decrease of adsorption capacity indicates material degradation at aqueous conditions. Therefore, the stability of BN-1700 was investigated in more detail and evaluated via nitrogen sorption measurements. Li et al. was able to synthesize a porous BN from melamine diborate at 1560 °C in nitrogen at-

mosphere and a subsequent treatment in air at 550 °C to remove remaining carbon. The resulting white h-BN had a specific surface area of 1687 m²/g and a pore volume of 0.99 cm³/g, the resulting bimodal pore size was around 1.3 nm and 3.9 nm [169]. All synthesized BN-x powders were black, indicating the presence of carbon impurities, this was investigated with TGA in Figure 6.16. About 10% carbon was removed by oxidation at about 500 °C, the sharp increase in mass starting at 900 °C is the oxidation of BN into B₂O₃. Therefore, BN-1700 was treated at 500 °C in air for 4h (BN-1700-500 °C-4h) and 24h (BN-1700-500 °C-24h) which resulted in gray-white powders. These were characterized with N₂-sorption: Figure 6.17 and Table 6.5. The exposure at 500 °C for 4h did not damage the material, extra mesoporosity was created during carbon removal. The prolonged exposure to air for 24h significantly decreased its microporosity while the mesoporosity only decreased slightly.

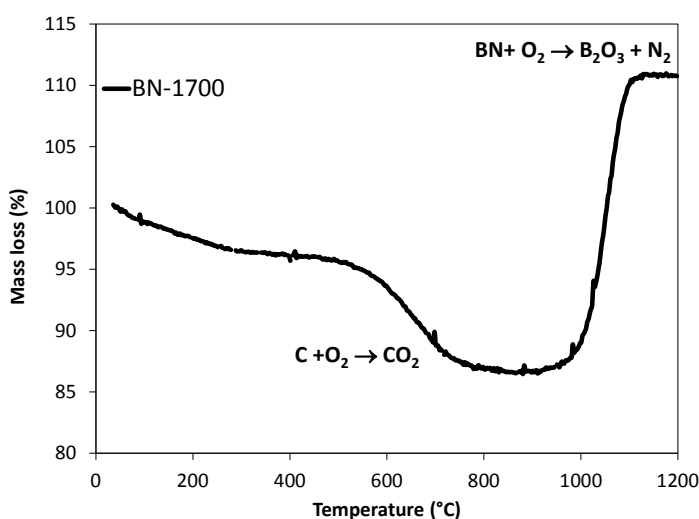


FIGURE 6.16: TGA curve of BN-1700 heated at 10 °C/min in air.

The stability in water was tested by immersing BN-1700 in water for 24h. Loss in both micro- and mesoporosity is observed as seen in Table 6.5. This explains the decrease in adsorption capacity (Figure 6.13) and poses a problem for its application as an adsorbent in water. It is known that h-BN is insoluble in water and does not interact with H₂O molecules [163, 188]. However, Streletskii et al. found that amorphization of h-BN promotes its interaction with water. They found that BN hydrolysis becomes significant at increased amorphization. The interaction with water involves the most defective amorphous fractions of BN [189]. This could explain the gradual deterioration of the BN-1700. If there are reactive amorphous or t-BN sites remaining as seen in Figure ??, the hydrolysis of BN into NH₃ and B₂O₃ could take place.

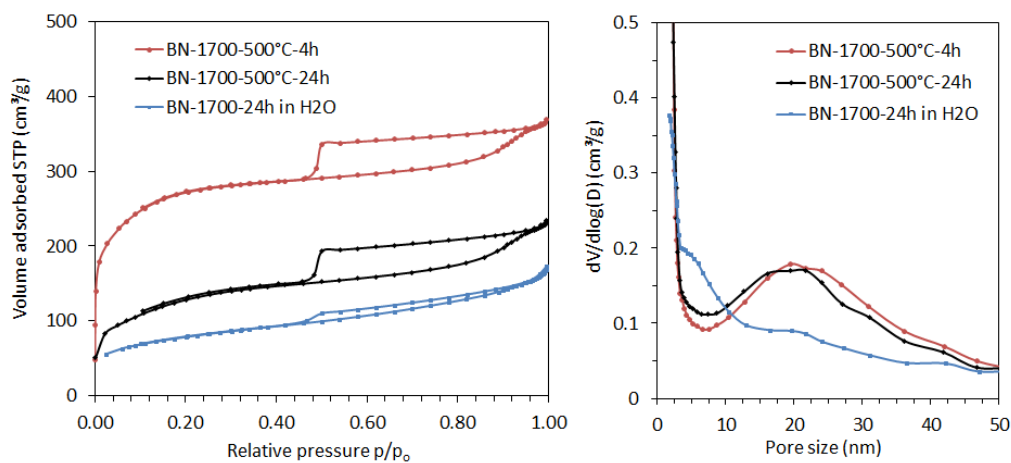


FIGURE 6.17: Nitrogen sorption measurements of template-free BN-1700 after stability tests in air at 500 °C and in water.

Table 6.5: Material characteristics of BN-1700 after stability tests.

Material	S_{BET} (m ² /g)	S_{meso} (m ² /g)	S_{micro} (m ² /g)	V_{tot} (cm ³ /g)	V_{meso} (cm ³ /g)	V_{micro} (cm ³ /g)	D_p (nm)
BN-1700-500-4h	965	705	260	0.57	0.35	0.23	23
BN-1700-500-24h	464	395	69	0.32	0.30	0.02	20
BN-1700-24h in H ₂ O	280	260	20	0.28	0.25	0.03	10

6.4 Conclusions

Porous BN was synthesized via two different pathways, the hard template route and template-free route. Via the hard template route, ammonia borane, a high yield precursor of BN was successfully synthesized and impregnated into a carbon template CMK-3. Upon ceramization, NH_3BH_3 transformed into BN and removal of the carbon template was performed via oxidation in air. The presence of BN however increased the stability of carbon which was difficult to remove. A porous BN was obtained after oxidation at $550\text{ }^\circ\text{C}$, but only had $330\text{ m}^2/\text{g}$ specific surface area. Harsh oxidation conditions destroyed the porous BN and porosity was lost.

An alternative, template-free route was investigated in which melamine diborate was synthesized from a melamine:boric acid ratio of 1:2. The ceramization temperature was varied from $1400\text{ }^\circ\text{C}$ to $1700\text{ }^\circ\text{C}$. Increasing ceramization temperature increased the specific surface area to almost $1000\text{ m}^2/\text{g}$ and also introduced more mesoporosity compared to $1400\text{ }^\circ\text{C}$. Both micropores ($<2\text{ nm}$) and mesopores from $2\text{-}40\text{ nm}$ were observed. The higher temperatures resulted in an increased crystallinity of BN, BN-1700 showed a sharper, more intense (002) reflection indicating a more hexagonal phase.

Adsorption tests for bisphenol A (BPA) showed an increased adsorption capacity for BN with a ceramization temperature of $1700\text{ }^\circ\text{C}$, which could be attributed to the increased mesoporosity of the material, facilitating the adsorption inside the slit shaped pores. Also a more hexagonal phase could be more favorable for the adsorption. BPA will most likely adsorb onto the hexagonal plane of BN because the adsorption mechanism consists of π - π -stacking interaction. However, after longer immersion in water, the adsorption capacities decreased because of material degradation. The porosity decreased drastically after immersion for 24h. Further research in the stabilization of this material is crucial before it can be used as a competitive adsorbent in water. Increasing h-BN phase will improve the stability of the material, an efficient method to remove carbon and stimulate h-BN formation is required. Ceramization or post-treatment in NH_3 could be investigated.

To address the growing challenges related to water pollution and reduce the amount of organic pollutants that end up in our aquatic systems, novel and efficient adsorbents need to be developed. In this PhD thesis, a rational approach was employed to synthesize mesoporous carbon and boron nitride. First, the relationship between synthesis conditions and the material properties was established. Secondly, the newly synthesized adsorbents were evaluated for the adsorption of organic pollutants from water.

The soft template synthesis of mesoporous carbon was thoroughly investigated with a new type of design of experiment, Definitive Screening Design. This method allowed the identification of significant parameters contributing to the formation of micro- or mesopores with a minimum of experiments. The ratio, precursor to surfactant, carbonization temperature and curing time were identified as important parameters to control the mesoporosity. Microporosity was influenced by the curing time and the carbonization temperature. Via DSD a predictive model for the resulting material properties was constructed. The mesoporous surface area was optimized via this model. This optimum was confirmed via a validation experiment that resulted in a high mesoporous surface area amounting to 393 m²/g, a total surface area of 712 m²/g and a pore volume of 0.78 m³/g. Subsequently, the potential use of the synthesized carbons as adsorbent for BPA was investigated. Both S_{meso} and wt% C were identified as significant factors for the BPA adsorption. A higher carbon content indicates a more hydrophobic surface area which will improve the adsorption capacity due to the adsorption involving mainly π - π interactions. A higher mesoporous surface area indicates more available surface for adsorption and increased the adsorption capacity.

Next, a more detailed study of BPA adsorption on synthesized hard (CMK-3) and soft (SMC) templated mesoporous carbons as well as commercial activated carbon was performed. These three carbon adsorbents have a completely different pore geometry. The main advantage of mesoporous carbons was the faster adsorption kinetics as the 2D hexagonal structure of the mesoporous carbons improves diffusion in the pores. The slower adsorption with larger particle size was attributed to intraparticle diffusion and was more pronounced in AC compared to soft templated mesoporous carbon. The maximum BPA adsorption capacity increased with the specific surface area of the adsorbent. However, the calculated number of molecules per nm² was higher for the mesoporous carbons in comparison to AC. This difference was attributed to the more hydrophobic character of the mesoporous materials compared to activated carbon.

The variability of synthesis conditions of soft templated mesoporous carbon allowed to tune the material characteristics to specific requirements. The ratio 'precursor to surfactant' (p/s) was already identified as an important parameter. Further investigation led to synthesis of large pore mesoporous carbons. By decreasing the p/s ratio, the mesophase changed from a 2D hexagonal ordered structure to a disordered large mesoporous network. The average pore diameter increased from a typical 7 nm up to 25 nm and even 50 nm. With increasing pore size, the pore size distribution became broader as well. The new synthesis conditions resulted in a porous carbon with micro-, meso- and even macropores. These large pore mesoporous carbons were tested for the very large adsorbate humic acid and compared to activated carbon. The adsorption of humic acid increased with pore size. A very high maximum adsorption capacity of 540 mg/g was found for the mesoporous carbon with the largest pores. Another factor affecting the adsorption was the hydrophobicity of the material. Mesoporous resins synthesized at 400 °C exhibited a lower adsorption capacity than the more hydrophobic mesoporous carbons treated at 800 °C. The adsorption kinetics of humic acid was faster for the mesoporous carbons than for the activated carbon.

Hexagonal boron nitride was investigated as a possible chemically and thermal stable porous adsorbent. A hard template route in which ammonia borane was impregnated in a mesoporous carbon CMK-3 was investigated. Because of difficulties in carbon removal and the low specific surface area of the BN, a new and alternative approach was pursued. A template-free synthesis was investigated with melamine diborate as a precursor. The precursor melamine diborate was synthesized from a melamine:boric acid mixture with a ratio of 1:2. The ceramization temperature was varied from 1400 °C to 1700 °C. Increasing ceramization temperature increased the specific surface area to almost 1000 m²/g. Higher temperatures also introduced more mesoporosity, both micropores and mesopores from 2-40 nm were observed. The

mesoporosity originated from sheet-like pores in the BN crystals. Increasing temperatures also increased the amount of hexagonal phase in the BN. Adsorption tests for BPA showed an increased adsorption capacity for BN-1700, which could be due to the increased mesoporosity of the material, facilitating the adsorption inside the slit-shaped pores. Also more hexagonal phase could be favorable for the adsorption as BPA will probably adsorb onto the hexagonal plane more easily because of π - π -stacking interaction. However, after prolonged immersion in water, the adsorption capacities decreased because of material degradation. Increasing the stability of these materials will be crucial for their use as adsorbents.

In conclusion, soft templated mesoporous carbons are versatile materials in which material properties can be tuned to meet specific requirements. Their mesoporosity resulted in significant faster adsorption of bisphenol A compared to the micropores in activated carbon. A facile method to control the pore diameter was established, increasing the pore diameter greatly enhanced the adsorption of humic acid. More extensive research will be required to reduce the production costs and enhance the regeneration and reusability of mesoporous carbon adsorbents to ensure their applicability in industrial adsorption processes. New, low-cost precursors or bio-based precursors could lower the production cost of mesoporous carbons. Research into the effect of mesopores or the stability of the carbon framework during regeneration processes could expose new advantages of mesoporous adsorbents. These large pore mesoporous carbons could also be further researched for different applications. Introducing new functionalities to the carbon surface for catalysis or biosensing applications or embedding the mesoporous carbons with nanoparticles for catalysis and the synthesis of magnetic materials for easy separation.

8.1 English summary

Mesoporous adsorbents are materials with pore diameters between 2 and 50 nm. Organic pollutants can be adsorbed inside these pores. The large pores can provide strategic advantages in accessibility or transport of pollutants compared to conventional adsorbents, such as activated carbon, with a pore size limited to micropores (< 2 nm). Two mesoporous adsorbent types were investigated as part of this PhD: mesoporous carbon and mesoporous boron nitride. Mesoporous carbons were synthesized via a soft template method, which uses the organic-organic self-assembly of carbon precursors (e.g. phenol, resorcinol) with a micelle-forming surfactant (e.g. P123, F127). An acid or base catalyzed polymerization of the precursor around these micelles takes place and the carbon polymers crosslink around these micelles to create the framework. Finally, the crosslinked polymer is transformed into a mesoporous resin when heated below 600°C and transforms into a mesoporous carbon when heated above 600°C . The flexibility of the soft template synthesis has resulted in a broad variation of precursors, surfactants, and reaction conditions. The selection of both precursor and surfactant, their ratio, acid or base catalyzed synthesis, synthesis route (EISA, phase separation or hydrothermal) and carbonization temperatures affects the material characteristics. Important material characteristics for an adsorbent are: specific surface area, pore volume, pore size and surface chemistry. These could be tailored depending on the target adsorbate. Due to the hydrophobic nature of mesoporous carbons they are especially interesting for the adsorption of organic pollutants from water.

8.1.1 Optimization of mesoporous carbon synthesis via DSD

Due to the large number of synthesis variables, the synthesis of soft templated mesoporous carbons was optimized with a Definitive Screening Design (DSD), a recently developed design of experiments (DOE) technique. Such a design enables to investigate the effects of synthesis conditions including their interactions or quadratic effects, on the material characteristics. A set of synthesis parameters was selected based on preliminary experiments and literature survey. The parameters were: precursor to surfactant ratio, curing time, EISA surface area and duration and carbonization temperature. The effect of these synthesis parameters on the material properties (microporous surface area (S_{micro}), pore volume (V_{micro}), mesoporous surface area (S_{meso}), pore volume (V_{meso}) and carbon content (wt% C) were investigated.

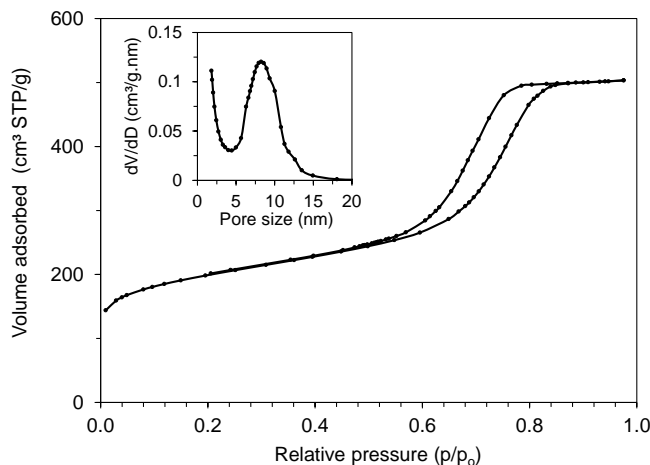


FIGURE 8.1: Nitrogen sorption isotherm and pore size distribution (inset) for the mesoporous carbon with optimized S_{meso} .

The analysis of the results obtained via DSD showed that mesoporosity was influenced mostly by the precursor to surfactant ratio, other significant effects were curing time and carbonization temperature. The microporosity was significantly influenced by the curing time and the carbonization temperature. The DSD was then used to optimize the mesoporous surface area which could improve its potential as adsorbent. A value of 0.83 for precursor to surfactant ratio was found and a carbonization temperature of 600 °C. A validation experiment resulted in a material with optimal mesoporous surface area (393 m²/g), a total specific surface area of 712 m²/g and a large pore volume of 0.78 cm³/g (Figure 8.1 and Table 8.1).

Table 8.1: Material properties of the mesoporous carbon and predicted values with optimized S_{meso} .

Material	S_{BET} (m ² /g)	S_{meso} (m ² /g)	S_{micro} (m ² /g)	V_{tot} (cm ³ /g)	V_{meso} (cm ³ /g)	V_{micro} (cm ³ /g)	D_p (nm)	C-content (wt%)
Optimal	712	393	319	0.78	0.64	0.14	7.8	87.1
Predicted	647	393	250	0.64	0.52	0.12	-	90.1

Subsequently, the potential use of the synthesized carbons as adsorbent for bisphenol A (BPA) was investigated via stepwise regression analysis. This gave insight in the relationship between the structural characteristics and the BPA adsorption performance of the DSD carbons. This analysis identified S_{meso} and wt% C as significant factors. A higher carbon content or a more hydrophobic surface area, due to the adsorption involving mainly π - π interactions, as well as a higher mesoporous surface area, increased the adsorption capacity.

8.1.2 Influence of pore geometry on the adsorption of bisphenol A

Following the optimization study of soft templated mesoporous carbons and their BPA adsorption, the effect of different pore geometries on BPA adsorption, was investigated. Kinetic and equilibrium adsorption studies on microporous activated carbon (AC) and hard (CMK-3) and soft (SMC) templated mesoporous carbons were performed (Figure 8.2).

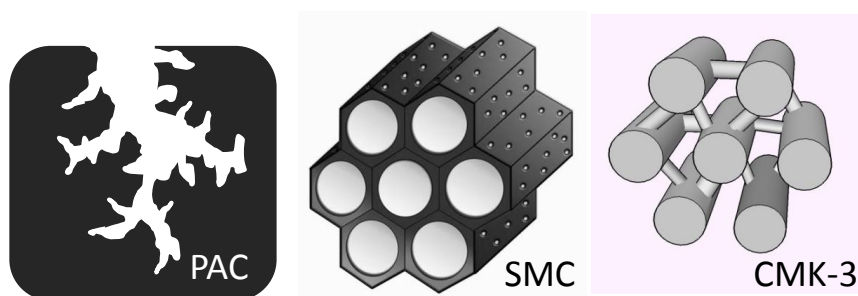


FIGURE 8.2: Schematic representation of microporous AC (left), 2D hexagonal mesoporous structure of SMC (middle) and the interconnected nanorod structure of CMK-3 (right).

The observed maximum BPA adsorption capacity increased with the specific surface area of the materials, CMK-3 showed a very high adsorption ca-

capacity of 474 mg/g, and outperforms AC with an adsorption capacity of 290 mg/g. When calculating the number of molecules adsorbed per nm^2 , both mesoporous materials, i.e. SMC and CMK-3, performed better than AC. This difference was attributed to the more hydrophobic nature of SMC and CMK-3 compared to AC.

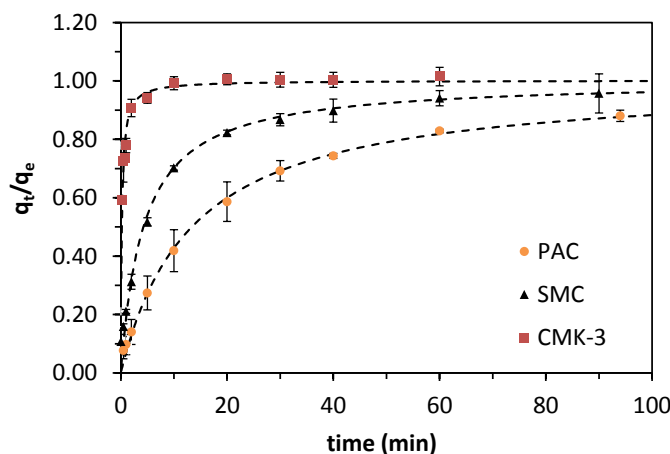


FIGURE 8.3: Adsorption kinetics of 100 mg of CMK-3 (■), AC (●) and SMC (▲) in 1 L of 60 mg/L BPA-solution, particle size is between 62 and 88 μm , the error bars represent the standard deviation of the triplicate measurements, the dashed lines represent the pseudo-second-order kinetic model descriptions.

Both mesoporous materials have a well-ordered 2D hexagonal structure, SMC consists of cylindrical pores with a diameter of 7.0 nm while CMK-3 has an interconnected nanorod structure with an average pore size of 4.0 nm. This resulted in a clear advantage for the adsorption kinetics of the mesoporous materials over AC. The BPA removal rate of CMK-3 was fastest followed by SMC and slowest for AC (Figure 8.3). For both SMC and AC a larger adsorbent particle size resulted in a slower BPA removal, which shows that the adsorption is controlled by intraparticle diffusion, although this effect was much more pronounced for AC than SMC.

8.1.3 Tuning the pore size for enhanced adsorption of humic acid

The great variability of synthesis conditions of soft templated mesoporous carbons allows to tune the material characteristics for specific requirements. For the adsorption of large organic pollutants, e.g. humic acid, the presence of large pores is required. The most reported way to achieve larger pores is to use another surfactant with a larger hydrophobic core. However, changing the precursor to surfactant (p/s ratio) has proven to also alter the mesophase and

affect the resulting pore structure and size. The ability to tailor the pore size of soft templated mesoporous carbons using the acid catalyzed EISA synthesis of resorcinol and F127 by varying the p/s ratio was investigated.

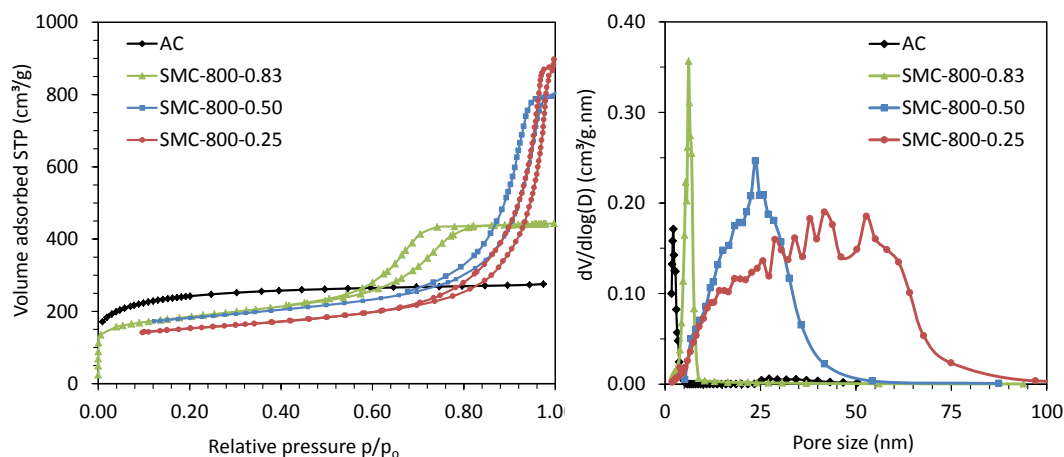


FIGURE 8.4: Nitrogen sorption isotherms (left) and pore size distribution (right) of AC and SMC carbonized at 800 °C with a p/s ratio of 0.83, 0.50 and 0.25.

By decreasing the p/s ratio from 0.83 to 0.5 and 0.25, the mesophase changed from a 2D hexagonal ordered structure to a disordered large mesoporous network. The average pore size increased from the typical 7 nm up to 25 nm and even 50 nm respectively, see Figure 8.4. With increasing pore size, the pore size distribution became broader. The lowest p/s ratio of 0.25 resulted in a porous carbon with micro-, meso- and even macropores. To investigate the effect of the carbonization temperature, the latter was varied from 400 to 800 and 1200 °C. A pronounced difference in the material composition was observed: the wt% C and, hence, hydrophobicity increased with the carbonization temperature. These large pore mesoporous carbons were tested for HA adsorption. Via regression analysis the most significant material properties were found, see Table 8.2. The adsorption capacity increased with pore size and wt% C, indicating that size exclusion effects occur together with a hydrophobic π -stacking adsorption mechanism.

8.1.4 Porous boron nitride as new adsorbent

Hexagonal boron nitride was investigated as a possible chemically and thermally stable porous adsorbent. A hard template route in which ammonia borane was impregnated in a mesoporous carbon CMK-3 was investigated.

Table 8.2: Experimental and predicted adsorption capacities (10 mg adsorbent in 50 mL of 500 mg/L HA-solution, RT, 200 rpm, pH = 7), together with the significant material characteristics pore size D_p and wt% C.

Material	D_p (nm)	wt% C (%)	$q_{e,exp}$ (mg/g)	$q_{e,pred}$ (mg/g)
AC	2.3	86	189 ± 17.2	209
SMC-400-0.83	7.0	77	155 ± 2.0	160
SMC 400-0.5	29.4	77	221 ± 20.1	209
SMC-400-0.25	40.0	82	261 ± 1.3	266
SMC-800-0.83	6.2	90	260 ± 10.6	244
SMC-800-0.5	23.7	95	294 ± 16.6	316
SMC-800-0.25	43.8	92	352 ± 19.8	341
SMC-1200-0.83	6.0	92	275 ± 0.5	257
SMC-1200-0.5	21.5	94	312 ± 12.8	305
SMC-1200-0.25	39.9	93	332 ± 0.5	339

Because of difficulties in carbon removal and the low specific surface area of the BN, a new approach was investigated. A template-free route was investigated in which the precursor melamine diborate was synthesized from a melamine:boric acid precursor mixture amounting to 1:2. The ceramization temperature was varied from 1400 °C to 1700 °C. Increasing ceramization temperatures enhanced the specific surface area to almost 1000 m²/g. Higher temperatures also introduced more mesoporosity, both micropores and mesopores from 2-40 nm were observed (Fig.8.5). The mesoporosity originated from sheet-like pores in the BN crystals. Increasing temperatures enhanced the amount of hexagonal phase in the BN.

BPA adsorption exhibited an increased adsorption capacity for BN-1700 after 1 h, which could be due to the increased mesoporosity of the material, facilitating the adsorption inside the slit-shaped pores. The adsorption interaction of BPA onto BN probably occurs via of π - π -stacking interactions. A more hexagonal phase was therefore more favorable and increased the adsorption capacity for BPA. However, after prolonged immersion in water, the adsorption capacities decreased because of material degradation. Increasing the stability of these materials will be crucial for their use as adsorbents.

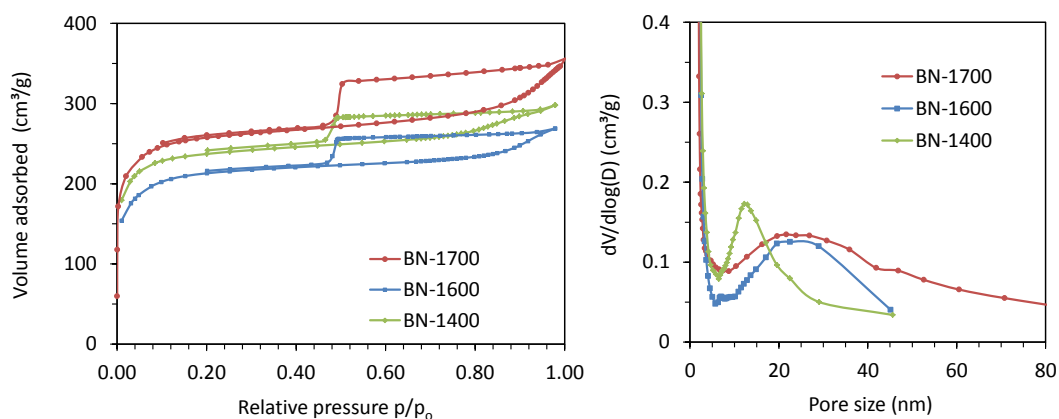


FIGURE 8.5: Nitrogen sorption isotherms (left) of the template-free BN materials ceramized at 1400, 1600 and 1700 °C and PSD (right).

8.1.5 Conclusions and outlook

In conclusion, soft templated mesoporous carbons were investigated and proved to be a versatile material in which material properties can be tuned to meet specific requirements. The mesopores resulted in a significantly faster adsorption of the organic pollutant bisphenol A, compared to the micropores in activated carbon. A facile method to control the pore size was established. The pore size could be increased to further enhance the adsorption of a large organic pollutant, humic acid. More extensive research needs to be done concerning lowering the production costs and the regeneration and reusability of mesoporous carbon adsorbents to improve their applicability in industrial adsorption processes.

8.2 Nederlandstalige samenvatting

Mesoporeuze adsorbentia zijn materialen met poriediameters tussen 2 en 50 nm die de mogelijkheid hebben schadelijke grote moleculen te adsorberen. Het grote verschil met conventionele adsorbentia zoals actieve kool is dat deze laatste microporiën bevatten waarvan de afmetingen gelimiteerd zijn tot 2 nm. Twee types mesoporeuze adsorbentia zijn onderzocht: mesoporeuze koolstof en mesoporeus boornitride.

Mesoporeuze koolstof gebaseerde materialen werden gesynthetiseerd via een zachte-templaatroutte, deze gaat uit van een interactie tussen koolstof-precursoren, zoals resorcinol en formaldehyde met een surfactant zoals F127 of P123, die een geordende micelstructuur aannemen. Door toevoeging van een zuur of base katalysator vindt polymerisatie plaats van de precursoren rond deze micellen. In een volgende stap worden deze polymeren verhit waardoor deze gaan vernetten en de mesostructuur wordt vastgezet. Uiteindelijk wordt het vernette polymeer verhit in een inerte atmosfeer tot hoge temperatuur om het surfactant te verwijderen en porositeit te creëren. Vanaf 400 °C spreekt men van een mesoporous hars, verhit men tot 600 °C of hoger resulteert dit in een mesoporeuze koolstof. De flexibiliteit van de zacht templaat synthese volgt uit een grote variëteit uit precursoren, surfactanten en reactiecondities. Afhankelijk van de gekozen precursor, surfactant, hun verhoudingen, zuur of base katalysator, de syntheseroute (EISA, fasescheiding of hydrothermaal) en carbonisatietemperatuur zullen de materiaaleigenschappen sterk verschillen. Belangrijke materiaaleigenschappen zijn: specifiek oppervlakte, porievolume, poriegrootte en de chemische samenstelling aan het oppervlakte. Deze kunnen dan aangepast worden voor specifieke eisen van de gewenste toepassing of adsorbaat dat moet worden verwijderd. Het hydrofobe karakter van mesoporeuze koolstoffen geeft hen een voordeel in het verwijderen van organische, vervuulende componenten uit water.

8.2.1 Optimalisatie van de mesoporeuze koolstofsynthese

Door het grote aantal synthesecondities is er een rationele aanpak nodig voor de optimalisatie van de synthese. De zachte-templaatsynthese van mesoporeuze koolstoffen werd geoptimaliseerd met behulp van een definitieve screening design (DSD), een recent ontwikkelde design of experiments (DoE) techniek. Zo'n DoE laat toe om het effect van syntheseparameters op de materiaaleigenschappen te onderzoeken. Via DSD worden lineaire, interactie- en kwadratische effecten geïdentificeerd. Welke syntheseparameters werden gevarieerd, werd gebaseerd op preliminair onderzoek alsook op de literatuur. De geselecteerde syntheseparameters waren: precursor tot surfactant verhouding,

vernettingstijd, de duur van het EISA-proces en ook het oppervlakte van het EISA-proces en de carbonisatietemperatuur. Het effect van deze syntheseparameters op de volgende materiaaleigenschappen werd geëvalueerd: microporeus specifiek oppervlakte (S_{micro}) en porievolume (V_{micro}), mesoporeus specifiek oppervlakte (S_{meso}) en porievolume (V_{meso}) en het gewichtspercentage aan koolstof (wt% C).

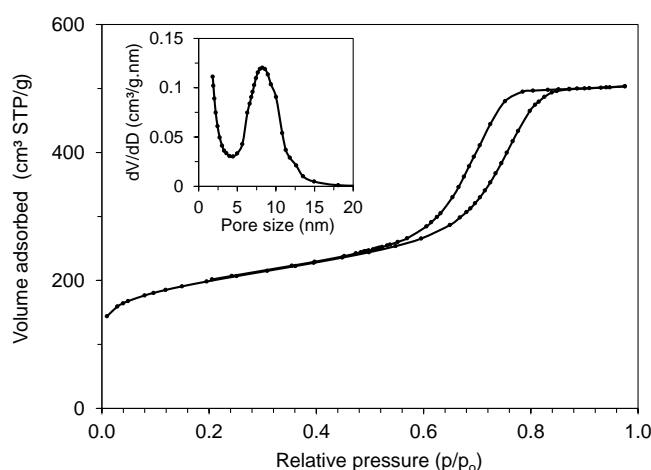


FIGURE 8.6: Stikstofsorptie isotherm en poriegroottedistributie voor mesoporeuze koolstof met geoptimaliseerd S_{meso} .

De resultaten van het DSD toonden aan dat het vormen van de mesoporiën voornamelijk werd beïnvloed door de precursor/surfactant verhouding, andere effecten waren de duur van het vernetten en de carbonisatietemperatuur. De vorming van de microporiën werd enkel beïnvloed door de duur van vernetten en carbonisatietemperatuur. De DSD werd ook gebruikt om de condities te bepalen om een maximaal mesoporeus specifiek oppervlakte te creëren. Een waarde van 0.83 voor precursor/surfactant verhouding en de carbonisatietemperatuur van 600 °C werden gevonden. Deze synthese werd uitgevoerd en resulteerde inderdaad in een hoog mesoporeus specifiek oppervlakte van 393 m²/g, een totaal specifiek oppervlakte van 712 m²/g and een groot porievolume van 0.78 cm³/g (Figuur 8.6 en Tabel 8.3).

Vervolgens werden deze gesynthetiseerde materialen getest voor de adsorptie van bisfenol A (BPA). Via stapsgewijze regressie analyse kon het verband tussen materiaaleigenschappen en adsorptiecapaciteiten voor BPA worden verduidelijkt. Daaruit bleek dat een hoog specifiek mesoporeus oppervlakte S_{meso} en gewichtspercentage koolstof wt% C significant bijdroegen tot

Table 8.3: Materiaaleigenschappen van de mesoporeuze koolstof en de voorspelde waarden voor een geoptimaliseerd S_{meso} .

Materiaal	S_{BET} (m ² /g)	S_{meso} (m ² /g)	S_{micro} (m ² /g)	V_{tot} (cm ³ /g)	V_{meso} (cm ³ /g)	V_{micro} (cm ³ /g)	D_p (nm)	wt% C (%)
Optimum	712	393	319	0.78	0.64	0.14	7.8	87.1
Voorspeld	647	393	250	0.64	0.52	0.12	-	90.1

de adsorptie. Het hoog gewichtspercentage koolstof wijst op een hydrofober materiaal wat de adsorptie tussen het adsorbens en BPA verbetert omdat deze vooral via $\pi - \pi$ interacties verloopt. Een hoger specifiek oppervlakte zal het beschikbare aantal plaatsen voor adsorptie en dus de adsorptiecapaciteit verhogen.

8.2.2 Invloed van de poriestructuur op de adsorptie van BPA

Na de optimalisatie van de synthese van mesoporeuze koolstofgebaseerde materialen en hun adsorptie van BPA, werd het effect van de poriestructuur, zie Figuur 8.7, op de BPA adsorptie onderzocht. Zowel een kinetische als evenwichtsstudie voor microporeuze actieve kool, harde (CMK-3) en zachte (SMC) templaatkoolstof werden uitgevoerd.

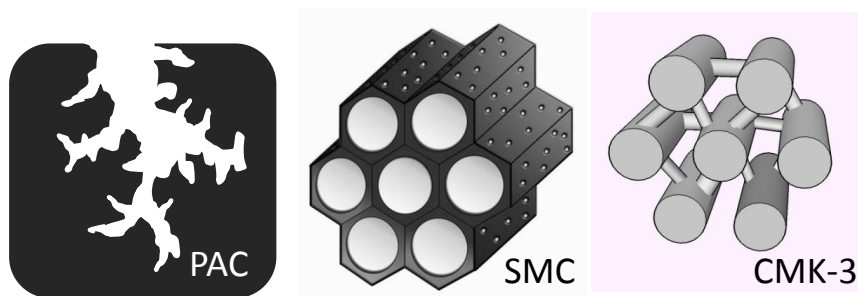


FIGURE 8.7: Schematische voorstelling van microporeus AC, 2D hexagonale mesoporeuze structuur van SMC en de intergeconnecteerde nano-staaf structuur van CMK-3.

Beide mesoporeuze materialen vertoonden een goed geordende 2D hexagonale structuur, het zachte-templaatkoolstof heeft cilindrische poriën van ongeveer 7.0 nm diameter. Het harde-templaatkoolstof bestaat uit onderlinge

verbonden koolstofstaven met poriën rond de 4.0 nm. De maximale hoeveelheid geadsorbeerd BPA werd bepaald voor de 3 materialen. Een belangrijk verband tussen het specifiek oppervlakte en de adsorptiecapaciteit werd vastgesteld. Het harde-templaatkoolstof (CMK-3) vertoonde de hoogste adsorptiecapaciteit van 474 mg/g, gevolgd door actieve kool met 290 mg/g. Het zachte-templaatkoolstof had een capaciteit van 154 mg/g, omdat in verhouding het specifiek oppervlakte het kleinste is van de drie materialen. Op basis van het aantal moleculen per nm^2 , leverden beide mesoporeuze materialen betere waarden op dan actieve kool. Dit werd toegewezen aan een meer hydrofoob karakter van de mesoporeuze koolstofgebaseerde materialen.

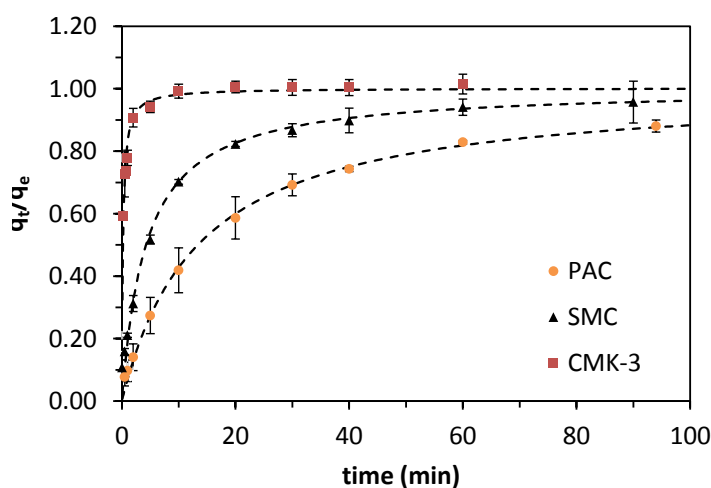


FIGURE 8.8: Adsorptiekinetiek van 100 mg van CMK-3 (■), AC (●) en SMC (▲) in 1 L van 60 mg/L BPA-oplossing, partikelgrootte tussen 62 en 88 μm , de foutenbalken zijn de standaardafwijkingen van de meting in drievoud opgemeten, de stippellijn stelt de pseudo-tweede-orde kinetiek fit voor.

De kinetiekstudie toonde een duidelijk voordeel voor mesoporeuze koolstofgebaseerde materialen t.o.v. actieve kool. De snelheid waarmee BPA verwijderd werd, was het snelst voor CMK-3, gevolgd door SMC en het traagst voor actieve kool, zie Figuur 8.8. Een belangrijke factor bij adsorptiekinetiek is de partikelgrootte van het adsorbens. Voor zowel SMC als actieve kool werden verschillende partikelgroottes getest. Hieruit bleek dat de adsorptiesnelheid sterk afnam met stijgende partikelgrootte en het adsorptieproces dus werd beïnvloed door intrapartikel diffusie. De daling voor actieve kool was veel sterker dan die van de mesoporeuze koolstof. Het harde-templaatkoolstof is met zijn hoge adsorptiecapaciteit en snelle adsorptiekinetiek een interessant adsorbens.

8.2.3 Afstemmen van de poriegrootte van mesoporeuze koolstoffen voor humuszuuradsorptie

De beschikbaarheid aan verschillende synthesecondities van zachte-templaat mesoporeuze koolstoffen laten toe de materiaaleigenschappen te gaan controleren voor specifieke doeleinden. Voor de adsorptie van grote organische moleculen zoals humuszuur is de aanwezigheid van mesoporiën noodzakelijk, en het variëren van de poriegrootte mogelijks interessant. De mogelijkheid werd onderzocht om de poriegrootte te veranderen bij mesoporeuze koolstoffen gesynthetiseerd via een zuurgekatalyseerde *EISA* met resorcinol/formaldehyde precursoren en F127 als surfactant. Meestal is hiervoor een nieuw surfactant type noodzakelijk, in sommige gevallen konden poriegroottes worden gevarieerd door de precursor/surfactant verhouding aan te passen. In dit onderzoek werd nagegaan of dit mogelijk was voor dit type zachte-templaatkoolstoffen en wat het effect is op humuszuuradsorptie.

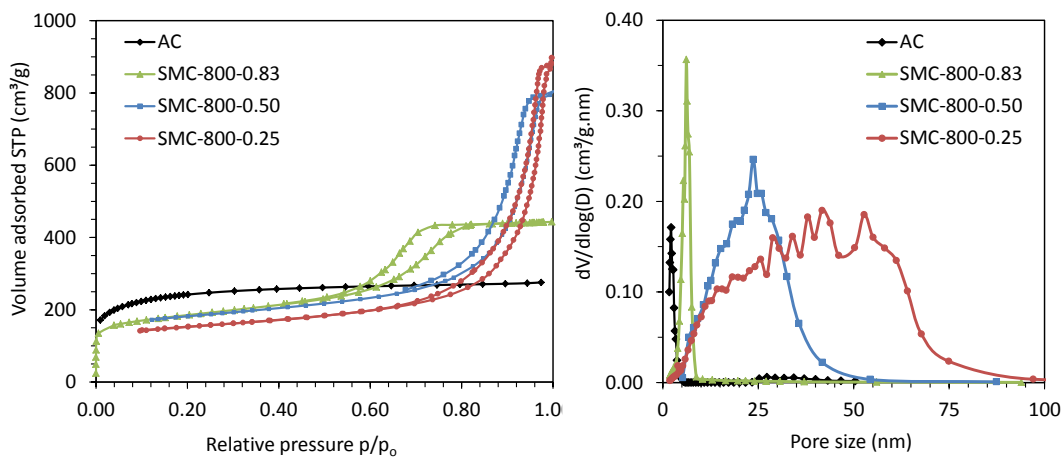


FIGURE 8.9: Stikstofsorptie isothermen (links) en poriegroottedistributies (rechts) van AC en SMC gecarboniseerd bij 800 °C met een p/s verhouding van 0.83, 0.50 en 0.25

Door het verlagen van de precursor/surfactant verhouding van 0.83 tot 0.5 of zelfs 0.25 vond er een verandering van de mesofase plaats. Hierdoor veranderde de 2D hexagonale structuur in een ongeordende structuur met grote mesoporiën. De gemiddelde poriegrootte verhoogde van 7 nm naar 25 nm tot zelfs 50 nm respectievelijk, zie Figuur 8.9. Met een toenemende poriegrootte, verbreedde ook de poriegroottedistributie. De laagst verhouding van 0.25 creëerde een materiaal dat zowel micro-, meso-, alsook macroporiën bevat.

De mesoporeuze koolstoffen met verschillende verhoudingen werden ook bij verschillende carbonisatietemperaturen (400, 800 en 1200 °C) behandeld. Het effect van deze carbonisatietemperatuur was het meeste zichtbaar in de materiaalsamenstelling. Het gewichtspercentage koolstof, en bijgevolg hydrofobiciteit, verhoogde met toenemende carbonisatietemperatuur.

Deze koolstofgebaseerde materialen met grote mesoporiën werden getest voor de adsorptie van humuszuur. Via een regressieanalyse werden de significante materiaaleigenschappen bepaald. De adsorptiecapaciteit steeg met een toename in poriegrootte en ook met een toename in gewichtspercentage koolstof, zie Tabel 8.4. Dit wijst erop dat tijdens de adsorptie zowel hydrofobe interacties plaatsvinden alsook uitsluiting van grote humuszuurmoleculen in kleinere poriën.

Table 8.4: Experimentele ($q_{e,exp}$) en voorspelde ($q_{e,pred}$) adsorptiecapaciteiten (10 mg adsorbens in 50 mL of 500 mg/L HA-oplossing, RT, 200rpm, pH = 7), samen met de significante materiaaleigenschappen: poriegrootte D_p en wt% C.

Materiaal	D_p (nm)	wt% C (%)	$q_{e,exp}$ (mg/g)	$q_{e,pred}$ (mg/g)
AC	2.3	86	189 ± 17.2	209
SMC-400-0.83	7.0	77	155 ± 2.0	160
SMC 400-0.5	29.4	77	221 ± 20.1	209
SMC-400-0.25	40.0	82	261 ± 1.3	266
SMC-800-0.83	6.2	90	260 ± 10.6	244
SMC-800-0.5	23.7	95	294 ± 16.6	316
SMC-800-0.25	43.8	92	352 ± 19.8	341
SMC-1200-0.83	6.0	92	275 ± 0.5	257
SMC-1200-0.5	21.5	94	312 ± 12.8	305
SMC-1200-0.25	39.9	93	332 ± 0.5	339

8.2.4 Poreus boornitride als nieuw adsorbens

Hexagonaal boornitride werd onderzocht als een mogelijk nieuw poreus adsorbens met chemische en thermische stabiliteit. Een harde-templaatmethode werd uitgevoerd waarbij ammoniumboraan in mesoporeuze koolstof CMK-3 werd geïmpregneerd. Door het moeilijk verwijderen van overgebleven koolstof

en het lage specifieke oppervlakte van het resulterende BN werd een andere methode onderzocht. Een templaatsvrije synthesemethode werd hiervoor gebruikt, eerst werd de precursor melamediboraat gesynthetiseerd uit een precursoroplossing met een molaire 1:2 verhouding van melamine en boorzuur. De keramisatietemperatuur werd gevarieerd tussen 1400 °C tot 1700 °C. De hogere temperatuur resulteerde in een groter specifiek oppervlakte voor het materiaal tot bijna 1000 m²/g en er werd meer mesoporositeit geïntroduceerd in het materiaal. Zowel micro- als mesoporiën van 2 tot 40 nm werden geobserveerd, zie Figuur 8.10. De mesoporositeit was terug te vinden tussen verschillende lagen waaruit de BN deeltjes zijn opgebouwd. Bij het BN gesynthetiseerd op hoge temperatuur werd ook meer hexagonale fase teruggevonden.

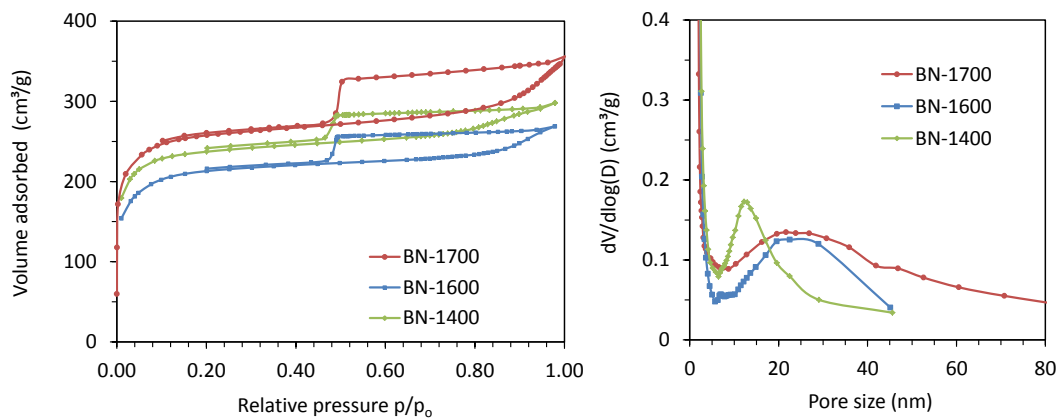


FIGURE 8.10: Stikstofsorptie isothermen (links) en poriegroottedistributies (rechts) van templaatsvrije BN materialen gesynthetiseerd bij 1400, 1600 en 1700 °C.

Adsorptietesten van 1 h voor BPA toonden een stijgende adsorptiecapaciteit met een groter specifiek oppervlakte en een toename aan mesoporositeit. Het groter aandeel hexagonale fase zou ook een positief effect kunnen hebben op de adsorptie van BPA, omdat dit meer π - π -stacking mogelijk maakt. Echter, na langdurige blootstelling aan water trad een daling van de adsorptiecapaciteit op. Het BN begon te degraderen, de stabiliteit verbeteren zal dus cruciaal zijn om deze materialen in te zetten als adsorbens.

8.2.5 Conclusies en toekomstperspectieven

In dit doctoraat werd de synthese van zachte-templaatkoolstoffen onder de loep genomen. Hieruit bleek dat deze synthese een veelzijdige methode is

waarbij de materiaaleigenschappen op maat kunnen gevarieerd worden. De mesoporiën in de koolstoffen resulteerden in een snellere adsorptie van het organische pollutant bisfenol A dan mogelijk is met actieve kool. Een eenvoudige methode om de poriegrootte te variëren werd ontdekt. De poriegrootte kon zodanig vergroot worden dat het in een verbeterde adsorptie resulteerde voor een zeer groot organisch pollutant humuszuur. Verder onderzoek rond het verlagen van de productiekosten van mesoporeuze koolstoffen zal moeten gebeuren alsook het testen van de regeneratie en herbruikbaarheid van het adsorbens, zodanig dat hun toepasbaarheid in industriële adsorptieprocessen mogelijk wordt.

Bibliography

- [1] UNWater, *The United Nations World Water Development Report*. 2015.
- [2] World Wide Fund for Nature (WWF), “Living planet report,” tech. rep., 1998.
- [3] T. Deblonde, C. Cossu-Leguille, and P. Hartemann, “Emerging pollutants in wastewater: a review of the literature.,” *International journal of hygiene and environmental health*, vol. 214, no. 6, pp. 442–448, 2011.
- [4] M. N. Rashed, “Adsorption Technique for the Removal of Organic Pollutants from Water and Wastewater,” *Organic Pollutants - Monitoring, Risk and Treatment*, pp. 167–194, 2013.
- [5] V. K. Gupta and T. A. Saleh, “Sorption of pollutants by porous carbon, carbon nanotubes and fullerene- An overview,” *Environmental Science and Pollution Research*, vol. 20, no. 5, pp. 2828–2843, 2013.
- [6] R. Ryoo, S. H. Joo, and S. Jun, “Synthesis of Highly Ordered Carbon Molecular Sieves via Template-Mediated Structural Transformation,” *The Journal of Physical Chemistry B*, vol. 103, no. 37, pp. 7743–7746, 1999.
- [7] Y. Meng, D. Gu, F. Zhang, Y. Shi, L. Cheng, D. Feng, Z. Wu, Z. Chen, Y. Wan, A. Stein, and D. Zhao, “A Family of Highly Ordered Mesoporous Polymer Resin and Carbon Structures from Organic–Organic Self-Assembly,” *Chemistry of Materials*, vol. 18, no. 18, pp. 4447–4464, 2006.
- [8] M. Hartmann, A. Vinu, and G. Chandrasekar, “Adsorption of Vitamin E on Mesoporous Carbon Molecular Sieves,” *Young*, no. 12, pp. 829–833, 2005.
- [9] S. Yoon, S. M. Oh, and C. Lee, “Direct template synthesis of mesoporous carbon and its application to supercapacitor electrodes,” *Materials Research Bulletin*, vol. 44, no. 8, pp. 1663–1669, 2009.

- [10] S. Yoon, S. M. Oh, C. W. Lee, and J. H. Ryu, "Pore structure tuning of mesoporous carbon prepared by direct templating method for application to high rate supercapacitor electrodes," *Journal of Electroanalytical Chemistry*, vol. 650, no. 2, pp. 187–195, 2011.
- [11] F. Liu, Y. Gao, S. Zhang, X. Yan, F. Fan, C. Zhao, and J. Sun, "Application of mesoporous carbon and modified mesoporous carbon for treatment of DMF sewage," *Journal of Nanoparticle Research*, vol. 18, no. 2, p. 38, 2016.
- [12] C. Liang, Z. Li, and S. Dai, "Mesoporous carbon materials: Synthesis and modification," *Angewandte Chemie - International Edition*, vol. 47, no. 20, pp. 3696–3717, 2008.
- [13] Y. Qiu, J. Huo, F. Jia, B. H. Shanks, and W. Li, "N- and S-doped mesoporous carbon as metal-free cathode catalysts for direct biorenewable alcohol fuel cells," *J. Mater. Chem. A*, vol. 00, pp. 1–13, 2016.
- [14] R. Ryoo, S. H. Joo, M. Kruk, and M. Jaroniec, "Ordered Mesoporous Carbons," *Advanced Materials*, vol. 13, no. 9, pp. 677–681, 2001.
- [15] A. Sayari and Y. Yang, "SBA-15 templated mesoporous carbon: New insights into the SBA-15 pore structure," *Chemistry of Materials*, vol. 17, no. 24, pp. 6108–6113, 2005.
- [16] Z. Wu, Y. Meng, and D. Zhao, "Nanocasting fabrication of ordered mesoporous phenol–formaldehyde resins with various structures and their adsorption performances for basic organic compounds," *Microporous and Mesoporous Materials*, vol. 128, no. 1-3, pp. 165–179, 2010.
- [17] N. Pal and A. Bhaumik, "Soft templating strategies for the synthesis of mesoporous materials: inorganic, organic-inorganic hybrid and purely organic solids," *Advances in colloid and interface science*, vol. 189-190, pp. 21–41, 2013.
- [18] X. Wang, C. Liang, and S. Dai, "Facile synthesis of ordered mesoporous carbons with high thermal stability by self-assembly of resorcinol-formaldehyde and block copolymers under highly acidic conditions," *Langmuir : the ACS journal of surfaces and colloids*, vol. 24, no. 14, pp. 7500–7505, 2008.
- [19] W. Konicki, K. Cendrowski, X. Chen, and E. Mijowska, "Application of hollow mesoporous carbon nanospheres as an high effective adsorbent for the fast removal of acid dyes from aqueous solutions," *Chemical Engineering Journal*, vol. 228, pp. 824–833, 2013.

- [20] T. Shi, Y. Wen, C. Ma, S. Jia, Z. Wang, and S. Zou, "Adsorption Characteristics of Phenol and Reactive Dyes from Aqueous Solution onto Ordered Mesoporous Carbons Prepared via a Template Synthesis Route," *Adsorption Science and Technology*, no. 27, pp. 643–660, 2009.
- [21] Z. X. Wu and D. Y. Zhao, "Ordered mesoporous materials as adsorbents," *Chemical Communications*, vol. 47, no. 12, pp. 3332–3338, 2011.
- [22] W. Xin and Y. Song, "Mesoporous carbons: recent advances in synthesis and typical applications," *RSC Adv.*, vol. 5, no. 101, pp. 83239–83285, 2015.
- [23] M. Kawahigashi, H. Sumida, and K. Yamamoto, "Size and shape of soil humic acids estimated by viscosity and molecular weight.," *Journal of colloid and interface science*, vol. 284, no. 2, pp. 463–469, 2005.
- [24] F. Liu, Z. Xu, H. Wan, Y. Wan, S. Zheng, and D. Zhu, "Enhanced adsorption of humic acids on ordered mesoporous carbon compared with microporous activated carbon," *Environmental toxicology and chemistry / SETAC*, vol. 30, no. 4, pp. 793–800, 2011.
- [25] N. P. Wickramaratne and M. Jaroniec, "Phenolic resin-based carbons with ultra-large mesopores prepared in the presence of poly(ethylene oxide)-poly(butylene oxide)-poly(ethylene oxide) triblock copolymer and trimethyl benzene," *Carbon*, vol. 51, no. 1, pp. 45–51, 2013.
- [26] C. Liang and S. Dai, "Synthesis of mesoporous carbon materials via enhanced hydrogen-bonding interaction," *Journal of the American Chemical Society*, vol. 128, no. 16, pp. 5316–5317, 2006.
- [27] S. Liu, Z. Huang, and R. Wang, "A carbon foam with a bimodal micro-mesoporous structure prepared from larch sawdust for the gas-phase toluene adsorption," *Materials Research Bulletin*, vol. 48, no. 7, pp. 2437–2441, 2013.
- [28] S. Schlienger, A.-L. Graff, A. Celzard, and J. Parmentier, "Direct synthesis of ordered mesoporous polymer and carbon materials by a biosourced precursor," *Green Chemistry*, vol. 14, no. 2, p. 313, 2012.
- [29] K. M. Nelson, S. M. Mahurin, R. T. Mayes, B. Williamson, C. M. Teague, A. J. Binder, L. Baggetto, G. M. Veith, and S. Dai, "Preparation and CO₂ adsorption properties of soft-templated mesoporous carbons derived from chestnut tannin precursors," *Microporous and Mesoporous Materials*, vol. 222, pp. 94–103, 2016.
- [30] D. Saha, K. E. Warren, and A. K. Naskar, "Soft-templated mesoporous carbons as potential materials for oral drug delivery," *Carbon*, vol. 71, no. 1, pp. 47–57, 2014.

- [31] D. Long, W. Qiao, L. Zhan, X. Liang, and L. Ling, "Effect of template and precursor chemistry on pore architectures of triblock copolymer-templated mesoporous carbons," *Microporous and Mesoporous Materials*, vol. 121, no. 1-3, pp. 58–66, 2009.
- [32] J. G. Li, Y. D. Lin, and S. W. Kuo, "From microphase separation to self-organized mesoporous phenolic resin through competitive hydrogen bonding with double-crystalline diblock copolymers of poly(ethylene oxide-*b*-caprolactone)," *Macromolecules*, vol. 44, no. 23, pp. 9295–9309, 2011.
- [33] Y. Huang, J. Yang, H. Cai, Y. Zhai, D. Feng, Y. Deng, B. Tu, and D. Zhao, "A curing agent method to synthesize ordered mesoporous carbons from linear novolac phenolic resin polymers," *Journal of Materials Chemistry*, vol. 19, no. 36, p. 6536, 2009.
- [34] A. Chen, Y. Yu, Y. Zhang, W. Zang, Y. Yu, Y. Zhang, S. Shen, and J. Zhang, "Aqueous-phase synthesis of nitrogen-doped ordered mesoporous carbon nanospheres as an efficient adsorbent for acidic gases," *Carbon*, vol. 80, no. 1, pp. 19–27, 2014.
- [35] M. Li and J. Xue, "Integrated synthesis of nitrogen-doped mesoporous carbon from melamine resins with superior performance in supercapacitors," *Journal of Physical Chemistry C*, vol. 118, no. 5, pp. 2507–2517, 2014.
- [36] J. Wei, D. Zhou, Z. Sun, Y. Deng, Y. Xia, and D. Zhao, "A controllable synthesis of rich nitrogen-doped ordered mesoporous carbon for CO₂ capture and supercapacitors," *Advanced Functional Materials*, vol. 23, no. 18, pp. 2322–2328, 2013.
- [37] J. Yu, M. Guo, F. Muhammad, A. Wang, G. Yu, H. Ma, and G. Zhu, "Simple fabrication of an ordered nitrogen-doped mesoporous carbon with resorcinol-melamine-formaldehyde resin," *Microporous and Mesoporous Materials*, vol. 190, pp. 117–127, 2014.
- [38] Y. Huang, F. Yang, Z. Xu, and J. Shen, "Nitrogen-containing mesoporous carbons prepared from melamine formaldehyde resins with CaCl₂ as a template," *Journal of Colloid and Interface Science*, vol. 363, no. 1, pp. 193–198, 2011.
- [39] J. Xu, X. Zhao, A. Wang, and T. Zhang, "Synthesis of nitrogen-doped ordered mesoporous carbons for catalytic dehydrochlorination of 1,2-dichloroethane," *Carbon*, vol. 80, no. 1, pp. 610–616, 2014.
- [40] Y. Deng, C. Liu, D. Gu, T. Yu, B. Tu, and D. Zhao, "Thick wall mesoporous carbons with a large pore structure templated from a weakly

- hydrophobic PEO–PMMA diblock copolymer,” *Journal of Materials Chemistry*, vol. 18, no. 1, p. 91, 2008.
- [41] Y. Deng, Y. Cai, Z. Sun, D. Gu, J. Wei, W. Li, X. Guo, J. Yang, and D. Zhao, “Controlled synthesis and functionalization of ordered large-pore mesoporous carbons,” *Advanced Functional Materials*, vol. 20, no. 21, pp. 3658–3665, 2010.
- [42] C. Liang, K. Hong, G. a. Guiochon, J. W. Mays, and S. Dai, “Synthesis of a Large-Scale Highly Ordered Porous Carbon Film by Self-Assembly of Block Copolymers,” *Angewandte Chemie*, vol. 116, no. 43, pp. 5909–5913, 2004.
- [43] J. Górka, C. Fenning, and M. Jaroniec, “Influence of temperature, carbon precursor/copolymer ratio and acid concentration on adsorption and structural properties of mesoporous carbons prepared by soft-templating,” *Colloids and Surfaces A: Physicochemical and Engineering Aspects*, vol. 352, no. 1-3, pp. 113–117, 2009.
- [44] T. Mitome, Y. Hirota, Y. Uchida, and N. Nishiyama, “Porous structure and pore size control of mesoporous carbons using a combination of a soft-templating method and a solvent evaporation technique,” *Colloids and Surfaces A: Physicochemical and Engineering Aspects*, vol. 494, pp. 180–185, 2016.
- [45] J. Choma, K. Jedynak, M. Marszewski, and M. Jaroniec, “Organic acid-assisted soft-templating synthesis of ordered mesoporous carbons,” *Adsorption*, vol. 19, no. 2-4, pp. 563–569, 2013.
- [46] L. Liu, F. Y. Wang, G. S. Shao, T. Y. Ma, and Z. Y. Yuan, “Synthesis of ultra-large mesoporous carbons from triblock copolymers and phloroglucinol/formaldehyde polymer,” *Carbon*, vol. 48, no. 9, pp. 2660–2664, 2010.
- [47] S. Tanaka, N. Nishiyama, Y. Egashira, and K. Ueyama, “Synthesis of ordered mesoporous carbons with channel structure from an organic-organic nanocomposite,” *Chemical communications*, vol. 16, pp. 2125–2127, 2005.
- [48] Y. Deng, T. Yu, Y. Wan, Y. Shi, Y. Meng, D. Gu, L. Zhang, Y. Huang, C. Liu, X. Wu, and D. Zhao, “Ordered mesoporous silicas and carbons with large accessible pores templated from amphiphilic diblock copolymer poly(ethylene oxide)-b-polystyrene,” *Journal of the American Chemical Society*, vol. 129, no. 6, pp. 1690–1697, 2007.
- [49] F. Zhang, Y. Meng, D. Gu, Z. Chen, B. Tu, and D. Zhao, “An Aqueous Cooperative Assembly Route To Synthesize Ordered Mesoporous

- Carbons with Controlled Structures and Morphology,” *Chemistry of Materials*, vol. 18, no. 22, pp. 5279–5288, 2006.
- [50] J. Jin, T. Mitome, Y. Egashira, and N. Nishiyama, “Phase control of ordered mesoporous carbon synthesized by a soft-templating method,” *Colloids and Surfaces A: Physicochemical and Engineering Aspects*, vol. 384, no. 1-3, pp. 58–61, 2011.
- [51] S. Tanaka, A. Doi, N. Nakatani, Y. Katayama, and Y. Miyake, “Synthesis of ordered mesoporous carbon films, powders, and fibers by direct triblock-copolymer-templating method using an ethanol/water system,” *Carbon*, vol. 47, no. 11, pp. 2688–2698, 2009.
- [52] U. B. Suryavanshi, T. Ijima, A. Hayashi, Y. Hayashi, and M. Tanemura, “Simple methods for tuning the pore diameter of mesoporous carbon,” *Chemical communications*, vol. 47, no. 38, pp. 10758–60, 2011.
- [53] Y. Huang, H. Cai, T. Yu, F. Zhang, F. Zhang, Y. Meng, D. Gu, Y. Wan, X. Sun, B. Tu, and D. Zhao, “Formation of mesoporous carbon with a face-centered-cubic Fd3m structure and bimodal architectural pores from the reverse amphiphilic triblock copolymer PPO-PEO-PPO.,” *Angewandte Chemie (International ed. in English)*, vol. 46, no. 7, pp. 1089–93, 2007.
- [54] C. Xue, B. Tu, and D. Zhao, “Facile fabrication of hierarchically porous carbonaceous monoliths with ordered mesostructure via an organic organic self-assembly,” *Nano Research*, vol. 2, no. 3, pp. 242–253, 2009.
- [55] I. Muylaert, A. Verberckmoes, J. De Decker, and P. Van Der Voort, “Ordered mesoporous phenolic resins: highly versatile and ultra stable support materials,” *Advances in colloid and interface science*, vol. 175, pp. 39–51, 2012.
- [56] K. Hou, A. Zhang, L. Gu, M. Liu, and X. Guo, “Efficient synthesis and sulfonation of ordered mesoporous carbon materials.,” *Journal of colloid and interface science*, vol. 377, no. 1, pp. 18–26, 2012.
- [57] C. Liu, L. Li, H. Song, and X. Chen, “Facile synthesis of ordered mesoporous carbons from F108/resorcinol-formaldehyde composites obtained in basic media.,” *Chemical communications*, no. 7, pp. 757–759, 2007.
- [58] G. P. Hao, W. C. Li, S. Wang, G. H. Wang, L. Qi, and A. H. Lu, “Lysine-assisted rapid synthesis of crack-free hierarchical carbon monoliths with a hexagonal array of mesopores,” *Carbon*, vol. 49, no. 12, pp. 3762–3772, 2011.

- [59] A.-h. Lu, B. Spliethoff, and F. Schu, "Aqueous Synthesis of Ordered Mesoporous Carbon via Self-Assembly Catalyzed by Amino Acid," *Chem. Mater.*, vol. 20, no. 6, pp. 5314–5319, 2008.
- [60] A. Nieto, M. Vila, and A. Garcá, "Easy synthesis of ordered mesoporous carbon containing nickel nanoparticles by a low temperature hydrothermal method," vol. 1, 2012.
- [61] F. Zhang, Y. Meng, D. Gu, Y. Yan, C. Yu, B. Tu, and D. Zhao, "A Facile Aqueous Route to Synthesize Highly Ordered Mesoporous Polymers and Bicontinuous Cubic Structure and Carbon Frameworks with Ia3," *J. Am. Chem. Soc.*, pp. 13508–13509, 2005.
- [62] P. Gao, A. Wang, X. Wang, and T. Zhang, "Synthesis of highly ordered ir-containing mesoporous carbon materials by organic-organic self-assembly," *Chemistry of Materials*, vol. 20, no. 5, pp. 1881–1888, 2008.
- [63] T.-Y. Ma, L. Liu, and Z.-Y. Yuan, "Direct synthesis of ordered mesoporous carbons," *Chemical Society reviews*, vol. 42, no. 9, pp. 3977–4003, 2013.
- [64] Y. Wan, Y. Shi, and D. Zhao, "Designed synthesis of mesoporous solids via nonionic-surfactant-templating approach.," *Chemical communications*, no. 9, pp. 897–926, 2007.
- [65] J. Xu, A. Wang, and T. Zhang, "A two-step synthesis of ordered mesoporous resorcinol-formaldehyde polymer and carbon," *Carbon*, vol. 50, no. 5, pp. 1807–1816, 2012.
- [66] R. Liu, Y. Shi, Y. Wan, Y. Meng, F. Zhang, D. Gu, Z. Chen, B. Tu, and D. Zhao, "Triconstituent co-assembly to ordered mesostructured polymer-silica and carbon-silica nanocomposites and large-pore mesoporous carbons with high surface areas.," *Journal of the American Chemical Society*, vol. 128, no. 35, pp. 11652–11662, 2006.
- [67] S. Tanaka, N. Nakatani, A. Doi, and Y. Miyake, "Preparation of ordered mesoporous carbon membranes by a soft-templating method," *Carbon*, vol. 49, no. 10, pp. 3184–3189, 2011.
- [68] D. M. Nevskaja, E. Castillejos-Lopez, A. Guerrero-Ruiz, and V. Muñoz, "Effects of the surface chemistry of carbon materials on the adsorption of phenol-aniline mixtures from water," *Carbon*, vol. 42, no. 3, pp. 653–665, 2004.
- [69] R. Otero, D. Esquivel, M. A. Ulibarri, F. J. Romero-Salguero, P. Van Der Voort, and J. M. Fernández, "Mesoporous phenolic resin and mesoporous carbon for the removal of S-Metolachlor and Bentazon herbicides," *Chemical Engineering Journal*, vol. 251, pp. 92–101, 2014.

- [70] B. Hu, K. Wang, L. Wu, S. H. Yu, M. Antonietti, and M. M. Titirici, "Engineering carbon materials from the hydrothermal carbonization process of biomass," *Advanced Materials*, vol. 22, no. 7, pp. 813–828, 2010.
- [71] J. D. Decker, T. Bogaerts, I. Muylaert, S. Delahaye, F. Lynen, V. V. Speybroeck, A. Verberckmoes, and P. V. D. Voort, "Covalent immobilization of the Jacobsen catalyst on mesoporous phenolic polymer : A highly enantioselective and stable asymmetric epoxidation catalyst," *Materials Chemistry and Physics*, vol. 141, no. 2-3, pp. 967–972, 2013.
- [72] S. H. Joo, C. Pak, D. J. You, S.-A. Lee, H. I. Lee, J. M. Kim, H. Chang, and D. Seung, "Ordered mesoporous carbons (OMC) as supports of electrocatalysts for direct methanol fuel cells (DMFC): Effect of carbon precursors of OMC on DMFC performances," *Electrochimica Acta*, vol. 52, no. 4, pp. 1618–1626, 2006.
- [73] A. Léonard, A. Vantomme, C. Bouvy, N. Moniotte, P. Mariaulle, and B.-l. Su, "Highly Ordered Mesoporous and Hierarchically Nanostructured Meso- macroporous Materials for Nanotechnology , Biotechnology , Information Technology and Medical Applications," *Microporous and Mesoporous Materials*, vol. 1, pp. 1–44, 2006.
- [74] J. D. Schuster, "Morphology Control of Ordered Mesoporous Carbons for High Capacity Lithium Sulfur Batteries," 2011.
- [75] J. Tang, T. Wang, X. Sun, Y. Guo, H. Xue, H. Guo, M. Liu, X. Zhang, and J. He, "Effect of transition metal on catalytic graphitization of ordered mesoporous carbon and Pt/metal oxide synergistic electrocatalytic performance," *Microporous and Mesoporous Materials*, vol. 177, pp. 105–112, 2013.
- [76] J. Tang, J. Liu, N. L. Torad, T. Kimura, and Y. Yamauchi, "Tailored design of functional nanoporous carbon materials toward fuel cell applications," *Nano Today*, vol. 9, no. 3, pp. 305–323, 2014.
- [77] J. Wang, C. Xue, Y. Lv, F. Zhang, B. Tu, and D. Zhao, "Kilogram-scale synthesis of ordered mesoporous carbons and their electrochemical performance," *Carbon*, vol. 49, no. 13, pp. 4580–4588, 2011.
- [78] S. Zhang, F. Yao, L. Yang, F. Zhang, and S. Xu, "Sulfur-doped mesoporous carbon from surfactant-intercalated layered double hydroxide precursor as high-performance anode nanomaterials for both Li-ion and Na-ion batteries," *Carbon*, vol. 93, pp. 143–150, 2015.
- [79] Y. Dong, H. Lin, and F. Qu, "Synthesis of ferromagnetic ordered mesoporous carbons for bulky dye molecules adsorption," *Chemical Engineering Journal*, vol. 193-194, pp. 169–177, 2012.

- [80] Y. Tian, X. Wang, and Y. Pan, "Simple synthesis of Ni-containing ordered mesoporous carbons and their adsorption/desorption of methylene orange," *Journal of Hazardous Materials*, vol. 213-214, pp. 361–368, 2012.
- [81] C. L. Mangun, K. R. Benak, J. Economy, and K. L. Foster, "Surface chemistry, pore sizes and adsorption properties of activated carbon fibers and precursors treated with ammonia," *Carbon*, vol. 39, no. 12, pp. 1809–1820, 2001.
- [82] Z. Xiang, D. Cao, L. Huang, J. Shui, M. Wang, and L. Dai, "Nitrogen-doped holey graphitic carbon from 2D covalent organic polymers for oxygen reduction," *Advanced Materials*, vol. 26, pp. 3315–3320, 2014.
- [83] Q.-F. Deng, L. Liu, X.-Z. Lin, G. Du, Y. Liu, and Z.-Y. Yuan, "Synthesis and CO₂ capture properties of mesoporous carbon nitride materials," *Chemical Engineering Journal*, vol. 203, pp. 63–70, 2012.
- [84] G. P. Hao, W. C. Li, D. Qian, and A. H. Lu, "Rapid synthesis of nitrogen-doped porous carbon monolith for CO₂ capture," *Advanced Materials*, vol. 22, no. 7, pp. 853–857, 2010.
- [85] Y. Wan, Y. Shi, and D. Zhao, "Supramolecular aggregates as templates: Ordered mesoporous polymers and carbons," *Chemistry of Materials*, vol. 20, no. 3, pp. 932–945, 2008.
- [86] Z. Wu, P. a. Webley, and D. Zhao, "Comprehensive study of pore evolution, mesostructural stability, and simultaneous surface functionalization of ordered mesoporous carbon (FDU-15) by wet oxidation as a promising adsorbent.," *Langmuir : the ACS journal of surfaces and colloids*, vol. 26, no. 12, pp. 10277–86, 2010.
- [87] C. Moreno-Castilla, "Adsorption of organic molecules from aqueous solutions on carbon materials," *Carbon*, vol. 42, no. 1, pp. 83–94, 2004.
- [88] M. Hartmann, "Ordered Mesoporous Materials for Bioadsorption and Biocatalysis," *Chemistry of Materials*, vol. 17, no. 18, pp. 4577–4593, 2005.
- [89] D. J. de Ridder, *Adsorption of organic micropollutants onto activated carbon and zeolites, PhD thesis, Technical University of Delft*. 2012.
- [90] H. M. H. Gad and A. A. El-Sayed, "Activated carbon from agricultural by-products for the removal of Rhodamine-B from aqueous solution," *Journal of Hazardous Materials*, vol. 168, no. 2-3, pp. 1070–1081, 2009.

- [91] W. Lei, D. Portehault, D. Liu, S. Qin, and Y. Chen, "Porous boron nitride nanosheets for effective water cleaning," *Nature communications*, vol. 4, p. 1777, 2013.
- [92] M. Dai and B. D. Vogt, "High capacity magnetic mesoporous carbon-cobalt composite adsorbents for removal of methylene green from aqueous solutions," *Journal of colloid and interface science*, vol. 387, no. 1, pp. 127–34, 2012.
- [93] F. Liu, J. Wang, L. Li, Y. Shao, Z. Xu, and S. Zheng, "Adsorption of direct yellow 12 onto ordered mesoporous carbon and activated carbon," *Journal of Chemical and Engineering Data*, vol. 54, no. 11, pp. 3043–3050, 2009.
- [94] a. Vinu, K. Hossain, G. Satish Kumar, and K. Ariga, "Adsorption of l-histidine over mesoporous carbon molecular sieves," *Carbon*, vol. 44, no. 3, pp. 530–536, 2006.
- [95] X. Yuan, W. Xing, S. P. Zhuo, W. Si, X. Gao, Z. Han, and Z. F. Yan, "Adsorption of bulky molecules of nonylphenol ethoxylate on ordered mesoporous carbons," *Journal of Colloid and Interface Science*, vol. 322, no. 2, pp. 558–565, 2008.
- [96] M.-y. Chen, M. Ike, and M. Fujita, "Acute Toxicity , Mutagenicity , and Estrogenicity of Bisphenol-A and Other Bisphenols," *Journal of Environmental Toxicology*, vol. 17, no. 1, pp. 80–86, 2001.
- [97] D. Nakamura, Y. Yanagiba, Z. Duan, Y. Ito, A. Okamura, N. Asaeda, Y. Tagawa, C. Li, K. Taya, S.-Y. Zhang, H. Naito, D. H. Ramdhan, M. Kamijima, and T. Nakajima, "Bisphenol A may cause testosterone reduction by adversely affecting both testis and pituitary systems similar to estradiol," *Toxicology letters*, vol. 194, no. 1-2, pp. 16–25, 2010.
- [98] W.-T. Tsai, C.-W. Lai, and T.-Y. Su, "Adsorption of bisphenol-A from aqueous solution onto minerals and carbon adsorbents.," *Journal of hazardous materials*, vol. 134, no. 1-3, pp. 169–75, 2006.
- [99] Q. Tao, Z. Xu, J. Wang, F. Liu, H. Wan, and S. Zheng, "Adsorption of humic acid to aminopropyl functionalized SBA-15," *Microporous and Mesoporous Materials*, vol. 131, no. 1-3, pp. 177–185, 2010.
- [100] Q. Sui, J. Huang, Y. Liu, X. Chang, G. Ji, S. Deng, T. Xie, and G. Yu, "Rapid removal of bisphenol A on highly ordered mesoporous carbon," *Journal of Environmental Sciences*, vol. 23, no. 2, pp. 177–182, 2011.
- [101] A. A. Attia, B. S. Girgis, and S. A. Khedr, "Capacity of activated carbon derived from pistachio shells by H₃PO₄ in the removal of dyes and

- phenolics,” *Journal of Chemical Technology and Biotechnology*, vol. 78, no. 6, pp. 611–619, 2003.
- [102] M. Teng, J. Qiao, F. Li, and P. K. Bera, “Electrospun mesoporous carbon nanofibers produced from phenolic resin and their use in the adsorption of large dye molecules,” *Carbon*, vol. 50, no. 8, pp. 2877–2886, 2012.
- [103] X. Zhuang, Y. Wan, C. Feng, Y. Shen, and D. Zhao, “Highly Efficient Adsorption of Bulky Dye Molecules in Wastewater on Ordered Mesoporous Carbons,” *Chem. Mater.*, no. 12, pp. 706–716, 2009.
- [104] P. K. Tripathi, M. Liu, L. Gan, J. Qian, Z. Xu, D. Zhu, and N. N. Rao, “High surface area ordered mesoporous carbon for high-level removal of rhodamine B,” *Journal of Materials Science*, vol. 48, no. 22, pp. 8003–8013, 2013.
- [105] A. Vinu, M. Miyahara, V. Sivamurugan, T. Mori, and K. Ariga, “Large pore cage type mesoporous carbon, carbon nanocage: a superior adsorbent for biomaterials,” *Journal of Materials Chemistry*, vol. 15, no. 48, p. 5122, 2005.
- [106] a. Vinu and M. Hartmann, “Characterization and microporosity analysis of mesoporous carbon molecular sieves by nitrogen and organics adsorption,” *Catalysis Today*, vol. 102-103, pp. 189–196, 2005.
- [107] A. Li, X. Zhao, H. Liu, and J. Qu, “Characteristic transformation of humic acid during photoelectrocatalysis process and its subsequent disinfection byproduct formation potential,” *Water Research*, vol. 45, no. 18, pp. 6131–6140, 2011.
- [108] A. Rodrigues, A. Brito, P. Janknecht, M. F. Proença, and R. Nogueira, “Quantification of humic acids in surface water: effects of divalent cations, pH, and filtration,” *Journal of environmental monitoring : JEM*, vol. 11, no. 2, pp. 377–382, 2009.
- [109] A. Kołodziej, M. Fuentes, R. Baigorri, E. Lorenc-Grabowska, J. M. García-Mina, P. Burg, and G. Gryglewicz, “Mechanism of adsorption of different humic acid fractions on mesoporous activated carbons with basic surface characteristics,” *Adsorption*, vol. 20, no. 5-6, pp. 667–675, 2014.
- [110] T. S. Arnarson and R. G. Keil, “Mechanisms of pore water organic matter adsorption to montmorillonite,” *Marine Chemistry*, vol. 71, no. 3-4, pp. 309–320, 2000.

- [111] A. M. Shaker, Z. R. Komy, S. E. M. Heggy, and M. E. a. El-sayed, “Kinetic Study for Adsorption Humic Acid on Soil Minerals,” *Physical chemistry A*, vol. 116, pp. 10889–10896, 2012.
- [112] J. Stárek, A. Zukal, and J. Rathouský, “Comparison of the adsorption of humic acids from aqueous solutions on active carbon and activated charcoal cloths,” *Carbon*, vol. 32, no. 2, pp. 207–211, 1994.
- [113] I. Muylaert, *The development of mesoporous phenolic resins as support for heterogeneous catalysis*. PhD thesis, UGent, 2012.
- [114] M. Thommes, K. Kaneko, A. V. Neimark, J. P. Olivier, F. Rodriguez-reinoso, J. Rouquerol, and K. S. W. Sing, “Physisorption of gases , with special reference to the evaluation of surface area and pore size distribution (IUPAC Technical Report),” 2015.
- [115] S. A. Huber, A. Balz, M. Abert, and W. Pronk, “Characterisation of aquatic humic and non-humic matter with size-exclusion chromatography - organic carbon detection - organic nitrogen detection (LC-OCD-OND),” *Water Research*, vol. 45, no. 2, pp. 879–885, 2011.
- [116] L. Liu, Q.-F. Deng, Y.-P. Liu, T.-Z. Ren, and Z.-Y. Yuan, “HNO₃-activated mesoporous carbon catalyst for direct dehydrogenation of propane to propylene,” *Catalysis Communications*, vol. 16, no. 1, pp. 81–85, 2011.
- [117] L. Liu, Q.-F. Deng, T.-Y. Ma, X.-Z. Lin, X.-X. Hou, Y.-P. Liu, and Z.-Y. Yuan, “Ordered mesoporous carbons: citric acid-catalyzed synthesis, nitrogen doping and CO₂ capture,” *Journal of Materials Chemistry*, vol. 21, no. 40, p. 16001, 2011.
- [118] M. Wu, P. Ai, M. Tan, B. Jiang, Y. Li, J. Zheng, W. Wu, Z. Li, Q. Zhang, and X. He, “Synthesis of starch-derived mesoporous carbon for electric double layer capacitor,” *Chemical Engineering Journal*, vol. 245, pp. 166–172, 2014.
- [119] K. Y. Foo and B. H. Hameed, “Insights into the modeling of adsorption isotherm systems,” vol. 156, pp. 2–10, 2010.
- [120] P. Van Der Voort, C. Vercaemst, D. Schaubroeck, and F. Verpoort, “Ordered mesoporous materials at the beginning of the third millennium: new strategies to create hybrid and non-siliceous variants.,” *Physical chemistry chemical physics : PCCP*, vol. 10, no. 3, pp. 347–360, 2008.
- [121] I. Muylaert, J. Musschoot, K. Leus, J. Dendooven, C. Detavernier, and P. Van Der Voort, “Atomic Layer Deposition of Titanium and Vanadium

- Oxide on Mesoporous Silica and Phenol/Formaldehyde Resins - the Effect of the Support on the Liquid Phase Epoxidation of Cyclohexene," *European Journal of Inorganic Chemistry*, vol. 2012, no. 2, pp. 251–260, 2012.
- [122] J. Schuster, R. Köhn, M. Döblinger, A. Keilbach, H. Amenitsch, and T. Bein, "In situ SAXS study on a new mechanism for mesostructure formation of ordered mesoporous carbons: thermally induced self-assembly," *Journal of the American Chemical Society*, vol. 134, no. 27, pp. 11136–11145, 2012.
- [123] L. Chuenchom, R. Kraehnert, and B. M. Smarsly, "Recent progress in soft-templating of porous carbon materials," *Soft Matter*, vol. 8, no. 42, pp. 10801–10812, 2012.
- [124] B. Jones and C. J. Nachtsheim, "A Class of Three-Level Designs for Definitive Screening in the Presence of Second-Order Effects," *Journal of Quality Technology*, vol. 43, no. 1, pp. 1–15, 2011.
- [125] C. He and X. Hu, "Functionalized ordered mesoporous carbon for the adsorption of reactive dyes," *Adsorption*, vol. 18, no. 5-6, pp. 337–348, 2012.
- [126] X. Yuan, S.-P. Zhuo, W. Xing, H.-Y. Cui, X.-D. Dai, X.-M. Liu, and Z.-F. Yan, "Aqueous dye adsorption on ordered mesoporous carbons," *Journal of colloid and interface science*, vol. 310, no. 1, pp. 83–89, 2007.
- [127] J. Galán, a. Rodríguez, J. Gómez, S. Allen, and G. Walker, "Reactive dye adsorption onto a novel mesoporous carbon," *Chemical Engineering Journal*, vol. 219, pp. 62–68, 2013.
- [128] X. Wu, K. Hui, K. Hui, S. Lee, W. Zhou, R. Chen, D. Hwang, Y. Cho, and Y. Son, "Adsorption of basic yellow 87 from aqueous solution onto two different mesoporous adsorbents," *Chemical Engineering Journal*, vol. 180, pp. 91–98, 2012.
- [129] Y. Tian, P. Liu, X. Wang, and H. Lin, "Adsorption of malachite green from aqueous solutions onto ordered mesoporous carbons," *Chemical Engineering Journal*, vol. 171, no. 3, pp. 1263–1269, 2011.
- [130] A. Belfroid, M. van Velzen, B. van der Horst, and D. Vethaak, "Occurrence of bisphenol A in surface water and uptake in fish: evaluation of field measurements," *Chemosphere*, vol. 49, no. 1, pp. 97–103, 2002.
- [131] C. a. Staples, P. B. Dorn, G. M. Klecka, S. T. O'Block, D. R. Branson, and L. R. Harris, "Bisphenol A concentrations in receiving waters near US manufacturing and processing facilities," *Chemosphere*, vol. 40, no. 5, pp. 521–5, 2000.

- [132] K. Agenson, "Retention of a wide variety of organic pollutants by different nanofiltration/reverse osmosis membranes: controlling parameters of process," *Journal of Membrane Science*, vol. 225, no. 1-2, pp. 91–103, 2003.
- [133] A. Nakanishi, M. Tamai, N. Kawasaki, T. Nakamura, and S. Tanada, "Adsorption characteristics of bisphenol A onto carbonaceous materials produced from wood chips as organic waste," *Journal of colloid and interface science*, vol. 252, no. 2, pp. 393–6, 2002.
- [134] J. Xu, L. Wang, and Y. Zhu, "Decontamination of bisphenol A from aqueous solution by graphene adsorption.," *Langmuir : the ACS journal of surfaces and colloids*, vol. 28, no. 22, pp. 8418–8425, 2012.
- [135] L. D. Nghiem, D. Vogel, and S. Khan, "Characterising humic acid fouling of nanofiltration membranes using bisphenol A as a molecular indicator," *Water research*, vol. 42, no. 15, pp. 4049–58, 2008.
- [136] S. Schlienger, C. Ducrot-boisgontier, J. Patarin, L. Michelin, and C. Vix-guterl, "Study Of The Formation Mechanisms Of Self-assembly Mesostructured Polymer Precursor For Ordered Mesoporous Carbons," *Carbon*, 2010.
- [137] J. Górka, A. Zawislak, J. Choma, and M. Jaroniec, "Adsorption and structural properties of soft-templated mesoporous carbons obtained by carbonization at different temperatures and KOH activation," *Applied Surface Science*, vol. 256, no. 17, pp. 5187–5190, 2010.
- [138] D. J. Kim, H. I. Lee, J. E. Yie, S.-J. Kim, and J. M. Kim, "Ordered mesoporous carbons: Implication of surface chemistry, pore structure and adsorption of methyl mercaptan," *Carbon*, vol. 43, no. 9, pp. 1868–1873, 2005.
- [139] J. Jin, N. Nishiyama, Y. Egashira, and K. Ueyama, "Pore structure and pore size controls of ordered mesoporous carbons prepared from resorcinol/formaldehyde/triblock polymers," *Microporous and Mesoporous Materials*, vol. 118, no. 1-3, pp. 218–223, 2009.
- [140] P. Van Der Voort, M. Benjelloun, and E. F. Vansant, "Rationalization of the synthesis of SBA-16: Controlling the micro- and mesoporosity," *Journal of Physical Chemistry B*, vol. 106, no. 35, pp. 9027–9032, 2002.
- [141] M. H. Kutner, C. J. Nachtsheim, J. Neter, and W. Li, *Applied Linear Statistical Models Fifth Edition*.
- [142] P. Liu, J. Jiao, and Y. Huang, "Ordered mesoporous carbon prepared from triblock copolymer/novolac composites," *Journal of Porous Materials*, vol. 20, no. 1, pp. 107–113, 2012.

- [143] C.-Y. Kuo, "Comparison with as-grown and microwave modified carbon nanotubes to removal aqueous bisphenol A," *Desalination*, vol. 249, no. 3, pp. 976–982, 2009.
- [144] G. Liu, J. Ma, X. Li, and Q. Qin, "Adsorption of bisphenol A from aqueous solution onto activated carbons with different modification treatments.," *Journal of hazardous materials*, vol. 164, no. 2-3, pp. 1275–1280, 2009.
- [145] Y.-H. Kim, B. Lee, K.-H. Choo, and S.-J. Choi, "Selective adsorption of bisphenol A by organic–inorganic hybrid mesoporous silicas," *Microporous and Mesoporous Materials*, vol. 138, no. 1-3, pp. 184–190, 2011.
- [146] M. Kruk, M. Jaroniec, R. Ryoo, and S. H. Joo, "Characterization of Ordered Mesoporous Carbons Synthesized Using MCM-48 Silicas as Templates," *J. Phys. Chem. B*, vol. 104, pp. 7960–7968, 2000.
- [147] S. Jun, Sang Hoon Joo, R. Ryoo, M. Kruk, M. Jaroniec, Z. Liu, T. Ohsuna, and O. Terasaki, "Synthesis of new, nanoporous carbon with hexagonally ordered mesostructure," *Journal of the American Chemical Society*, vol. 122, no. 11, pp. 10712–10713, 2000.
- [148] T.-W. Kim, I.-S. Park, and R. Ryoo, "A synthetic route to ordered mesoporous carbon materials with graphitic pore walls," *Angewandte Chemie (International ed. in English)*, vol. 42, no. 36, pp. 4375–4379, 2003.
- [149] K. P. Gierszal, M. Jaroniec, T.-W. Kim, J. Kim, and R. Ryoo, "High temperature treatment of ordered mesoporous carbons prepared by using various carbon precursors and ordered mesoporous silica templates," *New Journal of Chemistry*, vol. 32, p. 981, 2008.
- [150] I. T. Cousins, C. A. Staples, G. M. Kle^ˆ, and D. Mackay, "A Multimedia Assessment of the Environmental Fate of Bisphenol A," *Human and Ecological Risk Assessment*, vol. 8, no. 5, pp. 1107–1135, 2002.
- [151] R. Leyva-ramos, "Role of pore volume and surface diffusion in the adsorption of aromatic compounds on activated carbon," *Adsorption*, no. 6, pp. 945–957, 2013.
- [152] W. Libbrecht, F. Deruyck, H. Poelman, A. Verberckmoes, J. Thybaut, J. De Clercq, and P. Van Der Voort, "Optimization of soft templated mesoporous carbon synthesis using Definitive Screening Design," *Chemical Engineering Journal*, vol. 259, pp. 126–134, 2015.
- [153] H. Soni and P. Padmaja, "Palm shell based activated carbon for removal of bisphenol A: an equilibrium, kinetic and thermodynamic study," *Journal of Porous Materials*, vol. 21, no. 3, 2014.

- [154] N. Wickramaratne and M. Jaroniec, "Adsorption and structural properties of ordered mesoporous carbons synthesized by soft-templating in the presence of boric acid and tetraethyl orthosilicate," *RSC Advances*, vol. 2, no. 5, p. 1877, 2012.
- [155] H. Tamai, T. Kakii, Y. Hirota, T. Kumamoto, and H. Yasuda, "Synthesis of extremely large mesoporous activated carbon and its unique adsorption for giant molecules," *Chemistry of Materials*, vol. 8, no. 2, pp. 454–462, 1996.
- [156] J. Liu, J. Cao, H. Chen, and D. Zhou, "Adsorptive removal of humic acid from aqueous solution by micro- and mesoporous covalent triazine-based framework," *Colloids and Surfaces A: Physicochemical and Engineering Aspects*, vol. 481, pp. 276–282, 2015.
- [157] J. Yu, M. Guo, F. Muhammad, A. Wang, F. Zhang, Q. Li, and G. Zhu, "One-pot synthesis of highly ordered nitrogen-containing mesoporous carbon with resorcinol-urea-formaldehyde resin for CO₂ capture," *Carbon*, vol. 69, pp. 502–514, 2014.
- [158] K.-y. Shi, X.-x. Tao, F.-f. Hong, H. He, Y.-h. Ji, and J.-l. Li, "Mechanism of oxidation of low rank coal by nitric acid," *Journal of Coal Science and Engineering (China)*, vol. 18, no. 4, pp. 396–399, 2012.
- [159] E. Lorenc-Grabowska and G. Gryglewicz, "Adsorption of lignite-derived humic acids on coal-based mesoporous activated carbons," *Journal of Colloid and Interface Science*, vol. 284, no. 2, pp. 416–423, 2005.
- [160] Y. Ho, J. C. Y. Ng, and G. McKay, "Kinetics of pollutant sorption by biosorbents: review," *Separation & Purification Methods*, vol. 29, no. 2, pp. 189–232, 2000.
- [161] C. Jucker and M. M. Clark, "Adsorption of Aquatic Humic Substances on Hydrophobic Ultrafiltration Membranes," *Journal of Membrane Science*, vol. 97, no. 94, pp. 37–52, 1994.
- [162] N. E. Palmer and R. Von Wandruszka, "Dynamic light scattering measurements of particle size development in aqueous humic materials," *Analytical and Bioanalytical Chemistry*, vol. 371, no. 7, pp. 951–954, 2001.
- [163] B. Ertuğ, "Powder Preparation , Properties and Industrial Applications of Hexagonal Boron Nitride," *Sintering Applications*, 1950.
- [164] L. Márcia, S. Ansaloni, E. Martins, and B. D. Sousa *Materials Sciences and Applications*.

- [165] A. Auroux, P. Miele, and B. Bonnetot, "Porous boron nitride supports obtained from molecular precursors . Influence of the precursor formulation and of the thermal treatment on the properties of the BN ceramic," vol. 657, pp. 98–106, 2002.
- [166] S. Bernard, P. Miele, J. B. Parra, and M. Cedex, "Micro-, Mesoporous Boron Nitride-Based Materials Templated from Zeolites," *Chem. Mater.*, vol. 24, 2012.
- [167] W.-Q. Han, R. Brutchey, T. D. Tilley, and A. Zettl, "Activated Boron Nitride Derived from Activated Carbon," *Nano Letters*, vol. 4, no. 1, pp. 173–176, 2004.
- [168] J. Li, J. Lin, X. Xu, X. Zhang, and Y. Xue, "Porous boron nitride with a high surface area : hydrogen storage and water treatment," *Nanotechnology*, vol. 24, pp. 155603–155610, 2013.
- [169] J. Li, X. Xiao, X. Xu, J. Lin, Y. Huang, Y. Xue, P. Jin, J. Zou, and C. Tang, "Activated boron nitride as an effective adsorbent for metal ions and organic pollutants," *Scientific reports*, vol. 3, pp. 3208–3214, 2013.
- [170] M. b. Maleki, A. Beitollahi, J. Lee, M. Shokouhimehr, J. Javadpour, E. Park, J. Chun, and J. Hwang, "One pot synthesis of mesoporous boron nitride using polystyrene-b-poly(ethylene oxide) block copolymer," *RSC Advances*, vol. 5, no. 9, pp. 6528–6535, 2015.
- [171] B. Rushton and R. Mokaya, "Mesoporous boron nitride and boron-nitride-carbon materials from mesoporous silica templates," *Journal of Materials Chemistry*, vol. 18, no. 2, pp. 235–241, 2008.
- [172] P. Dibandjo, F. Chassagneux, L. Bois, C. Sigala, and P. Miele, "Comparison between SBA-15 silica and CMK-3 carbon nanocasting for mesoporous boron nitride synthesis," *Journal of Materials Chemistry*, vol. 15, no. 19, pp. 1917–1923, 2005.
- [173] D. Liu, W. Lei, S. Qin, and Y. Chen, "Template-free synthesis of functional 3D BN architecture for removal of dyes from water," *Scientific reports*, vol. 4, pp. 4453–4457, 2014.
- [174] L. Xue, B. Lu, Z.-S. Wu, C. Ge, P. Wang, R. Zhang, and X.-D. Zhang, "Synthesis of mesoporous hexagonal boron nitride fibers with high surface area for efficient removal of organic pollutants," *Chemical Engineering Journal*, vol. 243, pp. 494–499, 2014.
- [175] M. Maleki, A. Beitollahi, and M. Shokouhimehr, "Template-free synthesis of porous boron nitride using a single source precursor," *RSC Advances*, vol. 5, no. 58, pp. 46823–46828, 2015.

- [176] Y. Li, B. Yuan, J. Fu, S. Deng, and X. Lu, "Adsorption of alkaloids on ordered mesoporous carbon," *Journal of Colloid and Interface Science*, vol. 408, no. 1, pp. 181–190, 2013.
- [177] N. Zhang, H. Liu, H. Kan, X. Wang, H. Long, and Y. Zhou, "The preparation of high-adsorption, spherical, hexagonal boron nitride by template method," *Journal of Alloys and Compounds*, vol. 613, pp. 74–79, 2014.
- [178] S. Frueh, R. Kellett, C. Mallery, T. Molter, W. S. Willis, C. King'onde, and S. L. Suib, "Pyrolytic decomposition of ammonia borane to boron nitride," *Inorganic chemistry*, vol. 50, no. 3, pp. 783–92, 2011.
- [179] L. Lin, Z. Li, Y. Zheng, and K. Wei, "Synthesis and Application in the CO Oxidation Conversion Reaction of Hexagonal Boron Nitride with High Surface Area," *Journal of the American Ceramic Society*, vol. 92, no. 6, pp. 1347–1349, 2009.
- [180] P. Singla, N. Goel, V. Kumar, and S. Singhal, "Boron nitride nanomaterials with different morphologies: Synthesis, characterization and efficient application in dye adsorption," *Ceramics International*, vol. 41, no. 9, pp. 10565–10577, 2015.
- [181] H.-L. Zhu, Q.-X. Han, J. Wu, X.-L. Meng, and H.-Z. Cui, "Large scale synthesis of nanoporous BN flake with high surface areas," *Journal of Crystal Growth*, vol. 434, pp. 19–24, 2015.
- [182] A. Roy, A. Choudhury, and C. Rao, "Supramolecular hydrogen-bonded structure of a 1:2 adduct of melamine with boric acid," *Journal of Molecular Structure*, vol. 613, no. 1-3, pp. 61–66, 2002.
- [183] C. Hoffendahl, S. Duquesne, G. Fontaine, and S. Bourbigot, "Decomposition mechanism of melamine borate in pyrolytic and thermo-oxidative conditions," *Thermochimica Acta*, vol. 590, pp. 73–83, 2014.
- [184] L. Li, X. Yao, C. Sun, A. Du, L. Cheng, Z. Zhu, C. Yu, J. Zou, S. C. Smith, P. Wang, H. M. Cheng, R. L. Frost, and G. Q. Lu, "Lithium-catalyzed dehydrogenation of ammonia borane within mesoporous carbon framework for chemical hydrogen storage," *Advanced Functional Materials*, vol. 19, pp. 265–271, 2009.
- [185] C. Schimpf, H. Schumann, J. Rathel, M. Herrmann, and D. Rafaja, "High-temperature stability of microstructure defects in graphitic boron nitride subjected to the field assisted sintering," *Journal of the European Ceramic Society*, vol. 36, no. 1, pp. 43–49, 2016.

- [186] B. Matović, J. Luković, M. Nikolić, B. Babić, N. Stanković, B. Jokić, and B. Jelenković, “Synthesis and characterization of nanocrystalline hexagonal boron nitride powders: XRD and luminescence properties,” *Ceramics International*, vol. 42, no. 15, pp. 16655–16658, 2016.
- [187] J. Li, X. Xiao, X. Xu, J. Lin, Y. Huang, Y. Xue, P. Jin, J. Zou, and C. Tang, “Activated boron nitride as an effective adsorbent for metal ions and organic pollutants,” *Scientific reports*, vol. 3, pp. 3208–3214, 2013.
- [188] Y. Chen, J. Zou, S. J. Campbell, and G. Le Caer, “Boron nitride nanotubes: Pronounced resistance to oxidation,” *Applied Physics Letters*, vol. 84, no. 13, pp. 2430–2432, 2004.
- [189] A. N. Streletskii, D. G. Permenov, B. B. Bokhonov, A. V. Leonov, and S. N. Mudretsova, “Mechanochemistry of hexagonal boron nitride. 2. Reactivity upon interaction with water,” *Colloid Journal*, vol. 72, no. 4, pp. 553–558, 2010.